UNIVERSITÉ DE BOURGOGNE
UFR Sciences et Techniques

LABORATOIRE INTERDISCIPLINAIRE CARNOT DE BOURGOGNE
UMR CNRS 5209

Interface Réactivité Matériaux
Métallurgie, Microstructure, Mécanique, Modélisation, Oxyde, Electrochimie

ÉCOLE DOCTORALE CARNOT

THÈSE DE DOCTORAT

Pour obtenir le grade de

DOCTEUR DE L'UNIVERSITÉ DE BOURGOGNE

Discipline **: Sciences**
Spécialité **: Chimie-Physique**

Low Cr Alloys With An Improved High Temperature Corrosion Resistance.

Harold Nicolas EVIN

Soutenu le 7 octobre 2010 à 14 heures 30 à l'amphithéâtre de l'ESIREM

JURY

Gilles BERTRAND	Professeur, Université de Bourgogne	**Examinateur**
Yves WOUTERS	Professeur, INP, Grenoble	**Rapporteur**
Daniel MONCEAU	Directeur de Recherche, CIRIMAT, Toulouse	**Rapporteur**
Alina AGÜERO	Docteur, INTA, Madrid	**Examinateur**
Philippe BOURGES	Ingénieur Industeel ArcelorMittal, Creusot	**Examinateur**
Cécilia FÖJER	Ingénieur OCAS N.V ArcelorMittal, Gand	**Co-directeur de thèse**
Sébastien CHEVALIER	Professeur, Université de Bourgogne	**Directeur de thèse**

A mère Carmen Régis-Constant,

A ma soeur Nicole Hejoaka,

A la famille Régis-Constant.

Sé Kouto Sèl Ki Sav Sa Ki en Tchè Jiromon

Avant-propos

Ce manuscrit conclue une période emplie de rencontres professionnelles, toutes plus intéressantes les unes que les autres, qui ont contribuées à la réussite du travail. C'est donc tout naturellement que cet avant propos est destiné à remercier l'ensemble d'entre elles.

Ce travail à été réalisé au sein du laboratoire Interdisciplinaire Carnot de Bourgogne (I.C.B), avec le soutien financier OCAS N.V ArcelorMittal Global R&D, Gand.

Je remercie le Pr. Gilles Bertrand, directeur de l'I.C.B., pour la confiance qu'il m'a accordée en m'offrant l'opportunité de faire une thèse au sein de cette structure et pour l'honneur qu'il m'a fait en présidant mon jury de thèse.

Je voudrais également exprimer ma profonde gratitude au Dr. Sven Vandeputte et au Dr. Serge Claessens, dirigeants OCAS.NV pour leur soutien sans faille à ces travaux et les différents échanges constructifs que nous avons pu avoir.

Je tiens à témoigner toute ma reconnaissance au Dr. Daniel Monceau, directeur de recherche CNRS au laboratoire CIRIMAT, et au Pr. Yves Wouters, directeur adjoint du laboratoire SIMaP, pour avoir jugé ce travail de thèse et également pour l'accueil qu'ils m'ont fait au sein de la communauté scientifique de la Corrosion Haute Température.

Je remercie vivement le Dr. Alina Agüero, del « Instituto Nacional de Técnica Aeroespacial » de Madrid, ainsi que le Dr. Phillipe Bourges, ancien ingénieur Industeel ArcelorMittal le Creusot, qui ont accepté d'être membre du jury de cette thèse.

J'adresse mes plus sincèrement remerciements au Pr. Sébastien Chevalier, pour avoir supervisé mon travail et pour m'avoir fait bénéficier de son expérience dans le domaine. L'ensemble des échanges furent passionnants et ont contribués à la réalisation de ce projet dans les meilleures conditions qui soient. Qu'il soit assuré de mon amitié.

Le co-encadrement de cette thèse, fut également une réussite. C'est pourquoi je remercie chaleureusement Madame Cécilia Föjer, ingénieur à OCAS N.V pour sa disponibilité et sa réactivité et son importante contribution à la bonne organisation de ces travaux.

Ma gratitude va au Dr. Olivier Heintz, pour le partage de sa riche expérience dans les techniques de caractérisations de surfaces, mais également a l'ensemble du personnel de l'ICB que j'ai pu côtoyer tout au long de ce travail : le Dr. Claudie Josse, le Dr. Ionna Popa, le Dr. Rémi Chassagnon, le Dr. Carmen Marcos de Lucas, Madame Nathalie Roudergues, Monsieur Emmanuel Couqueberg, Monsieur Claude Febvre, Monsieur Stéphane Maître, et Mlle Céline Dirand.

Mes remerciements vont également à Monsieur Jean-Michel Damasse, directeur du Centre de Recherche D'Isbergues (C.R.I) ArcelorMittal Stainless Europe, pour m'avoir offert la possibilité de rejoindre ses équipes et de valoriser ce travail de thèse au sein de son laboratoire.

Je tenais notamment à rendre un hommage particulier, au Pr. Alexis Steinbrunn, ancien directeur de l'ESIREM (Ecole Supérieur d'Ingénieurs de Recherche En Matériaux et Infotronique) Dijon, qui au travers de ses engagements et de sa dévotion envers ses étudiants à contribuer à l'orientation de mon parcours.

Enfin, je ne saurais oublier mes condisciples étudiants, au premier rang desquels les Siciliens, fidèles compagnons d'armes qui m'ont été d'un grand soutien facilitant mon intégration loin de mes terres d'origines, mais également Olivier Delrue, Cyril Gaudillère, Céline Choux, Cédric Morin, Romain Gateau, Sébastien Fontana, Maria Rosa Ardigo, Jonathan Skrzypski, Vanessa Bellat, Virginie Richoux, et Magalie Quinet , tous garants des excellents moments et de la bonne humeur au sein du laboratoire. Merci à tous pour votre amitié et votre soutien.

Table of contents

Introduction

General context of the work p1
Thermal power plant nowadays and tomorrow p2

I. State of the Art p5

I.1 Historical development of T/P91 p5
I.2 High temperature corrosion of general knowledge p7
I.2.1 Thermodynamics considerations and oxidation mechanisms p8
I.2.2 Kinetics considerations p12
I.3 Iron oxidation p14
I.4 Chromium oxidation p15
I.5 Iron-chromium alloys oxidation p15
I.5.1 Chromia forming alloys p15
I.5.2 Low chromium containing alloys p17
I.6 Effect of water vapour p18
I.7 Cyclic oxidation p23
I.8 Coatings against high temperature corrosion p24
I.8.1 Chromia forming coatings p24
I.8.2 Alumina forming coatings p24
I.8.3 Metal Organic Chemical Vapour Deposition coatings p26
I.9 Alloying Elements Effects p26
I.9.1 Reactive Elements p27
I.9.2 Sulphur-Phosphorus p28
I.9.3 Tungsten p28
I.9.4 Molybdenum p29
I.9.5 Manganese p29
I.9.6 Vanadium p30
I.9.7 Silicon p31
I.9.8 Aluminum p33

II. Experimental Techniques p41

II.1 Materials and samples preparation p41
II.2 High temperature oxidation tests p42
II.2.1 Isothermal tests in dry air p42

II.2.2 Isothermal tests in air enriched with 12% Vol. of water vapour p42
II.2.3 Oxidation tests in cyclic condition p43
II.2.4 Long term oxidation p44
II.3 Characterization of the oxide scale p44
II.3.1 Scanning Electron Microscopy (SEM) p44
II.3.2 X-Ray Diffraction (XRD) at low glancing angle p45
II.3.4 Photoelectrochemistry (PEC) p45
II.3.5 Ex-situ and In-situ X-ray Photoelectron Spectroscopy (XPS) p47
II.3.6 Transmission Electron Microscopy (TEM) p49
II.3.7 In-situ diffraction analyses at the European Synchrotron Radiation Facility p50
II.3.8 Secondary Ion Mass Spectroscopy (SIMS) p51
II.4 Diffusion process and oxidation mechanisms p52
II.5 Metal Organic Chemical Vapour Deposition (MOCVD) p53
II.6 Aluminide Pack cementation coating p54
II.7 Casting preparation using a levitation melter p54

III. Fire side corrosion of 9% Cr steel p57

III.1 Kinetic study p57
III.2 Oxide Scale morphologies p59
III.3 Scale characterization, composition and mechanism p61
III.3.1 PhotoElectroChemistry Spectroscopy results (PEC) p61
III.3.2 RAMAN Spectroscopy Results p65
III.3.3 In-situ and ex-situ XPS results p67
III.3.4 TEM results on thin cross section prepared by FIB p73
III.3.5 In-situ high resolution powder diffraction experiments using synchrotron facilities (ESRF Grenoble) p77
III .3.6 Isotopic labeling assessment tool of species diffusion for thermally grown oxide scale. p81

III.4 Discussion and general summary for high temperature corrosion in laboratory air p83

IV. Effect of water vapour and steam p87

IV.1 Kinetic study and scale characterization p87
IV.1.1 Effect of air enriched with 12%vol. of water vapour p87
IV.1.2 Effect of steam p89
IV.2 In-situ XPS analyses results and steam effect P90
IV.3 Investigation of corrosion products by TEM p96
IV.4 Discussion and general summary for oxidation at high temperature in steam and water vapour p98

V. Ways to improve 9%Cr steel high temperature corrosion resistance p102

V.1 Coatings and high temperature oxidation resistance p102

V.1.1 Pack cementation coatings p101

V.1.2 Reactive element oxide coating by Metal Organic Chemical Vapour Deposition (MOCVD) p105

V.1.3 Cyclic tests at 700°C in laboratory air p107

V.2 Effect of alloying elements addition p109

V.2.1 Fire side corrosion tests p111

V.2.1.1 Isothermal test at 750°C in laboratory air p111

V.2.1.2 TEM results for casting enriched in silicon p115

V.2.1.3 Cyclic oxidation tests p118

V.2.2 Effect of water vapour and steam p119

V.2.2.1 Isothermal tests in water vapour environment and scale characterization p119

V.2.3 Steam effect on casting enriched in silicon, TEM results p124

V.3 General summary and discussion on ways to improve 9%Cr steel high temperature corrosion resistance p127

VI. Synthesis and outlooks p130

VI.1 Synsthesis p130

VI.2 Outlooks p132

Objectives

General Context of the work

The 21th century will be the century of energy and environmental revolution. One of main challenges that Mankind will have to face will be to answer energy needs of a demographical growing population. The Energy consumption in emerging countries, such as India, Brazil or China, has rapidly increased over the last ten years. This unexpected progression also coupled with an out growing demand in developed countries (North America and Europe) make international expert worried about an potential energy crisis. Relying on the energy outlook 2008 from International Energy Agency [1], global energetic demand could reach $20x10^{13}$ KWh per year by 2025 which could represent an average of 2% increase per year until 2020.

Nowadays, more than 90% of the product electricity comes from fossil fuel sources (coal, gas, oil etc…). Figure I.1 gives a projection of the energy production as a function of the different types of sources.

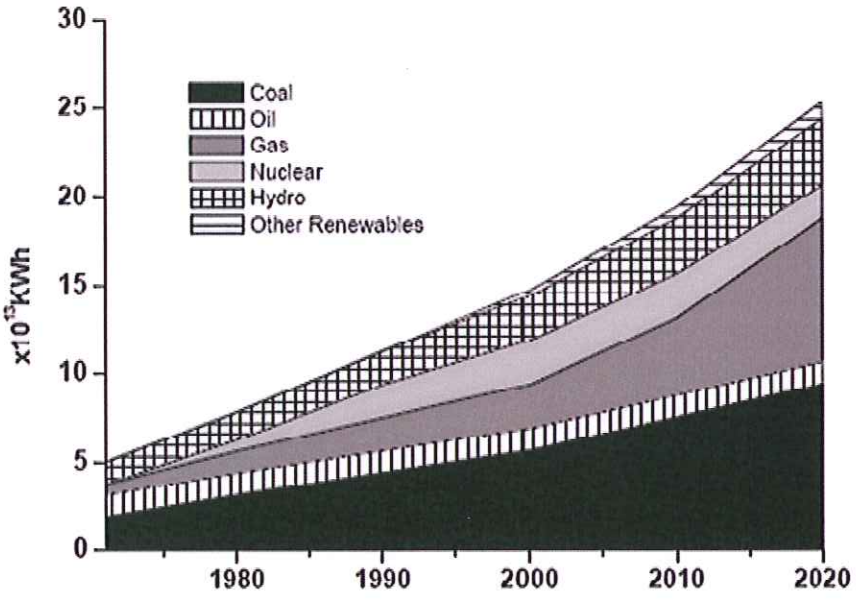

Figure 0.1: Trend in global energy production from 1971 to 2020 [2].

Even if important efforts are made to develop technologies using renewable or "clean" energy sources, they have not yet reached maturation. Therefore, to cover the new demands, fossil

fuel sources will still be exploited and a 60% per year of augmentation is expected for coal used between 2000 and 2020 [2].

Kyoto protocol ratified in 1998 by many countries, including the European Union, plans a significant reduction of green house effect gases emission. These include first of all CO_2 but also NOx. The Kyoto agreement plans a reduction of the overall green house effect gases emission by at least 5 % below the 1990 levels in the commitment period from 2008 to 2012 [3]. Thus, rarefactions of the sources, together with environmental constraints, are the engines for reflection on conversion efficiency of the current generation of power plants.

Thermal power plant nowadays and tomorrow.

In a thermal power plant the production of electricity in assured by the combustion of fossil fuel, either gas, oil, coal or a mixture of them all. The electric power is generated during a process which starts by heating water in a boiler and turning it into steam. This steam is brought at high temperature and pressure in a superheater and then flown into a turbine which drives a generator. After the turbine, the steam is condensed in a condenser and then the water is recycled in the heating part of the plant. The efficiency of the power plant is closely related to the steam parameters (pressure and temperature). Nowadays, steam is brought to above 22 MPa and above 540°C in a supercritical state. This corresponds to an electric efficiency function of the fuel used of approximately 33% to 48%.

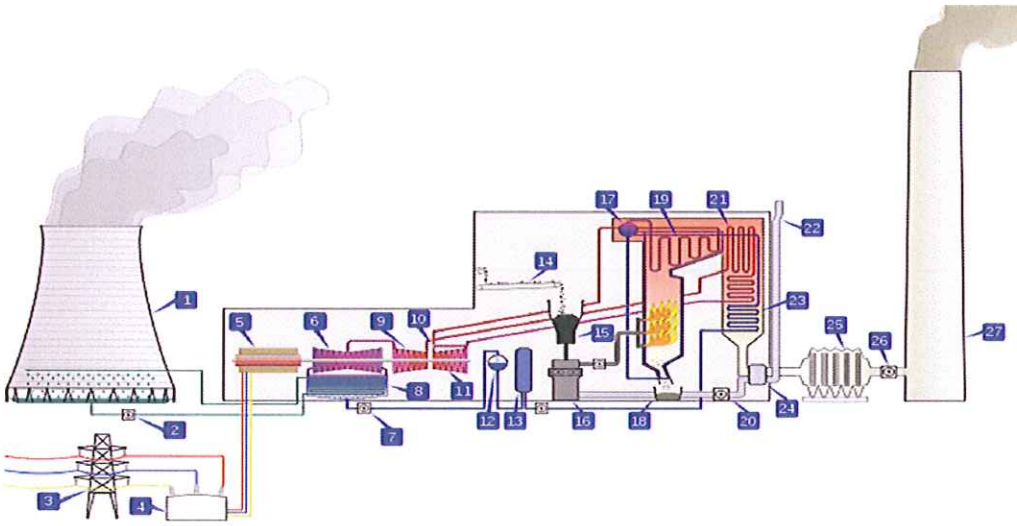

1. Cooling tower. 2. Cooling water pump. 3. Transmission line (3-phase). 4. Unit transformer (3-phase). 5. Electric generator (3-phase). 6. Low pressure turbine. 7. Condensate extraction pump. 8. Condensor. 9. Intermediate pressure turbine. 10. Steam governor valve. 11. High pressure turbine. 12. Deaerator. 13. Feed heater. 14. Coal conveyor. 15. Coal hopper. 16. Pulverised fuel mill. 17. Boiler drum. 18. Ash hopper. 19. Superheater. 20. Forced draught fan. 21. Reheater. 22. Air intake. 23. Economiser. 24. Air preheater. 25. Precipitator. 26. Induced draught fan. 27. Chimney Stack.

Figure 0.2 : schematic of a coal fired power plant [4].

To improve plant efficiency, it seems necessary to use higher temperature and pressure for the steam input and output parameters. As an example, the total efficiency of a plant increases by nearly 6 %when changing the steam parameters from 538 °C/18.5 MPa to 593 °C/30 MPa. It could even reach an 8 % increase at 650 °C [5].

For coal fired systems, temperatures up to 650 °C or even 700 °C with a pressure of 35 MPa are currently under consideration. The superheater tube part temperatures could often exceed the steam temperature by as much as 30 °C [5-7]. Improvement and development of new structure materials for those tubes are then compulsory steps to achieve such new working conditions. Materials with high temperature creep resistance are required. During the last decades, high temperature steels or more recently nickel-based alloys have demonstrated their potential with regards to high temperature creep strength. Nevertheless, metallic materials are well known for expanding when increasing the temperatures. The use of materials with low thermal expansion coefficients is necessary in order to minimize the generated mechanical stresses. To maximize also the energy conversion, thermal conductivity of the heater and superheater components should be kept high enough. Weldability of the materials involved has to be controlled and also optimized. Materials development becomes an important issue for the new generation of power plants which will

be designed to work at ultrasupercritical parameters of steam (600°C- 650°C, 30-35MPa) and green houses effect gas emissions such as CO_2. In this context, martensitic/ferritic 9% Cr steels, commercialized as T/P91, have been considered to be used for steam generators and heat exchangers for their good mechanical properties. But, the new targeted working conditions are much more aggressive than those where T/P91 is presently used in power plants (typically 530°C and 19 MPa). As a consequence, catastrophic oxidation behaviour is observed at temperatures higher than 600°C, and can result in the material damage.

The key to a successful improvement of T/P91 steel grade lies in a better understanding of the material reactivity under high temperature and high pressure through the observation and characterization of the germination and growth of the surface oxide layers occurring within the first oxidation instants in both hot dry air and hot wet atmosphere.

So, after a review of the states of the art concerning low chromium containing steel and a presentation of experimental equipments used for this work, a synthesis of the observations of the steel behaviour at high temperature in laboratory atmosphere will be realized in chapter III. This will lead to propose a sequence of the oxide scale formation in such environment. Then in chapter IV a particular attention will be paid to the effect of water vapor or steam on the steel oxidation rate at high temperature. In chapter V, ways to improve the high temperature oxidation resistance of 9% Cr steel grade will be proposed and tested. The results of those tests and their interpretation will help us to present conclusions and to consider outlooks for this work.

I. State of the Art

I.1 Historical development of T/P91

Development of 9%Cr steels has led to a number of new materials, which can be used in steam environment at around 580°C. These new steels have a stress rupture at this temperature close to that calculated for austenitic steels [8]. The main disadvantages of austenitic steels are their high coefficient of thermal expansion, their low thermal conductivity and their price. Those characteristics increase their thermal stresses when the temperature changes, corresponding to the working cyclic conditions of power plants, and therefore decrease their thermal fatigue resistance. For 9- 12%Cr steels, a fully martensitic microstructure with or without δ−ferrite is achieved after a simple austenitising and tempering treatment followed by air-cooling [9-10] (Figure I.1).

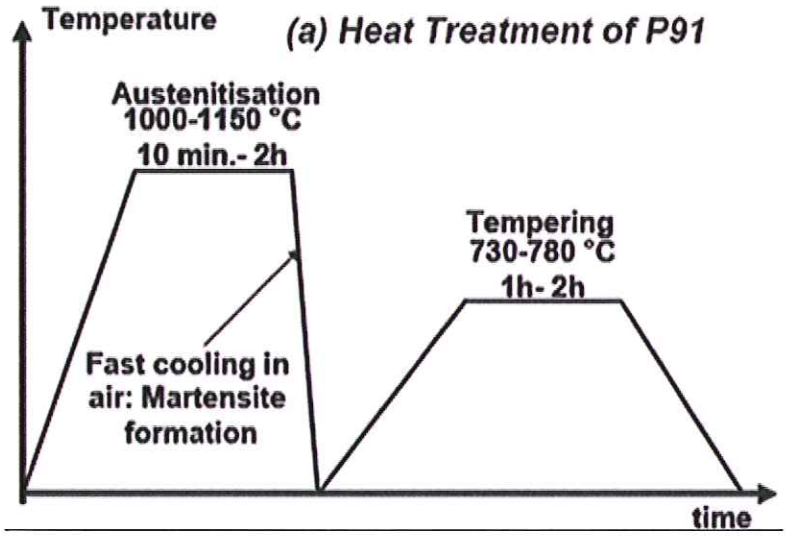

Figure I.1: P91 heat treatment [11].

Masuyama [8] presented an historical perspective on the development of steels for power plants. Ferritic steel developments are mostly aimed at their use for thick section pipes and heaters. Figure I.2 shows their evolution and their classification in over 4 generations. Among the commercialized 9%Cr steels, T/P91 has the highest stress resistance property and has been extensively used as material for heaters and steam pipes in power plants

operating at steam temperatures up to 590°C. Alloy NF 616 (T/P92), where part of the Mo in T/P91 is substituted by W, has an higher allowable stress and can operate up to steam temperatures of 620°C [12]. Alloy E911 is an European alloy similar in composition to T/P92 with a similar behaviour. At temperatures higher than 620°C, 9%Cr steels become limited by their oxidation resistance and usually 12%Cr steel and austenitic steels are used.

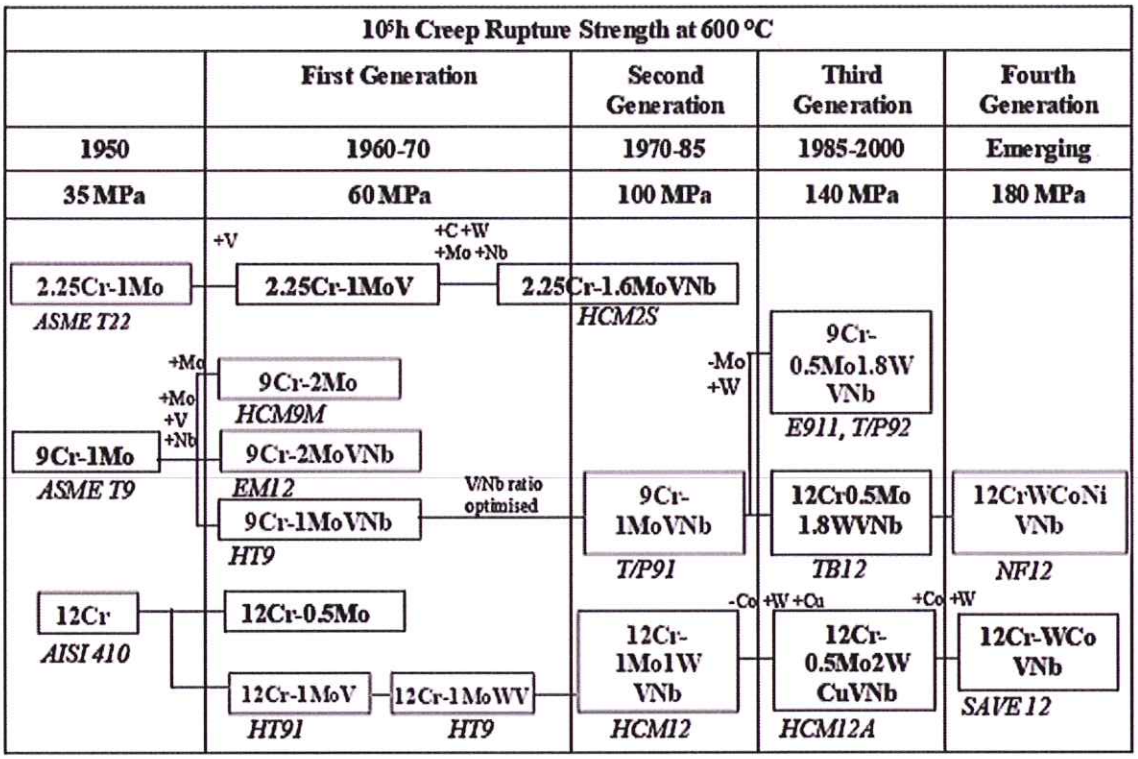

Figure I.2 : Historic development of 9%Cr steels grade [8].

Figure I.2 and Table I.1 give a synthesis of the evolution over years of the formulations of steels used in power plants. 12% Cr steels are widely used for tubing, heaters, and piping in Europe but they are less used in Japan and in USA due to their poor weldability and creep properties. Alloy HCM12 is an improved version of HT91 with 1% W and 1% Mo, with a duplex structure of δ ferrite and tempered martensite with improved weldability and creep strength. Creep strength was increased by substituting most of Mo with W and addition of Cu. It resulted in Alloy HCM12A (P-122), which can be used for heater and piping up to 620°C.

	Steels	Specification ASME	JIS	C	Si	Mn	Cr	Mo	W	Co	V	Nb	B	N	Others	Manufacturers
1-1/4 Cr	T11	T11	···	0.15	0.5	0.45	1.25	0.5	···	···	···	···	···	···	···	
	NFIH	···	···	0.12	···	···	1.25	1.0	···	···	0.20	0.07	···	···	···	Nippon Steel
2Cr	T22	T22	STBA24	0.12	0.3	0.45	2.25	1.0	···	···	···	···	···	···	···	
	HCM2S	T23	STBA24J1	0.06	0.2	0.45	2.25	0.1	1.6	···	0.25	0.05	0.003	···	···	Sumitomo
	Tempaloy F-2W	···	···	···	···	···	2.0	0.6	1.0	···	0.25	0.05	···	···	···	NKK
9Cr																Vallourec
	T9	T9	STBA26	0.12	0.6	0.45	9.0	1.0	···	···	···	···	···	···	···	Mannesman
	HCM9M	···	STBA27	0.07	0.3	0.45	9.0	2.0	···	···	···	···	···	···	···	Sumitomo
																Vallourec
	T91	T91	STBA28	0.10	0.4	0.45	9.0	1.0	···	···	0.20	0.08	···	0.05	0.8Ni	Mannesman
	E911	···	···	0.12	0.2	0.51	9.0	0.94	0.9	···	0.20	0.06	···	0.06	0.25Ni	Sumitomo
	NF616	T92	STBA29	0.07	0.06	0.45	9.0	0.5	1.8	···	0.20	0.05	0.004	0.06	···	Nippon Steel
12Cr																Vallourec
	HT91	(DIN × 20CrMoV121)		0.20	0.4	0.60	12.0	1.0	···	···	0.25	···	···	···	0.5Ni	Mannesman
																Vallourec
	HT9	(DIN × 20CrMoWV121)		0.20	0.4	0.60	12.0	1.0	0.5	···	0.25	···	···	···	0.5Ni	Mannesman
	Tempaloy F12M	···	···	···	···	···	12.0	0.7	0.7	···	···	···	···	···	···	NKK
	HCM12	···	SUS410J2TB	0.10	0.3	0.55	12.0	1.0	1.0	···	0.25	0.05	···	0.03	···	
	TB12	···	···	0.08	0.05	0.50	12.0	0.50	1.8	···	0.20	0.05	0.30	0.05	0.1Ni	
	HCM12A	T122	SUS410J3TB	0.11	0.1	0.60	12.0	0.4	2.0	···	0.20	0.05	0.003	0.06	1.0Cu	Sumitomo
	NF12	···	···	0.08	0.2	0.50	11.0	0.2	2.6	2.5	0.20	0.07	0.004	0.05	···	Nippon Steel
	SAVE12	···	···	0.10	0.3	0.20	11.0	···	3.0	3.0	0.20	0.07	···	0.04	0.07Ta, 0.04Nd	Sumitomo

Table I.1 : Nominal chemical composition in of ferritic steels for boilers [12]

Two alloys NF12 and SAVE 12 which have higher creep strength than HCM12A are still in developmental stage. Alloy NF12 contains 2.5%Co, 2.6% W. Alloy SAVE 12 contains 3% Co and 3% W and minor amounts of Ta and Nb. These elements help to strengthen it by forming fine and stable nitride precipitates [8, 12]. If weldability and creep strength have until now been the main criteria for choosing construction materials for power plants, the oxidation resistance behaviour of those steels at high temperature in steam become important elements of choice for the efficiency and lifetime of the plants.

I.2 High temperature corrosion general knowledge.

When exposed to high temperature, metallic materials react with their surrounding environment. They are exposed to more or less aggressive and complex atmospheres composed of gas such as O_2, N_2, CO_2 in air, or S_2, SO_2, NO_x or other combustion exhaust gases which can cause their total degradation. This phenomenon is called corrosion by hot gases or dry corrosion.

This study will focus on the effect of air and air enriched with water vapour or pure steam on 9%Cr steel grade. An important place will be given to the characterization of the oxide layers grown in such severe condition; and to the understanding of the oxidation mechanisms occurring in those systems.

I.2.1 Thermodynamics considerations and oxidation mechanisms.

General equation for the reaction between oxygen and metals could be written as follow [13-14]

$$\frac{2a}{b}M_{(s)} + O_{2(g)} \leftrightarrow \frac{2}{b}M_aO_{b(s)} \quad \text{Eq. I.1}$$

Where : M : metallic atom
M_aO_b : corresponding oxide

The oxidation process occurs in several steps. Oxygen is firstly adsorbed and dissociated at the metal surface. Germination of oxide nuclei occurs by reaction between the substrate and the gas, followed by a bi-dimensional growth which will form a thin and adhering film. The oxide layer will thicken with diffusion of ions (metallic cation and oxidant anions) within the scale.

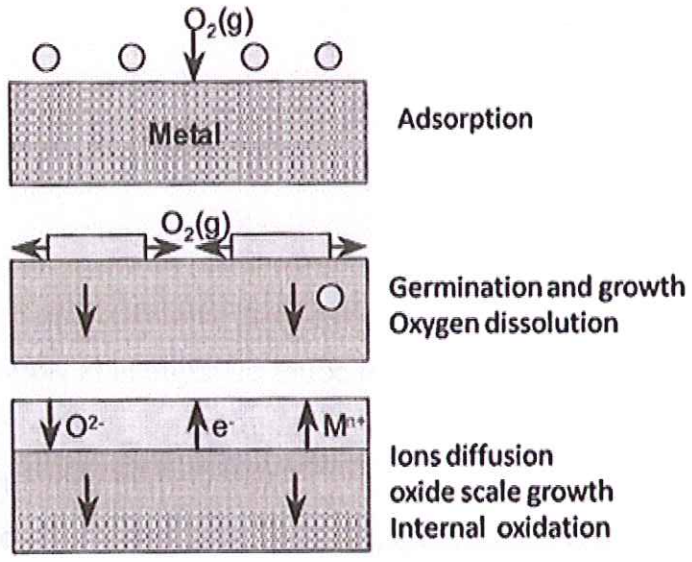

Figure I.3 : general reaction between oxygen and metal schematic, after Kofstad [13].

The diffusion phenomena are not always the same and depend of the metal/oxidant systems. The gas/oxide interface, the oxide/metal interface or the oxide scale itself can intervene in the process. Diffusion is possible thanks to defects in the crystalline structure (vacancies, interstices, dislocations, grain boundaries etc…) [13, 16-17].

When it is the oxide/gas interface which is involved in the oxide growth, mainly metallic cations migration is observed. Two distinct mechanisms can be described (cf. Figure I.4 arrow 1):

- Oxygen is reduced at the surface and linked to the metallic cations of the oxide film: vacancies and electron holes are created at this interface and will migrate through the scale to the oxide/metal interface. The substrate will then be oxidized and form metallic cations M^{n+} by reacting with these electron holes previously generated. Outward diffusion of M^{n+} ions is at the origin of vacancy generation at the metal/oxide interface.

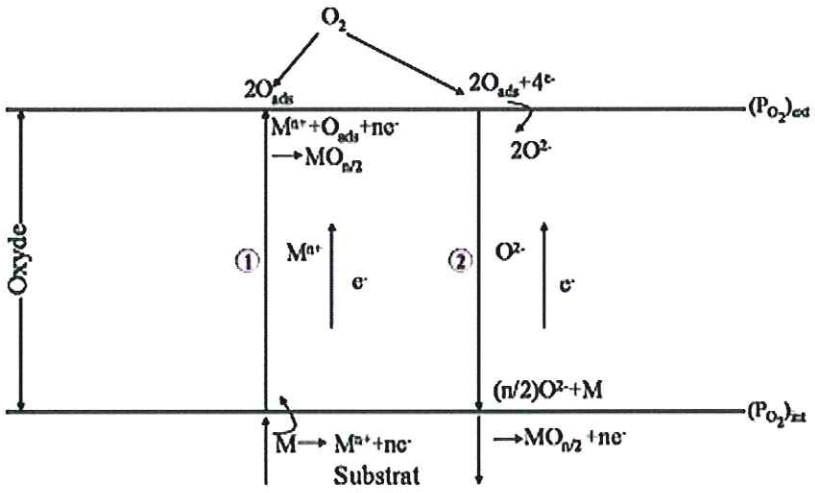

Figure I.4 : Diffusion mechanism in an oxide layer [19]

- In the other case, outward migration of metallic cations occurs through interstices generating stress in the crystalline lattice. Those cations react with the oxygen at the oxide surface.

In both previous cases, cavities or pores are created at the metal/oxide interface due to coalescences of the vacancies generated via the outward diffusion of the metallic ions. This phenomenon is detrimental to the oxide layer adhesion on the substrate.

When it is the metal/oxide interface which is involved in the oxide growth, mainly inward oxygen anions O^{2-} diffusion occurs (cf. Figure I.4 arrow 2). At this interface, cations react with O^{2-} of the oxide and create vacancies and/or electron holes, which migrate to the oxide/gas interface through the scale. Recombination between those holes or vacancies and the gas occurs and is at the origin of formation and the inward diffusion of O^{2-}.

The last case is the result of both processes: inward anions diffusion and outward cations diffusion. This leads to the formation of the oxide in the oxide scale itself.

Cracks and micro-cracks can occur in the oxide scale, their spreading to the oxide/metal interface can result in the spalling of the oxide scale. Formation of volatile and or fusible oxide layer during the oxidation reaction is also a possibility. Thus consumption of the metallic alloy and important degradation of engineering components could be observed in those cases (Figure I.5).

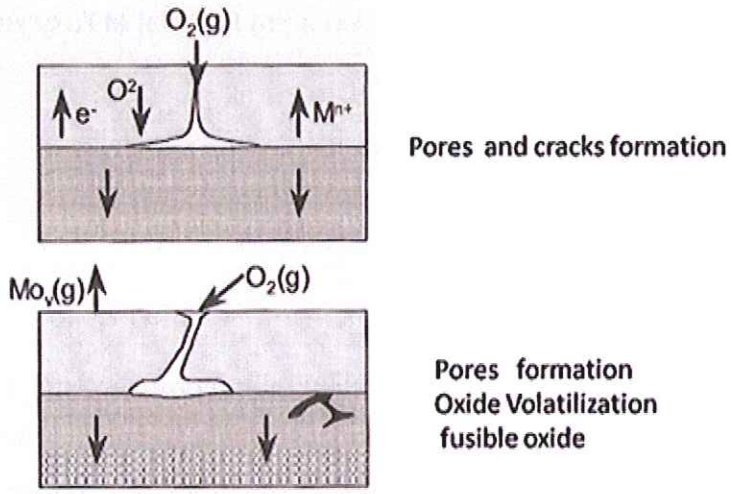

Figure I.5: Defects formation within the oxide scale, after kosftad [13].

Thermodynamically speaking, at the equilibrium, an oxide will form on the surface of a metal if the oxygen potential in the environment is higher than the oxygen partial pressure in equilibrium with the oxide. The Gibbs, free energy of the reaction of oxidation (cf. Eq.I.2) allows to determine the oxide stability.

$$G_r = \Delta_r G° + RT \ln \frac{a_{M_aO_b}{}^{2/b} P_0}{a_M{}^{2a/b} p_{O_2}} \qquad \textbf{Eq. I.2}$$

Where:

G_r : Gibbs free energy of reaction (J.mol^{-1})

$\Delta_r G°$: Variation of standard Gibbs free energy (J.mol^{-1})

R : Gas constant : 8,31 (J.mol^{-1}.K^{-1})

T : Temperature (K)

$a_{M_aO_b}$ and a_M : activities of the oxide and the metal respectively

$\frac{p_{O_2}}{P_0}$: Oxygen partial pressure (Pa)

If the activities of the metal and the oxide are taken as a unity, the previous equation may be used to express the dissociation pressure of the oxide; in other words, the pressure at which the metal and oxide coexist.

$$\Delta_r G° = RT \ln p_{O_2} \quad \text{Eq. I.3}$$

Po_2 may be obtained from Ellingham diagrams (Figure I.6) which is a plot of standard free energies for the formation of oxides versus temperature.

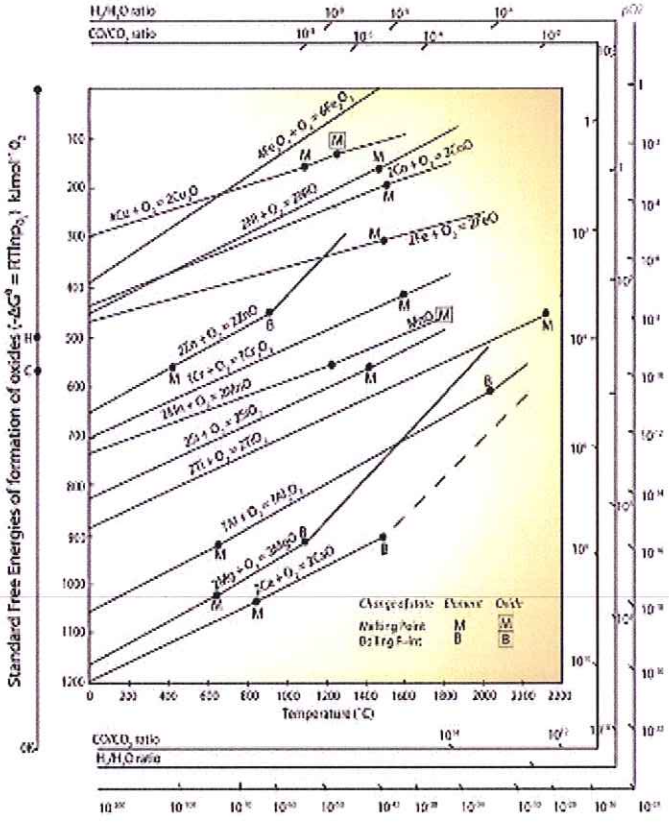

Figure I.6: Temperature dependence of standard free energy of formation of selected metal oxides (Elligham-Richardson Diagram) [20]

Thermodynamically stable oxides (Al_2O_3, SiO_2, Cr_2O_3) possess the largest negative values of $\Delta_r G°$. For designing industrial alloys, important information could be obtained from Ellingham diagrams. Iron, nickel, cobalt which are the alloy bases for many widely used materials, form oxide which are less stable than the oxides of some alloying element such as Cr, Al, Si etc.... When present in optimized concentration, these elements can form protective oxide scale over the base material. This is the main spirit of alloy design for application at high temperature in a corrosive atmosphere. Moreover, to be protective the oxide growing over the material should be adherent, dense and stable.

From thermodynamic calculations mentioned above, it is possible to predict whether the reaction between metal and oxygen can take place. However, to obtain comprehensive information about high temperature corrosion of metals and to protect the materials from its destruction, it is necessary to study the reaction kinetics of the oxide formation.

I.2.2 Kinetics considerations

Oxidation kinetics studies are of high importance for understanding the formation of oxide scale. Kinetics data and thus oxidation mechanisms could be different for a compact or a porous oxide layer [16]. For a porous scale, the diffusion of species is instantaneous and chemical reactions at one of the interfaces are the limiting steps. In the case of dense oxide layers, it is the diffusion of species within the growing scales which is the limiting step.

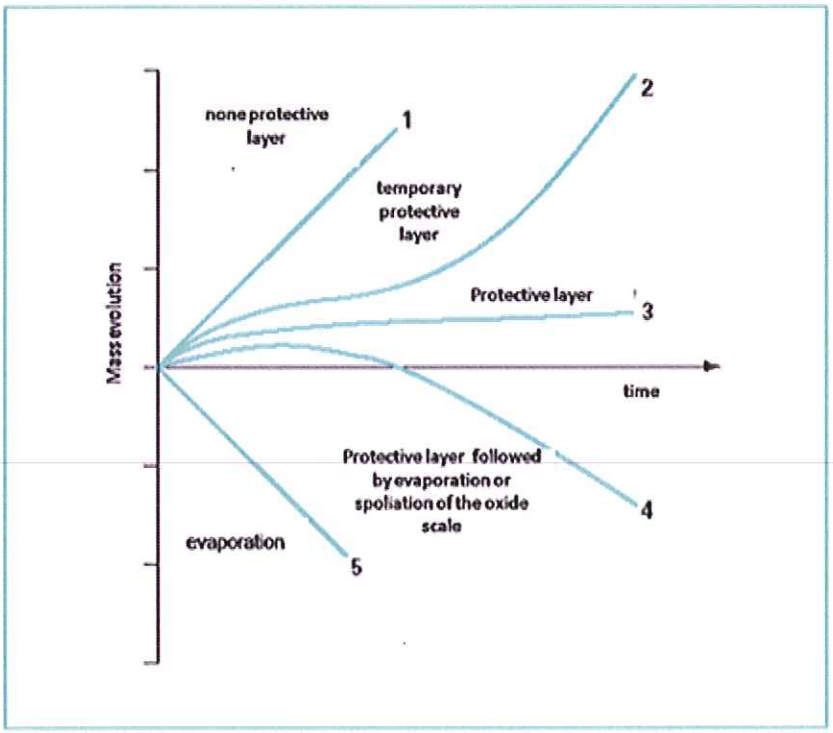

Figure I.7: Theoretical kinetic curves [21]

Two main kinetics behaviours are usually described for plane samples [17, 22]. The first one is called parabolic (c.f. curve 3 in Figure I.7), regime for which diffusion of species within a growing layer is the limiting step of the oxidation reaction. It corresponds to the growth of a protective, dense and stable oxide layer. In this case, the relationship between mass evolution on surface area (Δm/A) of a sample and the exposure time (t) is:

$$\left(\frac{\Delta m}{A}\right)^2 = k_p t \qquad \text{Eq. I.4}$$

Where:

k_p is the parabolic rate constant of oxidation, in $g^2.cm^{-4}.s^{-1}$.

The second kinetic regime law, called linear, (curve 1 Figure I.7) for which the chemical reaction of oxidation over one of the interfaces (gas-oxide and/or metal-oxide) is the

limiting step in the process of oxidation. This case corresponds to a non protective porous and poorly stable oxide scale. In this case, the relationship becomes:

$$\left(\frac{\Delta m}{A}\right) = k_l t \qquad \textbf{Eq. I.5}$$

Where:

k_l is the linear rate constant of oxidation, in $mg.cm^{-2}.s^{-1}$ or $g.cm^{-2}.h^{-1}$.

These rate constants are calculated from the slope of the curves $\left(\frac{\Delta m}{A}\right)^2 = f(t)$ and $\left(\frac{\Delta m}{A}\right) = f(t)$ for the parabolic and linear kinetic behaviour respectively. But, for parabolic cases, Pierragi [21] showed that a calculation from the slope of the curve $\left(\frac{\Delta m}{A}\right)^2 = \sqrt{t}$ gave a better approximation of k_p after the transition regime. However, the obtained curve is not often linear, in which case the oxidation rate is linked to a combination of simple kinetic laws [19, 24]:

$$t = cnste + \left(\frac{1}{k_l}\right)\left(\frac{\Delta m}{A}\right) + \left(\frac{1}{k_p}\right)\left(\frac{\Delta m}{A}\right)^2 \qquad \textbf{Eq. I.6}$$

In this particular case two distinct phenomena can impact the reaction of corrosion kinetic:

- The first one, which is a chemical reaction in the first step of the oxide growth, described by $\left(\frac{1}{k_l}\right)$ in the equation 1.6. This can reflect a possible chemical reaction at one of the metal/oxide or oxide/ gas interfaces

- The second one is due to a diffusion phenomenon within the scale which is highlighted by $\left(\frac{1}{k_p}\right)$ in the previous equation.

The theory developed by Wagner [25] can connect rate parabolic constant k_c to diffusion coefficients of anions (O^{2-}, S^{2-},…) and cations (Cr^{3+}, Al^{3+},..). Thus, for an oxide type M_aO_b, parabolic rate constant can be expressed:

$$k_c = \left(\frac{M_{oxide}}{M_O \times \rho_{oxide}}\right)^2 k_p \qquad \textbf{Eq. I.7}$$

and to Wagner's theory,

$$k_c = \frac{1}{2}\int_{P'_{O_2}}^{P''_{O_2}} \left[D_{anion} + \left(\frac{b}{a}\right) D_{cation} \right] d \ln P_{\grave{a}_2} \qquad \text{Eq. I.8}$$

Where:

k_c = parabolic rate constant in $cm^2.s^{-1}$,

a= 2 and b = 3 (for Cr_2O_3 for example),

p'_{O_2} oxygen partial pressure of oxide decomposition at metal-oxide interface

p''_{O_2} oxygen partial pressure at the gas- oxide interface.

D diffusion coefficient of species.

I.3 Iron oxidation

Iron is the cheapest most widely used metallic material available in the world. But, pure iron does not find application at high temperature because of its high reactivity. Pure iron forms 3 oxides in oxidizing atmosphere: wüstite FeO, magnetite Fe_3O_4 and hematite Fe_2O_3. The composition of the iron oxide scale is a function of temperature and oxygen partial pressure. According to Massalski [26], wüstite does not form below 560°C and, in this case, oxides formed on pure iron are only magnetite and hematite. Above 560°C, the three oxides are present with closest to the substrate FeO, followed by Fe_3O_4 and Fe_2O_3. This repartition in the oxide scale is due to the oxygen partial pressure and the enrichment in Fe. Due to the importance of iron based materials for construction application, the oxidation of this element has been widely studied. A simple mechanism has been developed as a synthesis of what happens in the scale. Iron ions and electrons migrate outwards through the FeO layer and the Fe_3O_4 layer, whereas in Fe_2O_3 scale there are both iron ions, electrons outwards diffusion and inward oxygen migration [13, 26-31]. Under water vapour oxidizing atmosphere at temperatures above 560°C, kinetic of the oxidation reaction has been observed to be faster than in air. This could be explained by the fact that FeO (which has an important defect concentration) is the only oxide formed in such atmospheres. The protective effect of Fe_3O_4 is absent in that case [32].

I.4 Chromium oxidation

Chromia, Cr_2O_3 (corundum structure), is the main thermodynamically stable oxide of chromium at high temperature. Other oxides CrO_2 and CrO_3 are observed under solid forms at low temperature. Kofstad [13] shows that Cr_2O_3 could change into CrO_3 and volatilize under normal oxidation condition, and especially at temperature higher than 1000°C. Water vapour can increase this phenomenon by adding to the formation of volatile hydroxides and oxy-hydroxydes of chromium [33] ($CrO_2(OH)$ and $CrO_2(OH)_2$). For this reaction, both water and oxygen are necessary. Caplan et al. [34] shows that in argon enriched with water vapour atmosphere, the volatilization phenomenon is not visible. The growth of chromia scale is considered following a parabolic kinetics law [10]. In the literature, the parabolic rate constant calculated could vary from 4 orders of magnitude between 10^{-11} to 10^{-15} $g^2.cm^{-4}.s^{-1}$ [35-37]. They all give an activation energy around 250 $kJ.mol^{-1}$ [36]. Cr_2O_3 scale growth mechanism is proposed to be due to a mixed migration phenomenon with an outward Cr cation diffusion and an inward O ion diffusion. Thus leading to the formation of chromia at the internal and external interface and within the scale itself [37, 38]. Cr outward migration can create defects at the metal/oxide interface which can create vacancies and provoke scale spallation [37].

I.5 Iron-chromium alloys oxidation

I.5.1 Chromia forming alloys

Addition of chromium in iron changes its behaviour at high temperature in oxidizing atmosphere by decreasing its oxidation rate. However, the oxide scale structure changes with the amount of chromium. Indeed, chromium is an α-gene element; when its nominal value is higher than 12% in weight within the alloys, it is the ferritic structure which is stable at high temperature. Whereas for lower amount of chromium, austenitic phases could be formed at temperature higher than 850°C, and could affect both the alloy mechanical properties and corrosion resistance (Figure I.8). Steels are called stainless when the amount of chromium in the bulk reaches 12% in weight. Nevertheless, in order to have protective dense layers of chromia, it is necessary to have an amount of chromium of around 17 to 20% wt. in the alloy [13, 39].

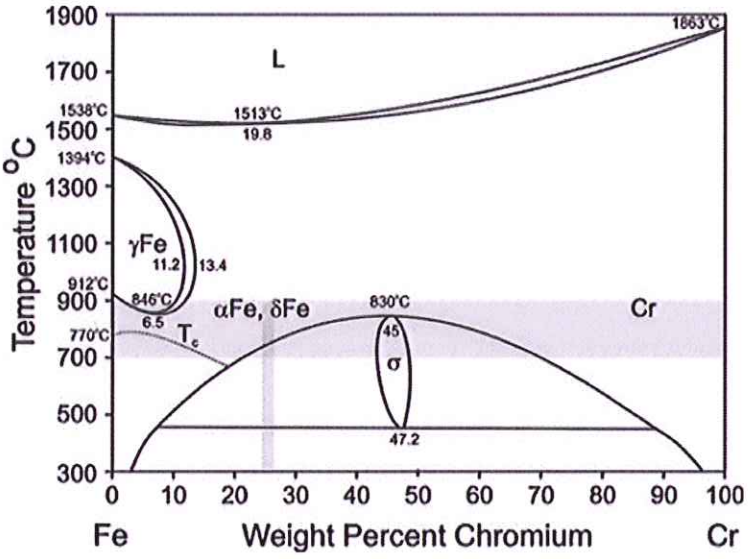

Figure I.8: Iron-chromium phase diagram [40]

One could also note that, at temperature below 800°C, in the case of stainless ferritic steels, formation of a Fe-Cr σ phase (which is an intermetallic compound whose structure is complex and not really defined) can be observed. This σ phase can be at the origin of mechanical weakness and severe acceleration of the corrosion reaction kinetic (Break away).

Meier et al. [40] demonstrated that the formation of this phase σ is highly dependent on the other alloying elements

As a general case, when the chromium content is high enough, the growth of the chromia scale can be divided in three parts:

- Nucleation stage: both iron oxide and chromium oxide appears with a concentration close to the proportion of these elements in the substrate. Indeed if Cr_2O_3 is thermodynamically more stable than the iron oxides, the latter are formed faster than chromia.
- Transitory stage: where the oxide film becomes denser, a preferential oxidation of the chromium is done. Cr_2O_3 grains coalesce to form a uniform film which stops Fe cations diffusion.
- Stationary stage: The chromia scale covers the surface of the alloys [41].

Formation of chromia over stainless steels follows a parabolic kinetics law [17]. Figure I.9 illustrates a list of parabolic rate constant for commercial chromia forming alloys.

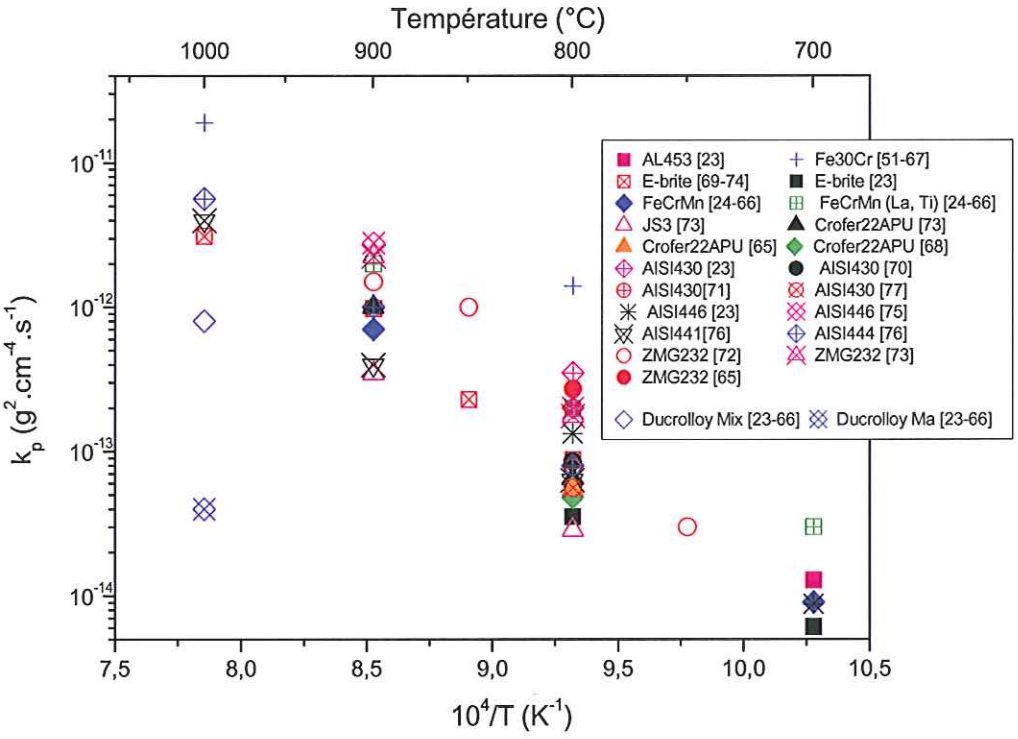

Figure I.9: List parabolic rate constants for several chromia forming alloys.[17,40 ,42-55]

The chromium outward diffusion process through the alloy grain boundaries is considered as the limiting step of the formation of the chromia scale [13, 56-63]. Then, the oxidation reaction takes place at the gas/oxide interface. The oxide grows with a columnar morphology following the c axis of the lattice of Cr_2O_3 [62-63]. Having a small grains alloy could be a way to improve chromium cation outward diffusion [64]. In case of low chromium containing alloy, important density of grain boundaries could be pathway for Cr^{3+} migration and help to form protective oxide layers.

I.5.2 Low chromium containing alloys

For low chromium content alloys, the primary cause of the decrease in the oxidation rates, compared to pure iron oxidation, is the formation of Fe-Cr spinel particles ($FeCr_2O_4$) at alloy oxide boundary. This spinel formation could impede Fe cation diffusion and FeO formation [23, 65]. By all means, little modification of the chromium content in the subsurface of the substrate could have an important impact on the corrosion resistance. The oxidation process consumes Cr, after some time, the chromium concentration falls below the necessary level for forming a protective oxide scale. This depleted zone could be detrimental when cracks or spallation of the scale occur; no healing process can take place. For 9 % chromium steel

several studies were conducted in a large spectrum of atmosphere from dry air to steam, or other gas CO_2/H_2O mixtures . The panel of obtained data can give an idea of the divergence of the opinion about the possibility to use 9% Cr steel at 650°C. Piron Abellan et al. [66] showed that in air for 1000 h , a thin chromium rich oxide scale is present at the surface of its P91 sample. A mixture of iron and chromium oxide were suspected to be part of the temporary protective layer but no clear phases identification or oxide characterization were possible in these thin scales.

In the literature, the presence of continuous layer of manganese and chromium oxide after 10000 h was exposed by Shütze [67], whereas Vossen et al. [68] attested of an important increase in mass gain after 2000h of exposure in dry air, they reported a total mass gain of 0.9 $mg.cm^{-2}$ after 3000 h.

Surface preparation effects were also studied. Grabke [69-70] reported the influence of the surface treatment on the formation of a protective chromia layer within the first oxidation instant. Indeed the chromium diffusion towards the top surface is enhanced with dislocation density [71]. But, everyone agrees on significant changes operating in the corrosion mechanism in water vapour containing environment.

I.6 Effect of water vapour

Several studies were performed over the effect of vapour on chromium containing alloys oxidation behaviour. But, none of the mechanism proposed is enough to explain all the phenomena observed during oxidation in this oxidizing atmosphere. Moreover, a few works deal with the effect of pure steam over 9-12% Cr containing steels. Usually, the results found in the literature are obtained in atmosphere enriched in water vapour, O_2/H_2O, laboratory air/H_2O, H_2/H_2O or CO_2/H_2O. In all cases, the knowledge and the understanding of these results as well as the oxidation mechanisms proposed are of most importance for any investigation of low Cr steels supposed to be used as structural materials for heat exchanger.

During high temperature oxidation in atmosphere enriched in water vapour, the kinetic of the reaction could be split in two different parts: a first one, following a parabolic law which is characteristic of a protective growing layer, followed by a linear part, which is characteristic of the acceleration of the corrosion mechanism [72].This kinetic accident is named "breakaway". Otsuka [73] showed that the parabolic rate constant calculated for the protective stage under water vapour is higher than the one calculated for dry air at the same temperature.

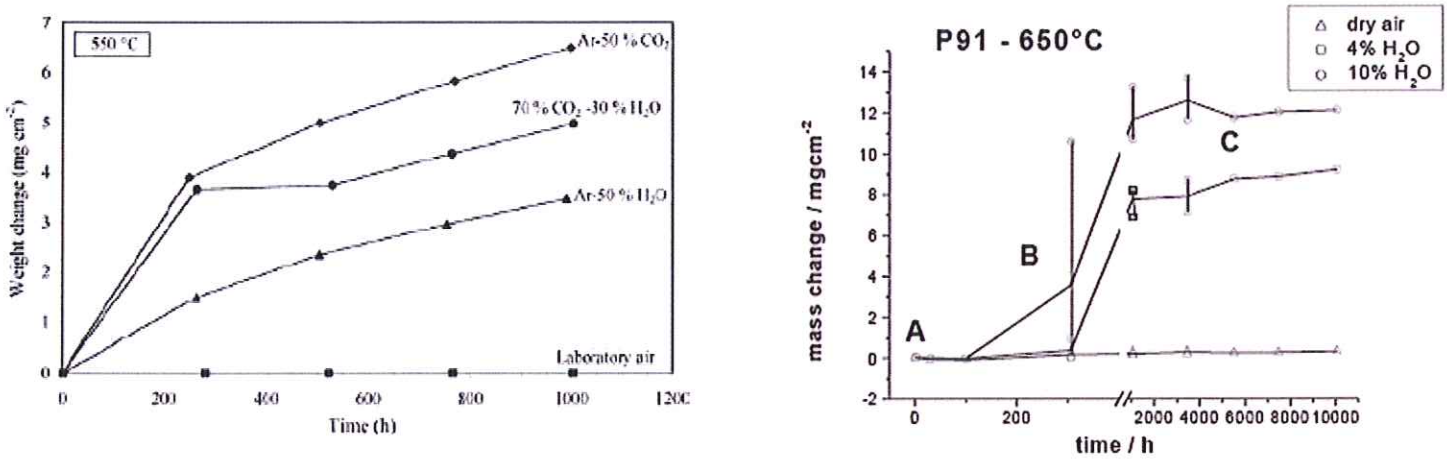

a) b)

Figure I.10 : a) Kinetics of oxidation for 9%Cr steels in different atmosphere at 550°C [66]; b) kinetics of oxidation for 9%Cr steels at 650°C function of the water vapour percentage in the atmosphere [75]

Cory and al. [74] give a $k_p = 1.7x10^{-13}$ $g^2.cm^{-4}.s^{-1}$ for Fe9Cr1Mo steel oxidized at 501°C in water vapour containing atmosphere.

As a general trend, mass gain is higher in wet hot gases atmospheres than in dry hot gases. Therefore, a detrimental effect of H_2O on high temperature behaviour was highlighted in different works (Figure I.12 a))

Schütze et al. [75] showed that increasing the water vapour content from 0 to 4 and 10 % in air lead to an acceleration of the breakaway oxidation for 9 % Cr steels. At 650 °C, 4 % and 10 % water vapour lead to the beginning of breakaway after 100 and 300 hours of oxidation, respectively.

The breakaway phenomenon is quite often explained by Cr depletion in the substrate. The cracking of the protective layer, or its spalling, could not be healed by the formation of chromia because of the low chromium content of the base material [72, 76]. It was also proposed that the formation of chromium oxyhydroxides is the main reason for the breakdown of the protective oxide layer over 9% Cr steel in steam [77, 78] or in O_2 enriched in water vapour [79, 80].

Other studies highlighted a "bell shape"(Figure I.11) dependence of the oxide kinetics growth as function of the temperature and oxygen partial pressure under steam atmosphere [81,82]. This means that the oxidation does not steadily increase with increasing temperature or water vapour content in the atmosphere. This could be related to differences in chromium distribution in the inner part of the oxide scale.

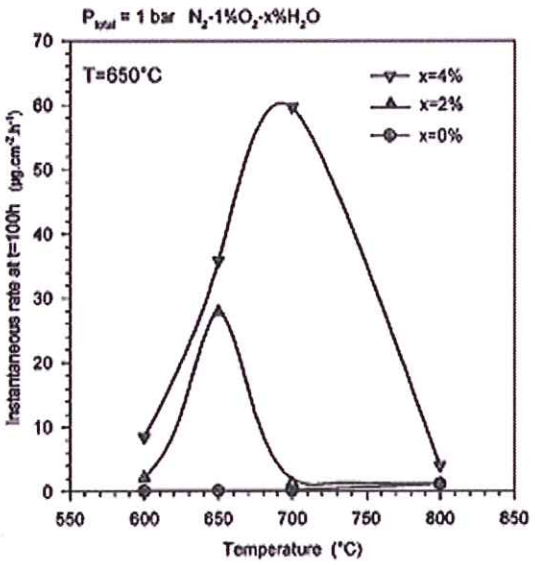

Figure I.11: Influence of water vapour on the oxidation rate of P91 in a N2-1%O2-x%H2O mixtures, between 600°C and 800°C after Nickel [81].

Nickel et al. [81] developed a theory according to which the nature of the defects in the scale could be changed by water vapour (from oxygen defects to substitutional hydroxide) and, thus, the diffusion phenomenon at the origin of the oxidation process increased the reaction kinetic. Henry et al. [82] also stated that hydroxide OH^- could substitute oxygen anions in the layer and easily diffuse, following the Grotus mechanism [84, 85] in the scale because of its effective electrical charge and its size (0.095 nm OH^- for 0.140 nm for O^{2-}). If the ratio H_2O/O_2 is high, the kinetic of the oxidation process increases and the chromium depletion of the substrate follows the same trend. The hypothesis of hydrogen dissolution in the scale being a catalytic way to increase the oxidation reaction was also developed in Hultquist [86] and Larring [87] studies.

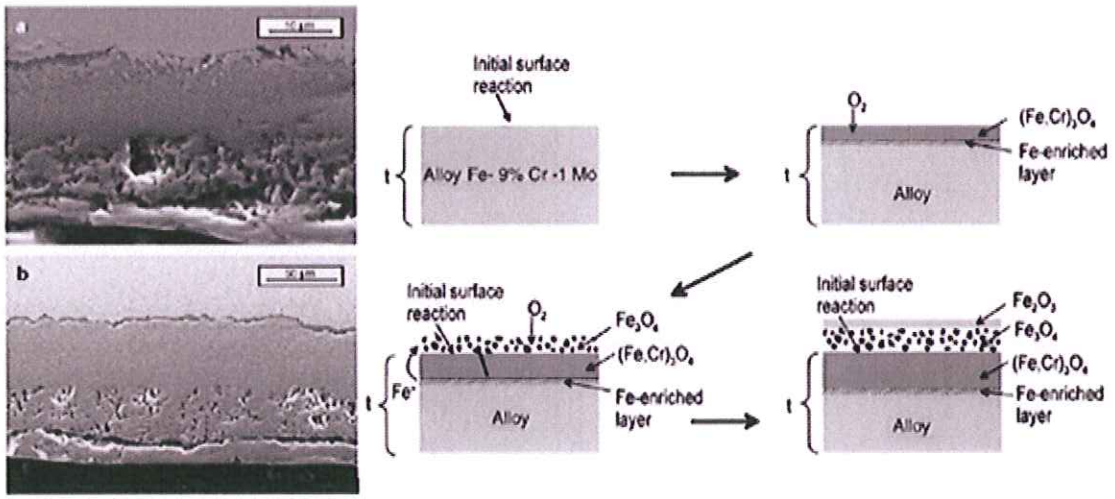

Figure I.12: SEM micrograph (top: substrate, bottom: outer oxide layer) and oxide formation mechanism on T91 in steam from Laverde et al. [88].

Laverde et al. [64, 88-90] characterized three oxide layers in the oxide scale after isothermal oxidation of T91 in steam saturated atmosphere between 595 and 700°C. Whatever the time or temperature exposure, $(Fe,Cr)_3O_4$, Fe_3O_4, Fe_2O_3, were observed (from the substrate to the gas/oxide interface). The micrographs in Figure I.12 show a thick and dense oxide layer close to the substrate with a fractured interface oxide/substrate. The second oxide layer is porous. Another fractured layer is seen between the second and the third oxide layer. Porosity could be explained by the growing layer mechanism proposed in Figure I.14. Magnetite reacts with water to give hematite and hydrogen. The release or the caption of hydrogen regenerates porosities in the two iron oxides layer [88]. A theory is developed based on the dissolution in the oxide layer of the hydrogen contained in steam [86, 87, 89]. Micro-channels formed during the growth of Cr_2O_3 in the first stages of oxidation could be path-ways for water vapour diffusion [89]. Iron reacts with the water vapour and forms porous oxides following the equation:

$$3H_2O + 2Fe \rightarrow Fe_2O_3 + 3H_2 \quad \text{Eq. I.9}$$

The previous formed chromia can be reduced by the produced hydrogen following this equation:

$$Cr_2O_3 + 3H_2 \rightarrow 3H_2O + 2Cr \quad \text{Eq. I.10}$$

In this case, water vapour is considered like a catalyst for iron oxidation. But, no substantial proof of this effect over 9%Cr steels has been developed. Quadakkers et al. [91] have proposed another theory. Figure I.13 is a schematic which resumes their theory. Breakdown of the protective spinel layer is accompanied by formation of a rapidly growing magnetite layer and an inner scale consisting of Cr_2O_3 precipitates in an "FeO-matrix".

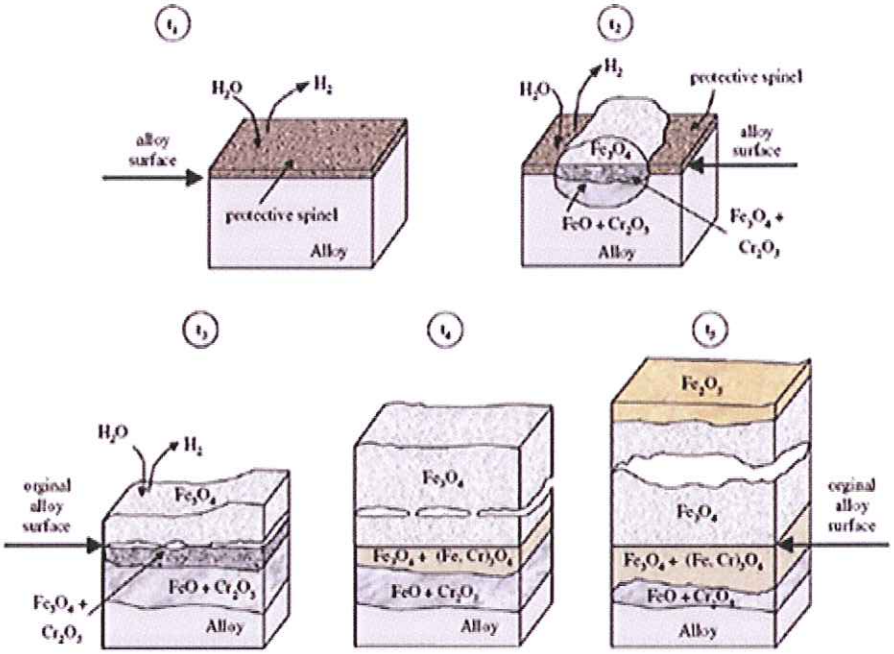

Figure I.13 : Schematic illustration showing scale formation of 9-12%Cr steels in Ar-H_2O mixtures in the temperature range 550-650°C. Exact mechanisms and times depend on steel composition and exposure temperature. In case of 10Cr-Mo-W steel at 650°C the time t5 is approximately 2-5h, after Quaddakers [91].

The inner and outer layers are separated by a gap, which could be caused by vacancy condensation resulting from rapid growth rate of the outer magnetite layer. Further growth of the scale depends to large extent on transport processes within this gap, where the so called "H_2/H_2O brigdes" proposed by Rahmel and Tobolski [92], and illustrated in Figure I.14 provide the transport mechanism.

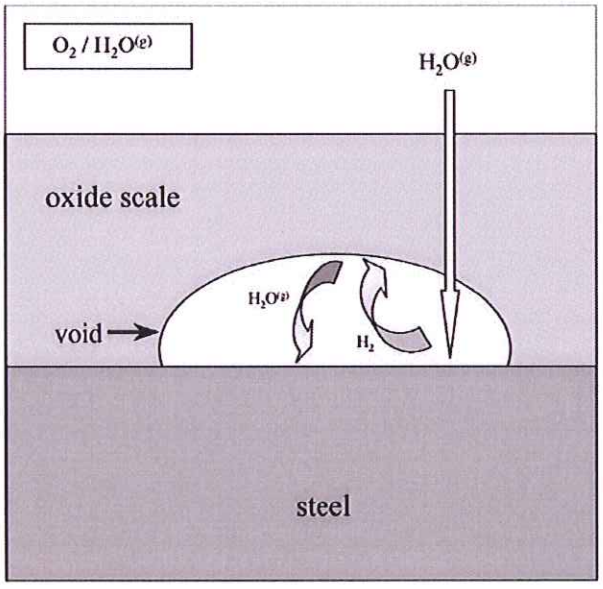

Figure I.14: Illustration of the Rahmel and Tobolski mechanism in O_2/H_2O atmosphere [93].

Moreover, molecular gas transport occurs through the outer scale [94]. As the overall scale thickness increases, Fe-activity at the scale/gas interface gradually decreases due to the

increasingly difficult of Fe cation transport in the oxide surface as a result of the presence of the large gap that develops (Figure I.13). The decrease in iron activity gradually results in formation of hematite, which is the oxide in the equilibrium with the gas atmosphere, on top of the scale. The further development of the layer now depends very much on the temperature. Upon prolonged exposure, the scale starts to develop more and more micro-voidages that develop first in the inner scale. Quadakkers [91] highlighted that the pore distribution was very dependent upon alloy purity and scale and/or the scale/alloy interface coalesce to form pores. The latter seem to be affected by the presence of "condensation-sites" such as carbide precipitates.

Despite the several detrimental effects reported in all those studies, the potential beneficial effects that water vapour could have on oxide scale adhesion to the substrate during cyclic corrosion tests was highlighted. Less spalling was observed by Quadakkers et al. [95] in wet gases than in air. Diminution of the oxide grains size grown in water vapour containing environment was also identified as a possible cause the mechanical resistance during cyclic test because it allows better stress accommodation [96].

I.7 Cyclic oxidation

Cyclic oxidation, corresponding to the worst condition due to thermal shocks [13] which produce acceleration in the oxidation process [17-97]; the phenomena are dependent on the thermal shock amplitude difference and the exposure time. Fractured oxide layers are formed due to differences in thermal expansion coefficients between the constituting layers and the base material. Laverde et al. [88] highlighted this effect of cyclic oxidation under water vapour condition on the structure of the oxide scale grown on P91 (Figure I.15)

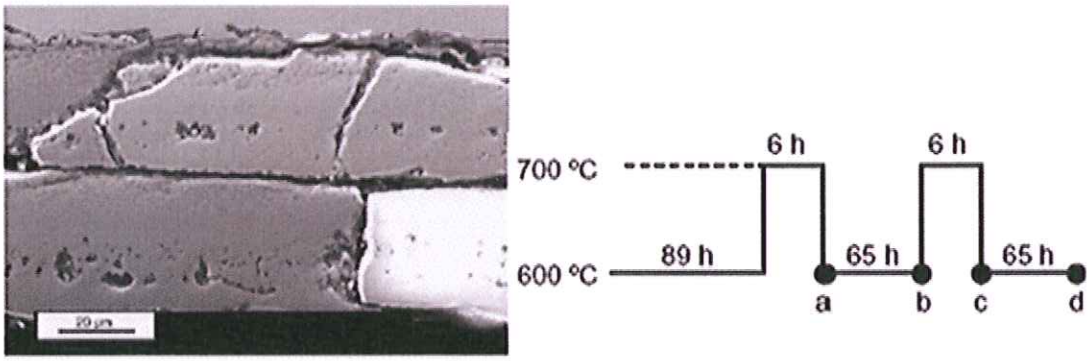

Figure I.15: (left) micrograph of the oxide scale formed after non isothermal oxidation of a specimen under the cyclic condition between 600°C and 700°C (right) [88].

Moreover, they state that any temporary temperature increase or presence of hot spots occurring in practice will produce an acceleration of the oxidation process, causing a decrease in lifetime, which is dependent on the magnitude of the temperature difference and the length of the exposure time at the higher temperature. Depletion of Cr and Fe from the substrate bulk is enhanced in cyclic condition. Oxide spallation occurs and porous iron oxides are formed.
Therefore,ways to in improve the high temperature behaviour of low chromium steel such as T/P91 will be investigated and we will focus on the study and the understanding of solutions, coatings, treatments or alloying element to enhance the corrosion resistance behaviour of the 9% Cr steel without decrease its good creep resistance.

I.8 Coatings against high temperature corrosion

I.8.1 Chromia forming coatings

To preserve the mechanical properties of the engineering component made of 9%Cr steel, a surface treatment with a chromium rich coating (up to 40% in weight) could be realized [98]. The co-extrusion of two materials for realizing an outer tube rich in chromium and an inner tube with high creep strength ferritic steel was proposed by Smith et al. [99]. But, if corrosion protection is necessary to increase life time of the components, the cost these ones matters also from the industrial point of view.
Thermal spray coatings composed of a nickel matrix and a chromium content between 14% to 35% in weight, as used in the aerospace industry, was tested on heat exchanger and boilers [100-102]. But if the corrosion resistance of the coated materials has improved significantly this method show its limitation when transposed to the industry. Indeed, difficulties are faced for coating the inner part of tubes, and the external coating can modify the weldability of these tubes.

I.8.2 Alumina forming coatings

Forming alumina instead of chromia at the top surface of the 9%Cr steel could also be a way to enhance its corrosion behaviour at high temperature. Agüero et al. [103-105] have reported interesting results concerning steam exposure at 650°C of a Fe_2Al_5 coating deposited on 9% Cr steels realized by slurry deposition. The slurry coatings consist in an aluminum

paint which is put on the substrate prior to a heat treatment. This treatment allows aluminum diffusion in the subsurface to create an Al-enriched zone.

Other deposition techniques were also developed based on the Chemical Vapour Deposition (CVD) process and provide promising protection of 9%Cr containing steels at 900°C in wet hot gases [106-107]. Pack cementation for forming aluminide coating is one of those CVD techniques. By this method Al, Cr and Si deposition could be achieved on both outside and inside the steel tube. Moreover, complex coatings based on co-deposition of two or three elements were extensively studied and lead to a better understanding of the element diffusion in the pack during the coating process [108-114].

In the case of low chromium content steel oxidation, once coated with aluminum it could be useful to consider the Fe-Al diagram in Figure I.16. Indeed, the coating zone corresponds to an inter-diffusion zone between the aluminum and the substrate born from the gradient of activities established between the pack and coating/substrate interface.

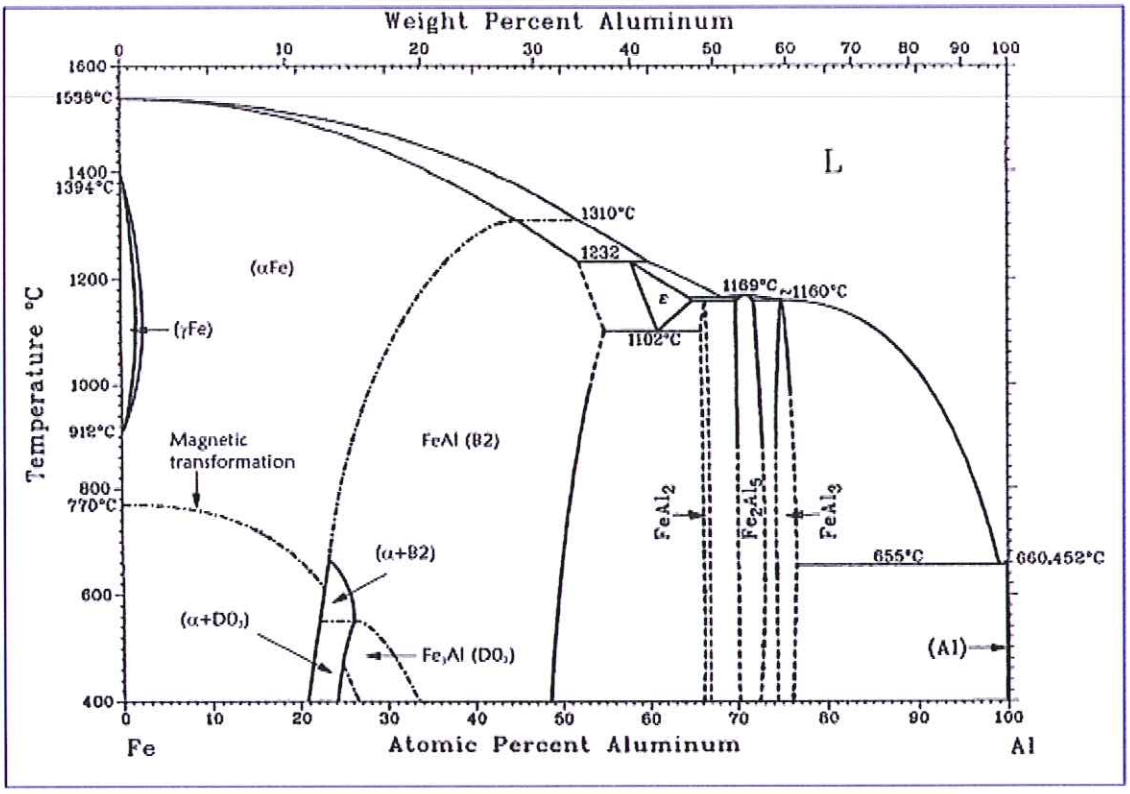

Figure I.16: Binary diagram Fe-Al [115].

Fe_3Al, FeAl, $FeAl_2$, $FeAl_3$, and Fe_2Al_5, and solid solution of Al in Fe are the intermetallic phases which can be formed during the reaction between the aluminum within the cementation pack and the substrate. The formation of those phases is controlled by the diffusion fluxes which depend on the pack mixture composition, the holding time and the temperature of the process.

The oxidation of aluminum containing alloys usually leads to the formation of amorphous or α, θ, γ Al_2O_3 [116-118] depending on the temperature and the oxidizing atmosphere. Nevertheless, it has been reported by Sakiyama et al. [119] that below 700°C, the main oxidation product is the cubic $\gamma-$ Al_2O_3. But hematite, magnetite, hercynite ($FeAl_2O_4$) and amorphous alumina are also identified in the oxide layer. The formation of these oxide are closely related to the amount aluminum in the coating. Several works were carried out to determine the specific threshold where the formation of iron oxide is limited [120-123]. At 700°C, in was highlighted that 5% in weight of aluminum is the minimum concentration above which no iron oxide nodules appears [124].

To improve the aluminide pack cementation coating process, recent works focused their investigation on the possible beneficial effect of rare earth element addition in the pack such as Y, Ce, Hf. Those elements can help to a better aluminum oxide adhesion to the steel and to develop small grain size oxide [125-128].

I.8.3 Metal Organic Chemical Vapour Deposition coatings.

The effect of reactive element will be discussed in further details in the following paragraph. But important works among which Qu et al. [129-130] or again Chevalier et al. [17, 45] show that deposition of rare earth oxide such as ceria or yttria could significantly decrease the oxidation kinetic of steel. Metal Organic Chemical Vapour Deposition (MOCVD) coatings were extensively studied as way to realize thin oxide film of (La_2O_3, Y_2O_3, Nd_2O_3) on metallic substrates [17, 45, 131-133]. The thin film, with or without a heat pretreatment, acts as a barrier, to cations from the substrate, and oxygen anions, diffusion and impede as much as possible catastrophic oxidation.

Even if this process may not have immediate application at the industrial scale, a part of this work will be dedicated to study of the effect of MOCVD coatings on high temperature corrosion of 9% Cr steels.

I.9 Alloying Elements Effects

Coatings are a way to enhance the oxidation resistance of materials, but as discussed in paragraph I.2.5 a slight change in the steel composition could also change its behaviour in aggressive environment. This paragraph will be dedicated to an overview of the different

effects of alloying elements which could be used for changes in the steel composition. But one should bear in mind that modification of steel formulation could also impact its mechanical properties.

I.9.1 Reactive Elements

Reactive elements such as Hf, Zr, etc.... have an important oxygen affinity (free Gibbs energy of oxides are more negative than Cr and Al oxides); they will be oxidized first upon exposure and help to protective oxide nucleation [64]. Chevalier [63] showed that Nd_2O_3 coated Fe-30Cr steel, decreased the oxidation rate at 1000°C from one order of magnitude and improved the oxide adherence by modifying the chromia oxide grains morphology and allowing stress relaxation during cyclic oxidation. Rare earth segregation phenomena, in chromia grain boundaries, which occur at high temperature around (800°C-1100°C) [134-135], decreases the oxidation velocity of the chromia forming alloy (Fe30Cr) and enhances the oxide scale adhesion [104].

Many articles were written over the effect of cerium on high temperature oxidation resistance for chromium steel. Sroda et al. [137] showed in their studies a negative effect of this particular rare earth over ferritic steel oxidation, in simulated combustion atmospheres, especially in HCl containing atmosphere; whereas Sundararajan et al [138], Grabke [64] and Rhys-Jones [139] agreed to the contrary. Indeed, they show through their studies a good corrosion behaviour for 9 % Cr and steel by adding cerium (0.002-0.08 wt %) in the grades, or by nanoceria coatings. Moreover, Wolff et al. [140] showed that by adding mischmetal (0.003% La + 0.008%Ce) in FeCrAl steel grade they improved the adherence of the protective alumina oxide scale. As a general mechanism, this enhanced oxidation resistance could be due to the fact that oxide nucleation process occurring on the alloy surface was favored by Ce or La and their respective oxides (CeO_2 or La_2O_3).

The oxide layer obtained was composed of small grain thank to extra nuclei sites. Beneficial effect over the oxide scale structure due to reactive elements was as well highlighted in Martinez-Villafane researches where small oxide grains were observed after rare earth addition [141, 142] in a Fe13Cr steel. Indeed, they showed that 0.03 % wt of Nd or Pr reduced the oxidation rate of Fe13Cr alloy at 800°C. Moreover, this effect becomes more evident when both reactive elements were mixed in the casting with this proportion: 0.01% wt of Nd and 0.01% Pr.

I.9.2 Sulphur-Phosphorus

At high temperature and during annealing process in chromia forming alloys, elements diffuse from the bulk of the base material. Phosphorous and nitrogen first segregate at the reactive surface followed by S and Sn. Above 800°C, S segregation dominates. Cr, P, N and Sn display a co-segregation mechanism at high temperature [143]. The segregation of S on the surface leads to a site competition with oxygen during chemisorption in the initial stages of oxide scale formation. This phenomenon restricts both the growth and the thickness of the protective oxide layer. S segregation at the metal/oxide can lead to spallation of the oxide at high temperature. Similar phenomena are observed with P [143-145]. Elements such as Ti and Nb show strong interaction with P, keeping P in the grain and decreasing its diffusion at the grain boundary and its surface segregation. In the alloys and steels containing carbon, Ti and Nb form carbides; therefore, with increasing C content, the grain boundary segregation of P increases and thus modifies the corrosion mechanism [146]. One can conclude that there is a need to decrease phosphorus and sulphur content in the alloy to suppress the detrimental effects due to their surface segregation involving instability in the adherence of protective oxide scales.

I.9.3 Tungsten

Tungsten is principally added into FeCr steel in order to enhance mechanical properties. Only a few articles deal with tungsten impact on steel corrosion resistance [147]. They reported that additions of 1.5–2% W seem to be detrimental to oxidation performance of 9–12%Cr steels in steam at 650°C [146, 147]. This statement is in good accordance with Lepingle et al. [90] work which showed that T91 and T92 had higher oxidation rates. In other words their resistance against high temperature oxidation is worse. However, this detrimental effect of W must be cautiously considered. Indeed, when W is added to a steel, Mo is generally not added or added in small quantities and vice et versa. So, as mentioned by Agüero et al. [148], it is difficult to attribute with certainty whether the negative influence on corrosion rates is due to the presence of W or to the lack of Mo in the steel.

I.9.4 Molybdenum

As for tungsten, molybdenum is mainly added in the steel to enhance its creep behaviour [149]. Some data were published on its effect on corrosion resistance properties. Mo seems to be a basic compound of the oxide scales formed on the 9–12%Cr steels during their high temperature corrosion in air and/or in steam [90, 146, 150]. A beneficial effect of molybdenum was observed for austenitic steels at 600°C under waste incineration conditions, but for a content of 6 % wt in the steel [151]. For 16% Cr ferritic steels in humid air, Pint et al. [152] also noticed a beneficial effect of Mo, mainly for tests at very high temperature, i.e. 800°C. For the 2.25 % and the 9 %Cr steels, Lepingle et al. [90] observed that the steels with about 1% Mo (T91) had lower corrosion rates in pure steam at 650°C than similar steels (T92) with much lower Mo content. On the other hand, Schütze et al. [67] recommends keeping the molybdenum content as low as possible in steels when they are used in water vapour containing environments. So with such contradictory information, it is not easy to highlight a clear relationship between Mo or W contents and the oxidation phenomena occurring in low chromium iron based steels.

I.9.5 Manganese

The international high temperature corrosion community is divided over the real effect of manganese as alloying element in low chromium steel during oxidation phenomena. Zurek et al. [82] and Marasco et al. [153] clearly conclude that manganese has a bad effect on the growing of protective oxides scales. Lepingle [90] work investigated the effect of manganese in oxidation resistance of steel under steam oxidizing atmosphere (Figure I.17) and did not give a general trend on the effectiveness of this alloying element. But, focusing on T91 and T92 mass gains and Mn content, a positive effect of manganese can be observed on the high temperature behaviour of T92.

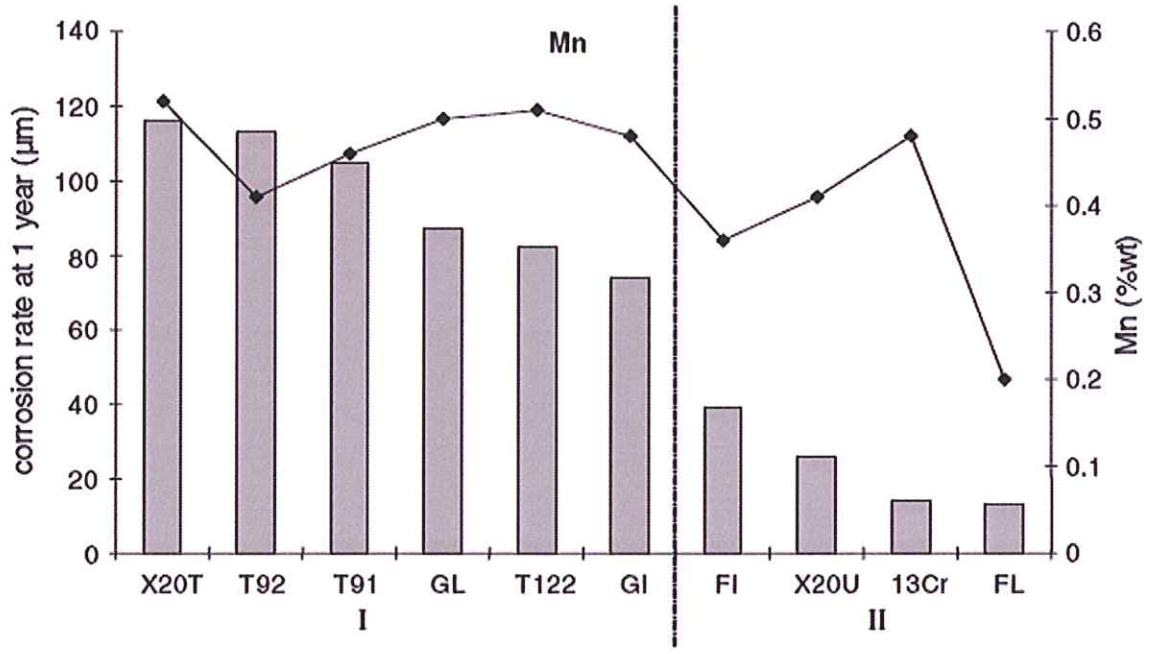

Figure I.17: Relation between the corrosion rate after 1 year of steels exposed at 650°C in steam and their Mn content [90].

Lepingle [90] described manganese as an important alloying element in protection against corrosion because of its participation in the formation, of corrosion products such as manganese chromium spinel. The presence of Mn in a 11% Cr steel, although at a rather low level (0.8%), was considered to be very important in the formation of the surface spinel oxides in air at 600°C [154]. Similar observation was noted for crofer22 (23%Cr content) by Yang et al. [155] by using $(Mn,Co)_3O_4$ oxide coating. Such a coating acts as a mass barrier and inhibits the oxide scale growth on stainless steel and prevents Cr from outward migration. In humid air in the temperature range 700–800°C, beneficial effects were observed for additions of manganese in 16–18%Cr ferritic steels [156]; but the influence of Mn in concentrations varying from 0.1 to 3.5% was unclear [157]. For the 9– 11%Cr steels in steam, manganese is expected to have a positive effect in water containing environments. Indeed, Collins et al. [158] came to the conclusion that Co-Mn oxide coating decreased by a factor 2 the chromium volatility which can occur at around 800°C in humid atmosphere therefore it prevents them from Cr depletion in the substrate.

I.9.6 Vanadium

Following the same trend as W and Mo, vanadium is more a structural element used to increase mechanical properties and strength of the low chromium iron steel [159]. Purmensky

et al. [160] studied steels with Cr, Mo and V in their chemical composition. These steels exposed to high temperatures and submitted to tensile stress, had improved mechanical resistance due the precipitation of Mo_2C carbides in 2.25Cr1Mo steels and V_4C_3 carbides in the Vanadium containing steels. A few papers [159-161] tried to analyze the impact of V on corrosion resistance behaviour on chromia containing alloys. In the engineering science field, it was reported the need to decrease or to suppress the use of vanadium as alloying element because of the catastrophic effect on oxidation which can occur around 660°C and caused by the formation of a fusible oxide: V_2O_5 [161].

I.9.7 Silicon

Its positive influence on oxidation is generally known, in particular for ferritic steels in water vapour [90, 137]. CVD methods were developed for surface treatment of inner tube made of low chromium content steels, and showed improvement in corrosion resistance behaviour [160]. Those good properties could be due to the formation of a uniform SiO_2 at the initial stages of the oxidation which contributes to the growth of a well adherent and dense protective oxide. Indeed, Huntz et al. [163], after studying the effect of different weight percentage of silicon in 9%Cr steel at high temperature, came to the conclusion that the effect of silicon is first due to its diffusion to the surface of the steel and SiO_2 formation at the surface, i.e. oxidation induced surface segregation. Afterwards, when oxidation continues, a chromia scale forms over the silica film, as the oxygen activity thermodynamically imposed by silica is too small for developing iron oxide layers. Thus, as expected from thermodynamics, it forms a continuous inner layer of silica, beneath chromium oxide. But, silicon concentration critical values need to be well defined. Indeed, for Lepingle et al. [90], Si seems to be effective at values above 0.5% (weight %) but, once again, no general trend about Si impact on corrosion resistance in steam oxidizing atmosphere can be extracted from Figure I.18 except by focusing on T91 and T92.

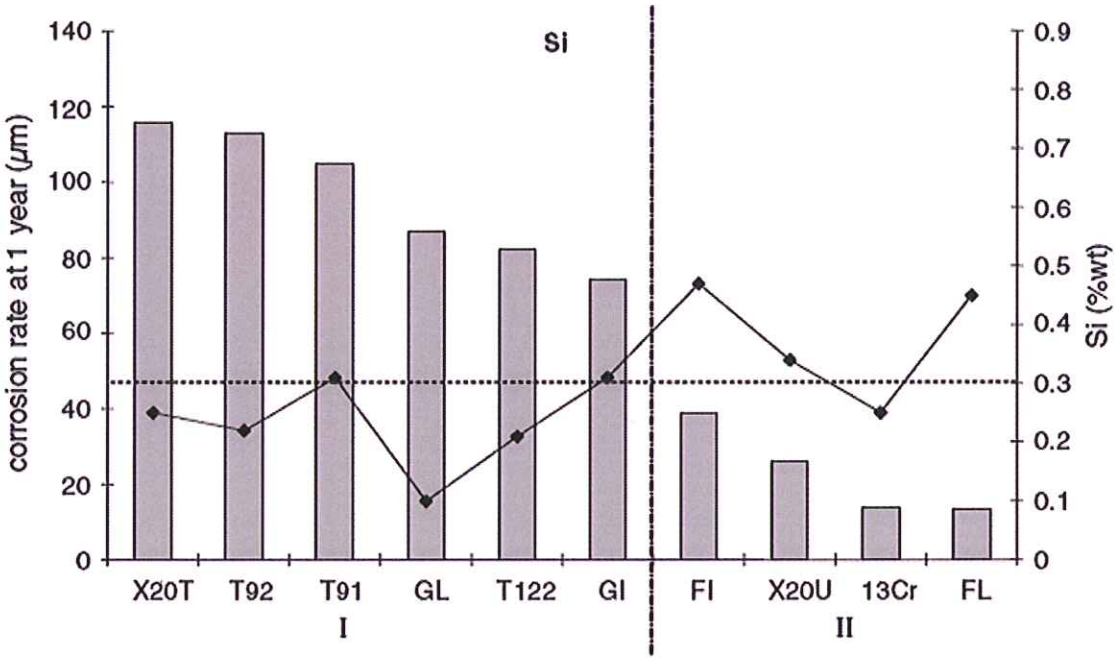

Figure I.18: Relation between the corrosion rate after 1 year of steels exposed at 650°C in steam and their Si content [90].

In this case, Si content seems to be beneficial to T92 oxidation resistance properties. For Huntz et al. [163], 0.5% of silicon is not enough to achieve any protective effect in their studies. Indeed, they defined 3% of silicon as the good amount for an improved oxidation resistance in both O_2 and $Ar/H_2/H_2O$ oxidizing atmosphere at high temperature as shown in the kinetics data Figure I.19. The silicon amount which segregates at the steel surface when heating up to 600 °C is greater for the 3% Si steel than for the 2% Si steel. Moreover, the chromia scale formed on the 2% Si steel has not a good adherence, while spalling is not observed with the 3% Si steel. Moreover, the beneficial impact of silicon addition could be combined with alumina protective effective effect by co-deposition using CVD method on low Cr steel [164].

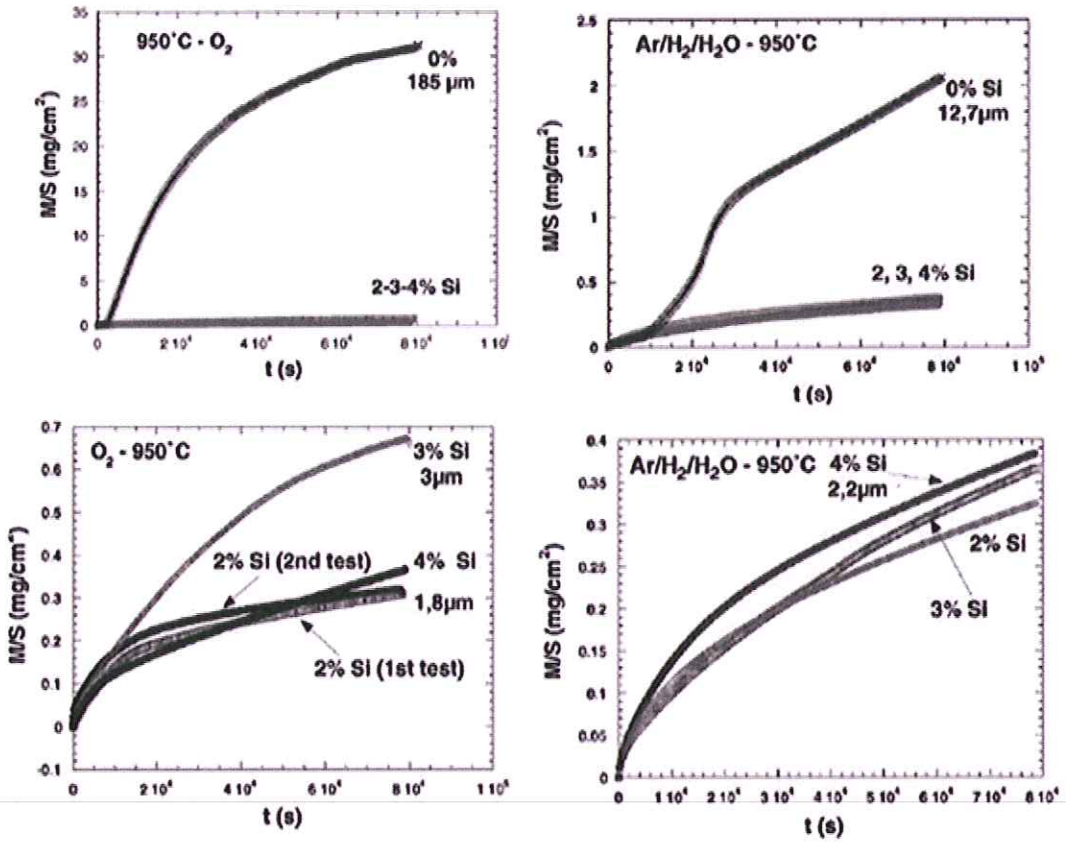

Figure I.19: Evolution of the mass gain with the oxidation time on 9%Cr steel, at 950°C, (left) in O_2, (right) at $Ar/H_2/H_2O$,for samples with various amount of silicon [163].

I.9.8 Aluminum

Aluminum as silicon is well known for its good corrosion resistance properties at high temperature by formation of a thin and dense alumina film [105, 164-169]. Indeed, at 650°C in air for P92 steels, aluminisation of the substrate allows the formation of an aluminide diffusion coating, leading to the growth of adherent alumina scale. Wolff et al. [140] on Fe35Cr and Fe40Cr showed that alloying with Al proved to be effective in increasing the oxidation resistance by up to one order of magnitude. Results support the premise that the oxidation resistance depends on sufficient aluminum content (3 %-5 % wt) to provide a stable Al_2O_3 layer at the surface from the initial transient stage of oxidation, and the development of a secondary chromium oxide layer to provide stability when the aluminum is depleted. Indeed, it should be noticed that high aluminum content formed an alumina which cracked easily during cyclic oxidation, whereas improvement of cyclic oxidation is obtained with low Al content pack chemistry [165, 169]. But, Chang et al. [168] have highlighted, using 9%Cr

in oxidizing atmosphere between 750 and 950°C, the fact that alumina oxide grew at high temperature and that oxidation rate increased by increasing the temperature. The fast scale growth caused high stress which can lead to cracking or spallation in the oxide leading to high mass gain.

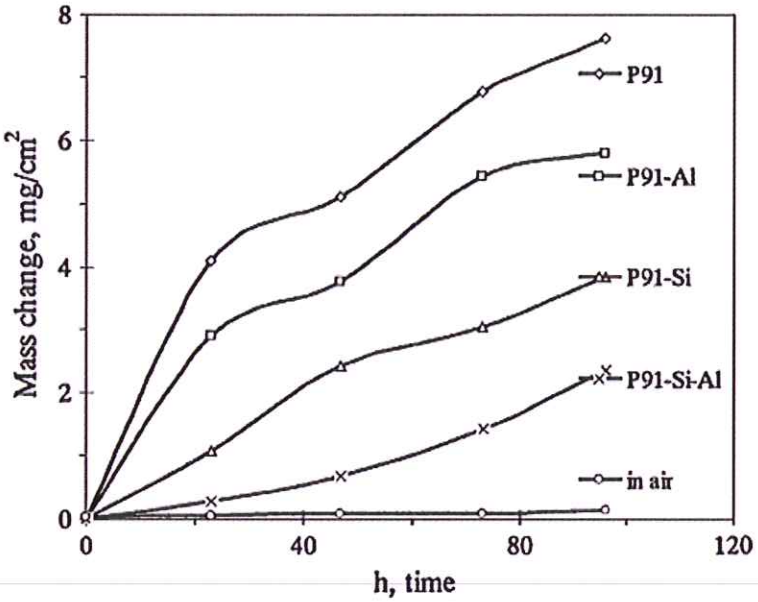

Figure I.20: Mass gain comparison for the different steels exposed in air with KCl vapour for 96 h at 650°C after Li [170].

On the other hand, Li et al. [170] observed, by adding 2.2% Si and 2.2 % Al in the bulk of P91, an important decrease of the oxidation rate, in KCl vapour containing environment at 650°C. Figure I.20 shows the kinetics obtained during their experiments. They came to the conclusion that Si is more effective than Al. The decreased corrosion rate after the addition of Si is attributed to the enrichment of a silica layer at the inner part of the scale, which works by retarding the rapid migration of the reactive species (Cr and Fe cations and oxygen anions).

REFERENCES

[1] http://www.iea.org
[2] J.D. Parker, Materials at high temperatures, 2 (2002) 47.
[3] Protocole de Kyoto à la convention-cadre des nations unies sur les changements climatiques, Nations Unies, 1998. FCCC/INFORMAL/83. GE.05-61647 (F) 070605 090605.
[4] http://en.wikipedia.org/wiki/File:PowerStation2.svg
[5] R. Viswanathan , W.T. Bakker, Proceedings of 2000 International Joint Power Generation Conference, Miami Beach, Florida, July 23-26 (2000).
[6] R. Viswanathan, Advanced Materials and Processes, August (2004) 73.
[7] V. Rhor, PhD thesis, Institut Nationnal Polytechnique de Toulouse, Toulouse, France, 2005.
[8] F.Masuyama, R. Viswanathan and J. W. Nutting, IOM Communication Ltd, London (1999) 33.
[9] P.J. Ennis and W.J. Quadakkers, Proceedings of the 5th Internationnal Charles Parsons Turbine Conference, Cambridge, (2000).
[10] P.J. Ennis and W.J. Quadakkers, VGB PowerTech, 8 (2001) 87.
[11] K. Haarman, J.C. Vaillant and B. Vanderberghe, Vallourec&Mannesmann Tubes (2002).
[12] R. Viswanathan and W. Bakker, Journal of Materials Engineering and Performance,10 (2001) 81.
[13] Kofstad : High Temperature Corrosion, Elsevier Applied Science (1988).
[14] P. Sarrazin, A. Galerie, J. Fouletier : Mechanisms of high temperature corrosion, Trans Tech Publications, Zürich, Switzerland (2008).
[15] Developments in high temperature corrosion and protection of materials, édité par Wei Gao et Zhengwei Li, Woodhead Publishing in materials, Cambridge, England (2008).
[16] P. Sarrazin, A. Galerie, J. Fouletier : Les Mécanismes de la Corrosion Sèche, une approche cinétique, EDP Sciences (2000).
[17] S. Chevalier : Traitements de surface et nouveaux matériaux : Quelles solutions pour lutter contre la dégradation des matériaux à haute température, Editions Universitaires de Dijon, collection Sciences, Dijon (2007).
[18] P. Kofstad : Nonstoichiometry. Diffusion and Electrical Conductivity in Binary Metal Oxides, Ed. Springer, Berlin (1997).
[19]K. Messaoudi, PhD thesis, University of Paris XI Orsay, Paris, France (1997).
[20] A.S Khanna, Introduction to High Temperature Oxidation and Corrosion, ASM International, US, 2002.
[21] L. Antoni, A. Galerie : Techniques de l'Ingénieur, Traité Matériaux Métalliques, M 4220, 1.
[22] G. Béranger, J.C. Colson, F. Dabosi : Corrosion des matériaux à haute température, Les Editions de Physique, Les Ulis, France (1985).
[23] B. Pieraggi , Oxidation of Metals, 27 (1987) 177.
[24] D. Monceau, B. Pierragi ,Oxidation of Metals, 50 (1998) 477.
[25] C. Wagner, Journal of Electrochemical Society, 99 (1952) 369.
[26] T.B. Massalski, ASM Metals Park (1990).
[27] A. Bruckman and G.Simkovich, Corrosion Science,12 (1972) 596.
[28] C. Wagner, Journal of Electrochemical Society, 103 (1956) 609.
[29] L.Himmel, R.F Mehl and C.E Birschenall, Journal of Metals, 5 (1953) 827.

[30] M.H. Davies, M.T. Simmad, C.E Birschenall, Journal of Metals,191 (1951) 889.
[31] N.Birks and G.H. Meier, Edward Arnold Ltd, London, UK (1983).
[32] K. Heindlhofer and B.M. Laresen, Trans. Ameri. Sc. Steel. Treat., 21 865 (1933).
[33] G.C Fryburg, R. A. Miller, F.J Khol and C. A. Stearns, Journal of Electrochemical Society ,124 (1977) 1738.
[34] D. Caplan and M.Cohen, Journal of Electrochemical Society, 108 (1961) 438.
[35] A.C.S. Sabioni, A.M. Huntz, J. Philibert, B. Lesage and C. Monty, Journal of Materials Science, 27 (1992) 4782.
[36] D. Caplan and G.I. Sproule, Oxidation of Metals, 9 (1975) 459.
[37] M. Skeldon, J. M. Calvert, D.G lees, Oxidation of Metals,28 (1987) 109.
[38] A.M. Huntz and S.C. Tsai, Journal of Materials Science letters ,13 (1994) 821.
[39] W. J. Quadakkers, J. Piron-Abellan, V. Shemet, L. Singheiser, Materials at High Temperatures, 20 (2003) 115.
[40] J. E. Hammer, S. J. Laney, R. W. Jackson, K. Coyne, F. S. Petit, G. H. Meier, Oxidation of Metals, 67 (2007) 1.
[41] I.Saeki, H. Konno and R. Furuichi, Corrosion Science, 38 (1996) 19.
[42] Z. Yang, K. S. Weil, D. M. Paxton, J. W. Stevenson, Journal of the Electrochemical Society, 150 (2003) 1188.
[43] G. Cabouro, G. Caboche, S. Chevalier, P. Piccardo, Journal of Power sources, 156 (2006) 39.
[44] W. J. Quadakkers, J. Piron-Abellan, V. Shemet, Materials Research, 7 (2004) 203.
[45] S. Chevalier, G. Bonnet, K. Przybylski, J. C. Colson, J. P. Larpin, Oxidation of metals,54 (2000) 527.
[46] P. Piccardo, S. Chevalier, R. Molins, M. Viviani, G. Caboche, A. Barbucci, M. Sennour, R. Amendola, Surface and Coatings Technology, 201 (2006), 4471.
[47] K. Huang, P. Y. Hou, J. B. Goodenough, Solid State Ionics,129 (2000) 237.
[48] T. Brylewski, M. Nanko, T. Maruyama, K. Przybylski, Solid State Ionics,143 (2001) 131.
[49] H. Kurokawa, K. Kawamura, T. Maruyama, Solid State Ionics 168 (2004) 13.
[50] T. Fichpedersen, P. B. Friehling, J. B. Bidde-Sorensen, S. Linderoth, Journal of Corrosion Science and Engineering, 6 (2003) 1.
[51] P. Huczkowski, N. Christiansen, V. Shemet, J. Piron-Abellan, L. Singheiser, W. J. Quadakkers, Materials and Corrosion, 55 (2004) 825.
[52] P. Y. Hou, K. Huang, W. T. Bukker, in S. C. Singhal, M. Dokiya (Eds.), Solid Oxide Fuel Cells VI. Electrochemistry Society Proceedings 99-19, The electrochemical Society, Pennington, New York, 748.
[53] K. Huang, P. Y. Hou, J. B. Goodenough, Materials Research Bulletin, 36 (2001) 81.
[54] S. Chandra-Ambhorn, Y. Wouters, L. Antoni, F. Toscan, A. Galerie, Journal of power sources, 171 (2007) 688.
[55] L. Cooper, S. Benhaddad, A. Wood, D. G. Ivey, Journal of power sources, 184 (2008) 220.
[56] T. Horita, Y. Xiong, K. Yamaji, H. Kishimoto, N. Sakai, M. E. Brito, H. Yokokawa, Solid State Ionics, 174 (2004) 41.
[57] S. Chevalier, G. Bonnet, G. Borchardt, J.C. Colson, J.P. Larpin, Materials Science Forum, 372 (2001) 327.
[58] P. Skeldon, J. M. Calvert, D. G. Lees, Phylosophical Transactions of the Royal Society A, 296 (1980) 567.
[59] M. J. Graham, D. F. Mitchell, Materials Science Forum, 43 (1989) 207.
[60] C. M. Cotell, G. J. Yurek, R. J. Hussey, D. F. Mitchell, M. J. Graham, Oxidation of Metals, 34 (1990) 173.

[61] C. M. Cotell, G. J. Yurek, R. J. Hussey, D. F. Mitchell, M. J. Graham, Oxidation of metal, 34 (1990) 201.
[62] M. F. Stroosnijder, J. D. Sunderkötter, M. J. Cristobal, H. Jenett, K. Isenbügel, M. A. Baker, Surface and coating technology, 83 (1996) 205.
[63] S. Chevalier, C. Valot, G. Bonnet, J. C. Colson, J. P. Larpin, Material Science and Engineering A, 343 (2003) 257.
[64] H. J. Grabke, Surface and Interface Analysis , 30 (2000) 112.
[65] I. G. Wright, Metal handbook, Corrosion 9th edition, ASM Metals Park, OH (1987).
[66]J. Piron Abellan, T. Olszewski, G. H. Meier, L. Singheiser, W. J Quadakkers, International Journal of Materials Research 101 (2010) 2
[67] M. Schütze , D. Renusch, M. Schorr, Corrosion Engineering, Science and Technology, 39(2004) 157.
[68] J.P.T.Vossen, P. Gawenda, K. Rahts , M. Röhrig , M. Schorr, M. Schütze, Materials at High Temperatures, 14 (1997) 387.
[69] H.J. Grabke, E.M. Müller-Lorenz, B. Eltester, M. Lucas, D. Monceau, Steel Research International, 68 (1997) 179.
[70] H.J Grabke, Z.Tökei, C. Ostwald, Steel Research International, 75 (2004) 38.
[71] C. Ostwald , H.J Grabke, Corrosion Science, 46 (2004) 1113.
[72] S. Jianian, Z. LongJiang and L. Tiefan, Oxidation of Metals, 28 (1997) 449.
[73] N.Otsuka, Y. Shida and H. Fujikawa, Oxidation of Metals 32 (1989) 13.
[74] N.J. Corry and T.M. Herrington, Oxidation of Metals 28 (1987) 238.
[75] M. Schütze, M. Schorr, D. Renusch, A. Donchev, J.P.T. Vossen, Materials Research, **7** (2004) 111.
[76] H.E. Evans, A.T. Donaldson and T. C. Gilmour, Oxidation of Metals, 52 (1999).
[77] F. J. Perez and S. I. Castaneda, Surface and Coatings Technology, 201 (2007) 6239.
[78] J. Ehlers, D. J. Young, E. J. Smaardijk, A. K. Tyagi, H. J. Penkalla, L. Singheiser and W. J. Quadakkers, Corrosion Science, 48 (2006) 3428.
[79] F. Pérez-Trujillo and S. Castañeda, Oxidation of Metals, 66 (2006) 231.
[80] J. E. T. F. Liu, T. Jonsson, S. Canovic, K. Segerdahl, J. -E. Svensson, M. Halvarsson, Oxidation of Metals ,66 (2006) 295.
[81] H. Nickel, Y. Wouters, M. Thiele and W. J. Quadakkers, Fresenius' Journal of Analytical Chemistry, 361 (1998) 540.
[82] J. Zurek, E. Wessel, L. Niewolak, F. Schmitz, T. U. Kern, L. Singheiser and W. J. Quadakkers, Corrosion Science 46 (2004) 2301.
[83] S. Henry, PhD thesis, Institut Nationnal Polytechnique de Grenoble, Grenoble, France, 2000.
[84] N. Agmon, Chemical Physics Letters, 244 (1995) 456-462.
[85] S. Ricote, G. Caboche, O. Heintz, Journal of Applied Electrochemistry, 39 (2009) 553.
[86] G. Hultquist, B. Tveten, Erik Hörnlund, Oxidation of Metals, 54 (2000) 1.
[87] Y. Larring, R. Haugsrud, T. Norby, Jounral of Electrochemical Society B, 150 (2003) 374.
[88] D. Laverde, T. Gomez-Acebo and F. Castro, Corrosion Science, 46 (2004) 613.
[89] J. Jianmin, M. Montgomery, O. H. Larsen and S. A. Jensen, Materials and Corrosion, 56 (2005) 549.
[90] V. Lepingle, G. Louis, D. Allue, B. Lefebvre and B. Vandenberghe, Corrosion Science, 50 (2008) 1011
[91] W.J. Quadakkers, P.J. Ennis, J. Zurek and M. Michalik, Materials at High Temperatures, 22 (2005) 47.
[92] A. Rahmel et J. Tobolski, Corrosion Science 5 (1965) 333.

[93] J. Ehlers, D. J. Young, E. J. Smaardijk, A. K. Tyagi, H. J. Penkalla, L. Singheiser and W. J. Quadakkers, Corrosion Science, 48 (2006) 3428.
[94] Y. Ikeda and K. Nii, Transaction of the Japanese Institute of Metals, 26 (1984) 52.
[95] W. J. Quadakkers, J. F. Norton, H. J. Penkall, U. Breuer, A. Gil, T. Rieck, M. Hänsel in S. B. Newcomb, J. A. Little (Eds.) 3rd International conference of Microscopy of Oxidation Cambridge, 16-18 Septembre 1996, Proceedings, The institute of Materials (1996) 221.
[96] Y. P. Jacob, V. A. C. Haanappel, M. F. Stroosnijder, H. Buscail, P. Fielitz, G. Borchardt, Corrosion Science, 44 (2002) 2027.
[97] S. Osgerby, J. P. Banks, L.J. Brown, Materials and Corrosion, 57 (2006) 165.
[98] R. Viswanathan, R. Purget, U. Rao, Proceedings of the 7th Liege Conference on Materials for Advanced Power Engineering, Energy Technology, 21, Part I-III (2002) 1109.
[99] G. Smith, L. Shoemaker, Advanced Materials and Processes, July (2004) 23.
[100] S.C. Cha, H.W. Gudenau, G.T. Bayer, Materials and corrosion, 53 (2002) 195.
[101] L. Pawlowski, The science and engineering of thermal spray coatings, John Wiley & Sons, ISBN 0-471-95253-2, (1995)
[102] J.C Nava-Paz, A.L. Plumley, O.K Chow, W. Chen, Materials at High Temperatures, 13 (2002) 127.
[103] A. Agüero, R. Muelas, Materials Science Forum, 461 (2004) 957..
[104] A. Agüero, Garcia de Blas, R. Muelas, A.Sanchez, S. Tsipas, Materials Science Forum, 369 (2001) 939.
[105] A. Agüero, R. Muelas, M. Gutierrez, R. Van Vulpen, S. Osgerby, J.P. Banks, Surface and Coatings Technology, 201(2007) 6253.
[106] B.A. Pint, Y. Zhang, P.F. Tortorelli, J.A. Haynes, I.G. Wright, Materials at High Temperatures, 18 (2001) 185.
[107] K. L. Choy, Progress in Materials Science, 48 (2003) 57.
[108] R. Mevrel, C. Duret, R. Pichoir, Material Science and Technology, 2 (1986) 201.
[109] P.A. Choquet, E.R. Naylor, R.A Rapp, Materials science and engineering A, 121 (1989) 413
[110] W. Da Costa, B. Gleeson, D.J. Young, Journal of Electrochemical Society, 6 (1994) 1471.
[111] W. Da Costa, B. Gleeson, D.J. Young, Journal of Electrochemical Society, 10 (1994) 2690.
[112] W. Da Costa, B. Gleeson, D.J. Young, Surface and Coatings Technology, 88 (1996) 165.
[113] F.D. Geib, R.A. Rapp, Oxidation of Metals, 40 (1993) 213.
[114] B. Gleeson, W.H. Cheung., W. Da Costa, D.J. Young, Proceeding For the "8th Asian-Pacific Corrosion control Conference", Bangkok (1993) 43
[115] U.R. Kattner, T.B Massalski., Binary Alloy Phase Diagrams, H. Baker edition (1990), ASM International, p.147.
[116] C. Houngninou , S. Chevalier and J.P. Larpin Applied Surface Science, 236 (2004) 256.
[117] R. Prescott, M. J. Graham,Oxidation of Metals, 38 (1992) 233.
[118] R. Prescott, M. J. Graham, Oxidation of Metals,38 (1992) 73.
[119] M.Sakiyama, P. Tomaszewicz, G. R. Wallwork, Oxidation of Metals, 13 (1979) 311.
[120] W.E. Boggs, Journal of the Electrochemichal Society, 6 (1971) 906.
[121] W.C. Hagel, Corrosion, 21 (1965) 316.
[122] P. Tomaszewicz, G.R. Wallwork, Oxidation of Metals, 23 (1983) 53.
[123] P. Tomaszewicz, G.R. Wallwork, Corrosion, 40 (1984)152.
[124] S.W. Banovic, J.N Dupont., A.R. Marder, Oxidation of Metals, 54 (2000) 339.
[125] R. Bianco, R.A. Rapp, Oxidation of Metals , 38 (1992) 33.
[126] R. Bianco, R.A. Rapp, Journal of the Electrochemichal Society, 4 (1993) 1181.

[127] R. Bianco, R.A. Rapp, J.L Smialek, Journal of the Electrochemichal Society, 4 (1993) 1191.
[128] C. Choux, PhD thesis, University of Bourgogne, Dijon, France (2008).
[129] W. Qu, Jian Li, D. G. Ivey, Journal of Power Sources, 138 (2004) 162.
[130] W. Qu, L. Jia, D. G. Ivey, J. M. Hill, Journal of Power Sources, 157 (2006) 335.
[131] Fontana, R. Amendola, S. Chevalier, P. Piccardo, G. Caboche, M. Viviani, R. Molins, M. Sennour : Journal of Power Sources 171 (2007) 652.
[132] G. Cabouro, DEA, University of Bourgogne, Dijon, France (2004).
[133] C. Choux, Master 2 Research, University of Bourgogne, Dijon , France (2005).
[134] G.J. Yurek, P. Przybylski, A.J. Garratt-Reed, Journal of electrochemistry Society, 134 (1987) 2643.
[135] K.Przybylski, Material Science Forum, 43 (1989) 1.
[136] B.A. Pint, Oxidation of Metals, 45 (1996) 335
[137] S. Sroda, D. Baxter and M. Arponen, Materials and Corrosion, 56 (2005) 791.
[138] T. Sundararajan, S. Kuroda, J. Kawakita, S. Seal, Surface and Coatings Technology, 201 (2006) 2124.
[139] T.N. Rhys-Jones, H.J. Grabke, H. Kudiela , Corrosion Science, 27 (1987) 49.
[140] I. M. Wolff, L. E. Iorio, T. Rumpf, P. V. T. Scheers and J. H. Potgieter, Materials Science and Engineering A, 241 (1998) 264.
[141] A. Martinez-Villafañe, J. G. Chacon-Nava, C. Gaona-Tiburcio, F. Almeraya-Calderon, R. Bautista-Margulis, J. G. Gonzalez-Rodríguez, Scripta Materialia, 46 (2002) 127.
[142] Y. S. Li, Y. Niu and M. Spiegel, Corrosion Science, 49 (2007) 1799.
[143] A. P. Greeff, C. W. Louw, J. J. Terblans and H. C. Swart, Corrosion Science, 42 (2000) 991.
[144] P. Y. Hou, Journal of Materials Science Letters, 19 (2000) 577.
[145] P. Y. Hou, Oxidation of Metals, 52 (1999) 337.
[146] H. J. Grabke, R. Möller, H. Erhart and S. S. Brenner, Surface and InterfaceAnalysis, 22 (1987) 202.
[147] F. Abe, Materials Science and Engineering A, 770 (2001) 319.
[148] A. Agüero, M. García, M. Gutiérrez, Materials and Corrosion , 56 (2005) 937.
[149] F. Armanet, J.H. Davidson, Resistance a la corrosion a haute temperature des aciers inoxydables et alliages refractaires. P. Lacombe, B. Baroux, G. Beranger (Eds.), Les aciers inoxydables, Les Editions de Physique, Paris, 1990, 49.
[150] V. Lepingle, G. Louis, D. Petelot, B. Lefebvre, B. Vandenberghe,Materials Science Forum, 461 (2004) 1039.
[151] N. Sämann, M. Spiegel, H.J. Grabke, Materials Science Forum, 369 (2001) 963.
[152] B.A. Pint, R. Peraldi, P.F. Tortorelli. NACE Paper 03-499, Houston, Texas, NACE Corrosion 2003, San Diego, CA, March 2003.
[153] Marasco, D.J. Young. Oxydation of Metals. 36 (1991) 157.
[154] I. Iordanova, K.S. Forcey, R. Harizanova, Y. Georgiev, M. Surtchev, Journal of Nuclear Materials 257 (1998) 126.
[155] Z. Yang, G.-G. Xia, X.-H. Li and J. W. Stevenson, International Journal of Hydrogen Energy 32 (2007) 3648.
[156] M.J. Garcia Vargas, L. Lelait, V. Kolarik, H. Fietzek, M. Juez-Lorenzo, Materials Science Forum 461 (2004) 823.
[157] B. A. Pint, R. Peraldi, P.J. Maziasz, Materials Science Forum, 461 (2004) 815.
[158] C. Collins, J. Lucas, T. L. Buchanan, M. Kopczyk, A. Kayani, P. E. Gannon, M. C. Deibert, R. J. Smith, D. S. Choi and V. I. Gorokhovsky, Surface and Coatings Technology, 201 (2006) 4467.

[159] F. Abe, M. Taneike and K. Sawada, International Journal of Pressure Vessels and Piping, 84 (2007) 3.
[160] J. Purmensky, V. Foldyna and Z. Kubon, Key Engineering Materials, 171 (2000) 419.
[161]A. Kozlowski, Techniques de l'Ingénieur. Influence des éléments d'alliage, Autres éléments d'addition, M 4570.
[162] K. Berreth, K. Maile, A. Lyutovich, Materials and Corrosion 56 (2005) 916.
[163] A. M. Huntz, V. Bague, G. Beauple, C. Haut, C. Severac, P. Lecour, X. Longaygue and F. Ropital, Applied Surface Science, 207 (2003) 255.
[164] J. M. Brossard, M. P. Hierro, J. A. Trilleros, M. C. Carpintero, L. Sanchez, F. J. Bolivar, F. J. Perez, Surface and Coatings Technology, 201 (2007) 5743.
[165] Z. D. Xiang, P. K. Datta, Acta Materialia, 54 (2006) 4453.
[166] Z. Xiang, S. Rose, P. Datta, Journal of Materials Science, 41 (2006) 7353.
[167] E. Huttunen-Saarivirta, F. H. Stott, V. Rohr and M. Schütze, Corrosion Science,49 (2007) 2844.
[168] Y.-Y. Chang, C.-C. Tsaur and J. C. Rock, Surface and Coatings Technology ,200 (2006) 6588.
[169] E. N'Dah, S. Tsipas, F. Bolívar, M. Hierro and F. Pérez, Oxidation of Metals,69 (2008) 77.
[170] Y.S. Li, M. Spiegela, S. Shimada, Materials letters, 58 (2004) 3787.

II. Experimental Techniques.

In this chapter an overview of the experimental techniques and characterization tools used during this study will be .presented. The complementarity and originality of certain of those techniques will allow us in the following chapters to draw conclusions of the steps of germination and growth of the oxide layer on 9%Cr steels in dry and wet high temperature environments.

II.1 Materials and sample preparation.

9 % chromium steel provided by OCAS ArcelorMittal R&D Global, Gent was the substrate used for this work. The grade composition is given in table II.1 below.

Elts	C	Cr	Mo	Si	Mn	B	P	Ni	S	Nb	Al	V	N	Fe
9% Cr Alloy% Wt	**0.098**	**8.4**	**1.1**	**0.34**	**0.57**	**0.0004**	**0.01**	**0.25**	**0.002**	**0.076**	**0.017**	**0.27**	**0.028**	Bal

Table II.1: chemical composition of the 9% chromium containing steel used for the study.

The casting was laminated by hot rolling at 950°C. The plate was then normalized at 1100°C for 30 min followed and air cooled to room temperature. The final crystallographic structure was obtained after tempering at 800°C for 1h.

Samples were shaped to the dimensions of 15 x 10 x 2 mm coupons, with or without a 2 mm diameter hole in order to hang them for the isothermal oxidation test. Prior to any further experimental step, each specimen is polished up to 1200 µm with SiC papers and cleaned in an ultrasonic ethanol bath.

II.2 High temperature oxidation tests.

II.2.1 Isothermal tests in dry air.

The kinetics of oxidation of samples was followed using a SETARAM TG 92 thermobalance. Experiments were performed between 600°C and 750°C for 100 hours or 200 hours in laboratory air under atmospheric pressure. This thermobalance has a balance beam ruled by a computer and allow to measure mass variation with microgram accuracy. The evolution of mass is a function of time ($\Delta m/A) = k_p t$ where Δm: masse gain in g, A: area in cm^2 and t: time in second) and allow in certain cases to determine the rate parabolic constant k_p [1].

II.2.2 Isothermal tests in air enriched with 12% Vol. of water vapour.

The experimental setup used to achieve the aging processes in water vapour is exposed in Figure II.1. The device, which was developed during the PhD study of Celine Choux [2], consists of a circular furnace where the temperature of oxidation could reach 1000 ° C and three water vapour sources, each of them materialized by a balloon and a cooling column.

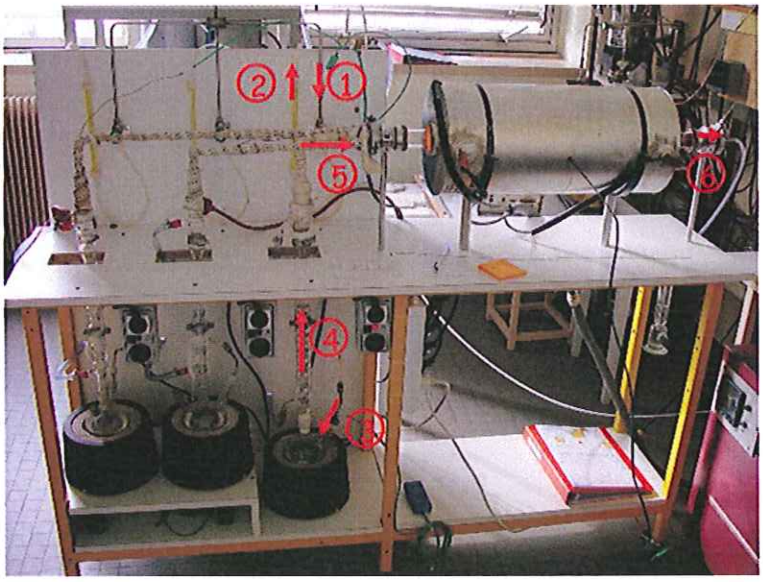

Figure II.1: Experimental disposal for isothermal tests in air enriched with 12% Vol. of water vapour

The specimens are introduced in a quartz tube within the furnace. For the aging processes in water vapour, a balloon is filled with distilled water and then brought up to temperature (90 ° C-100 ° C). Industrial air is led to the balloon into the boiling water (3), and it brings the water vapour into the hot furnace (4 and 5). The arrows (from 1 to 6) in Figure II.1 materialized the gas flow into the disposal. The air rate flow entering in the balloon is 70 ml/ min (5L/h). The water temperature in the condenser is set at 40°C and regulated by a thermostatic bath. These conditions form an atmosphere enriched with 12% Vol. of water vapour [3]. The other balloons are used for isotopic labeling experiment with D_2O and $H_2{}^{18}O$. The samples are weighted, with and without their crucible, before and after the oxidation tests in order to calculated their gross and net mass gain. At least ten samples could be tested at one time with this device.

II.2.3 Oxidation tests in cyclic condition.

Heat exchangers or boilers quite often work in cyclic condition. As previously mentioned in paragraph I.2.8 the temperature cycles could generate important stress in the material and its oxide which could have a catalytic effect on the lost of oxidation resistance. To further improve our understanding of such phenomenon, an automatic high temperature cyclic test block was developed during this work. Figure II.2 is a picture of the experimental device.

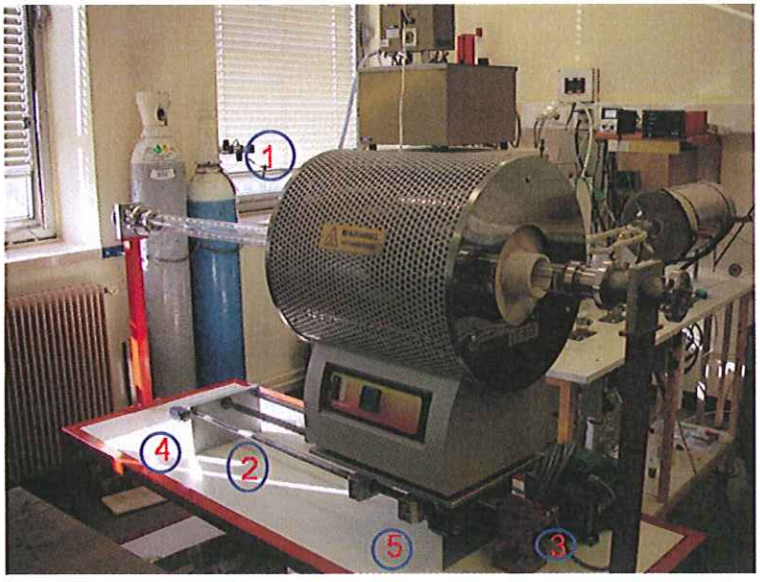

Figure II.2: Experimental device for high temperature cyclic tests.

The samples are placed into the furnace via a quartz tube (1). The furnace mobility on the trail (2) is ensured by an engine (3) which is controlled by two temporization devices (4-5). The

temporization allows for cycles of 1 hour each. One cycle being composed of 45 min at high temperature (650°C) and 15 min at (300°C). The samples are then brought down to room temperature each 24 hours for mass gross and net measurement. The device allows carry out cycle tests on around 9 samples at the same time.

Moreover, a very few works such [4, 5] deal with the effect of water vapour in cyclic condition on 9% Cr steel. Thus, the water vapour generator described in the previous paragraph was adapted on the cyclic test block and used to perform a set of cycle experiments in air enriched with 12% Vol. of water vapour at 650°C.

II.2.4 Long term oxidation

If isothermal tests of 100 hours using thermobalance give a good idea of oxidation kinetic for 9%Cr steel and allow to determine the parabolic rate constant; it remains necessary, for thermal plant application, to have an accurate idea of the steel behaviour for long time exposure in laboratory air at 650°C and 700°C using a CWF 1300 Carbolite muffle furnace. The discontinuous mass gain reported by this method, and the samples characterization give information on the oxide scales evolution in time.

II.3 Characterization of the oxide scale

An important part of this work was dedicated to the understanding of the first steps of oxidation of the materials which could help to prevent dramatic behaviour at high temperature. Therefore, several characterization tools, some of them original and other more conventional, were mobilized to bring elements of comprehension of the oxide growth mechanisms and the layers composition.

II.3.1 Scanning Electron Microscopy (SEM)

Oxidized samples surfaces analyses, and chemicals characterizations were performed using a JEOL JSM-6400 F scanning electron microscope (SEM) with a field emission gun (FEG), coupled with an Oxford LINK EXLII energy dispersive X-ray (EDX) analyzer.
Cross sections observations were also realized using a particular embedding technique [6]. Copper was pulverized on the sample surface thank to a Gatan 681 (6 keV Ar^+ ions beam,

Intensity = 100 μA, incidence 35°). Then a copper electrochemical deposition was done in two steps using a $CuSO_4$ solutions. The first step consists in the formation of a thin, adherent and covering coating (30 min, 20 mA.cm^2). The second step (3h, 35 mA.cm^2) is necessary to form a 100 to 150 μm thick coating which will protect the oxide layer during the subsequent polishing process. This technique allows the observation of the whole oxide layer thickness and the realization of semi quantitative chemical profiles.

II.3.2 X-Ray Diffraction (XRD) at low glancing angle

Different crystallites are present in the corrosion products. In order to identify those phases, patterns was taken by X-ray diffraction (XRD) using a CPS 120 INEL apparatus with a copper anticathode (Kα=0.154 nm) using to 1° glancing angles. The analyses at low glancing angles give information on the upper surface of the oxidized samples.

II.3.3 Micro Raman spectroscopy

Julie Mougin [7] and Sandrine Henry [8] showed in their PhD theses that Raman Spectroscopy could be a useful technique for characterizing oxide thermally grown on alloys. Thus, Raman surface and cross section analyses were performed in this work using a Jobin-Yvon T64000 spectrometer.

A nitrogen-cooled CCD was used as detector. The excitation was provided by an Ar–Kr ion laser and the spectra were recorded in a back-scattering configuration. The wavelength was 514nm and the excitation power was kept low enough to avoid heating of the samples as recommended by Aude Brevet in her work [9].

II.3.4 Photoelectrochemistry (PEC)

Yves Wouters and Alain Galerie [10-13] from the "Grenoble Intitut National Polytechnique" developed an original spectroscopy tool which allows the characterization of oxides by using their semi-conductivity properties. In the chromia case, they have highlighted two semiconductor phases signed by their respective bandgaps (3.0 and 3.5 eV) with variations of semiconduction types (n, p and insulator, more or less doped). The

protective character of the scale was clearly demonstrated when the highest bandgap phase (3.5 eV) identified as the external subscale, was close to an insulator [13]. Moreover, chromia is generally considered as p type semiconductor in the atmospheric pressure range and change to a n type semiconductor at very low oxygen pressure [11]. Macroscopic PEC measurements were obtained by illuminating the whole surface (area: 0.785 cm^2) of the samples oxidized in laboratory air which were used as working electrodes in a classical three-electrodes electrochemical cell. The measurement cell on Figure II.3 is equipped with a flat quartz optical window, using a platinum foil (area = 1 cm^2) as the counter electrode and a Hg/Hg_2SO_4 mercury sulphate electrode (MSE) as the reference electrode (+0.650 V/ENH).

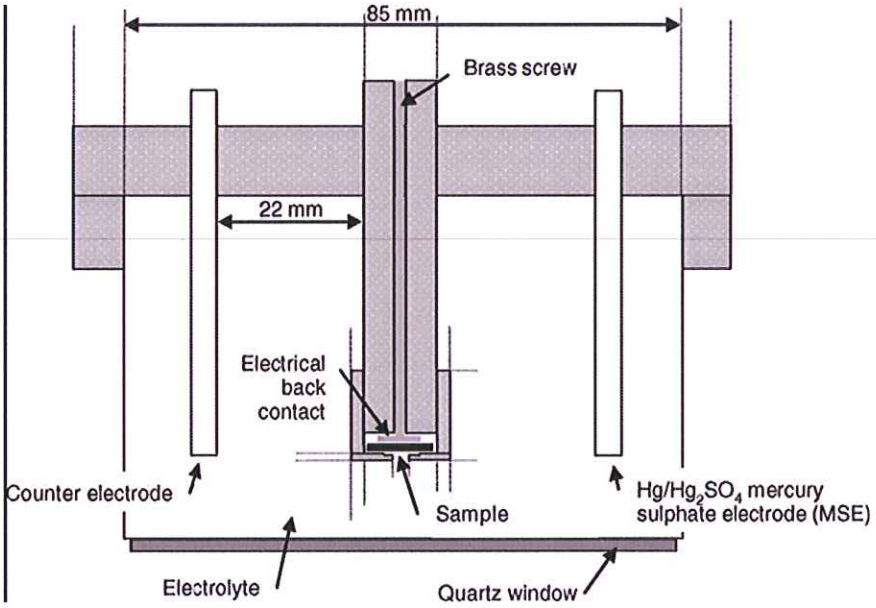

Figure II.3: schematic of the electrochemical measuring cell [10]

Electrical back contact was taken directly on the Fe9Cr metal after removing the oxidation layer. The electrochemical cell was controlled by means of a Voltalab 32 potentiostat (Radiometer Analytical) driven by a homemade software. Photocurrent vs. energy curves were measured under modulated light conditions, using a lock-in amplifier (PAR 5208, EG&G Instruments) together with a mechanical light chopper (PAR 197, EG&G Instruments, f = 21 Hz), at variable wavelength using a 1000 W Xenon arc bulb (Müller GmbHLax 1000) and a triple grating monochromator (PAR 1235, EG& G Instruments) allowing to select the photon wavelengths with a spectral width of ±1 nm. To extract the quantum yield from the as-measured photocurrent values, a calibrated silicon photodiode (Hamamatsu S-1722) was used to measure the photon flux as a function of wavelength. For this purpose, the silicon photodiode replaced the sample in identical position after removing

part of the electrolyte from the cell until the sample surface was grazing the surface of the electrolyte. This minimised the unavoidable uncertainties in the determination of the relative photon flux (and quantum yield) at each wavelength, as could be verified by comparing the transmission curves of colored solutions measured by means of either the photodiode or an UV–Visible spectrometer. In this study, quantum yield will be named photocurrent (I_phot). All experiments were performed in an aqueous solution of sodium sulfate desaerated (0.1 M) at pH 8.0 $\pm$ 0.1.

II.3.5 Ex situ and In-situ X-ray Photoelectron Spectrocopy (XPS)

Within the purpose to clearly understand the corrosion reaction on the 9% Cr substrate, XPS spectra profiles were also registered using 241W Al kα radiation (1486.6 eV) on a PHY Quantera SXM. Information within the scale depth was obtained by successive Argon ion sputtering (3 keV, 15nA) and analyses from the oxide surface scale to the bulk of sample oxidized at 600°C for 100 h in air and at atmospheric pressure in a muffle furnace. The analyses being performed on post-mortem sample oxidized outside the characterization disposal will be called Ex-situ XPS analyses by opposition to what is obtained using the device developed by Olivier Heintz [14] at the laboratory "Intersdisplinaire Carnot de Bourgogne".

This equipment elaborated for heat treatment under controlled atmosphere enables the step by step study of the reactivity of materials under high temperature and high pressure once coupled with X-ray Photoelectron Spectrometer (Figure II.4) .

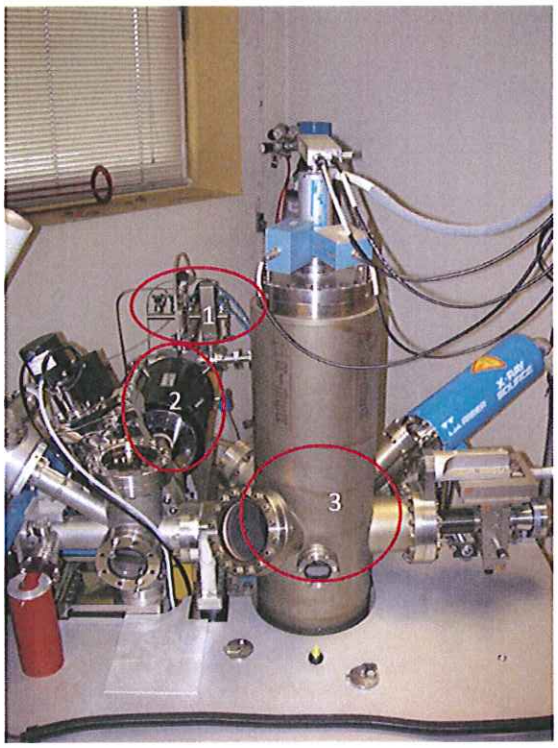

Figure II.4: Experimental equipment for in-situ XPS experiment.

The samples were placed in a quartz tube inserted in a tubular oven (2). The unit was maintained under vacuum prior and after the oxidation process (7.10^{-5} Pa, using a turbomolecular pumping unit). The oxidized metallic coupon, cooled to room temperature, was then transferred into the analysis chamber (3) of a SIA 100 Cameca-Riber spectrometer (Resolution of 1.2 eV full, width at half maximum of $3d_{5/2}$ level of silver) without contamination from outside atmosphere. In order to focus on the first steps of the oxide growth, the samples oxidation conditions were the following: 5 min, 30 min and 1 hour exposure at 600°C in laboratory air under atmospheric pressure (1 is the gas inlet part of the device); and 5 min, 30 min and 1 hour exposure at 600°C in steam with a pressure close to 2.10^{-2} bar. Spectra were then recorded using 240W Al Kα radiation (1486.6 eV). Emerging photoelectrons were detected perpendicularly to the surface. Photoemission peak areas were calculated after background substraction using a Shirley routine. Energy calibration has been achieved on level 1s of adventitious carbon (at 284.5 eV). Argon ion bombardments were carried out using a Perkin-Elmer 04-303A differentially pumped ion gun. Bombarding conditions were an acceleration voltage of 4keV, a pressure of 10^{-5} Pa and an angle of incidence with respect to the surface normal equal to 60°. The ion flux was in the region of $5x10^{16}$ ions $cm^{-2}.s^{-1}$.

The spectrum of industrial hematite and chromia powder commercialized by the Prolabo Sanofi-aventis laboratory (Rhône-Poulenc) and were registered prior to this work as a help for

the interpretation of the spectrum reconstruction. The Casa software package was used for data treatments including background subtraction with a Shirley routine and quantifications using relative sensitivity factors given in the package.

Moreover a heat treatment at 650°C for 100h was performed using this specific device with a D_2O source as steam generator. The objective was to highlight after a SIMS analysis the effect of the proton on the oxidation mechanism.

II.3.6 Transmission Electron Microscopy (TEM)

This technique allows having information on the oxide scale at the nanometric scale. The investigation of thin films, using TEM microscope, requires significant preparations which are usually time consuming [15]. For this work thin foils were prepared at OCAS ArcelorMittal Global R&D, Ghent using the Focus Ion Beam (FIB) method. Indeed Micro-analytical tool combines high resolution imaging (electron and ion images) with specific sample preparation techniques (etching or milling) on a nanoscale. The FIB allows at least the realization of two thin cross sections per day. The preparation steps for the so called "lift out" method are the followings:

- A working zone is selected by doing micrographs of the oxidized samples top surface using the FEG-SEM head of the FIB. The chosen area is protected by a Pt and C coating. Then started the milling process into the samples from the top surface to the metal/oxide interface with the Ga^+ ion focus beam of the equipment. A needle is then used to take out (lift out) cautiously the cross section from the sample surface and to weld it to a copper grid. At this moment, a thinning step begins where materials are removed by several pulverizations with the Ga^+ ion beam; until reaching a thickness which allows working with the TEM (< 70 nm). A cleanning step with Ar^+ beam is then performed to suppress pollution generated by the Ga^+ pulverization.

The thin foils on the copper grid were investigated with a TEM JEOL JEM 2100 LaB_6 (accelerating voltage =200 kV, point resolution 0.25 nm, network resolution 0.14 nm) coupled with JEOL JED 2300T energy dispersive X-ray analyzer.

II.3.7 In-situ diffraction analyses at the European Synchrotron Radiation Facility.

The European Synchrotron Radiation Facility (ESRF) in Grenoble is the most powerful synchrotron radiation source in Europe. A proposal for performing in-situ diffraction experiments at low angles in order to follow step by step the growth of the crystallite structure on the oxidized samples was accepted. The main idea behind those analyses was to clearly obtain the sequence of oxide scale formation from the germination to the "breakaway". Therefore the ID31 high resolution powder diffraction beamline was chosen for performing this experiment. The six-circle diffractometer was equipped with a furnace covered by a 0.5 mm thickness quartz dome (Figure II.5). A turbo pump was used to achieve a secondary vacuum inside the furnace. The samples were glued using their sides with an alumino silicate mixture, on the nickel heat resistance of the furnace which could reach 1000°C.

A wavelength of 0.4 Å (corresponding to an energy of 31 keV) was used during these experiments. The beam was size 1mm (horizontal) X 200 μm (vertical). The incidence angle was chosen to be equal to 1° in order to have information on the sample top surface. The depth of the analyzed zone was therefore 3μm. A region of 2x10 mm^2 at the sample surface was investigated in this way. Nine detectors collectively measure the diffracted intensity as a function of 2θ. Patterns from 2θ= 4° to 2θ=35° were registered with a 0.001° scanning step

When starting the experiment, 200 mbar of oxygen was injected in the furnace. A reference scan was registered at room temperature. The sample was brought to 750°C with a 10°C/min heating rate. Once at the dwell temperature, patterns were registered every 24 min during 60 hours. Data analaysis was performed using TOPAS©4.2 programme. The background line was fitted with a linear function while for the peak shape a Pearson VII function was used. The 2θ position of each peak were determined as a function of time.

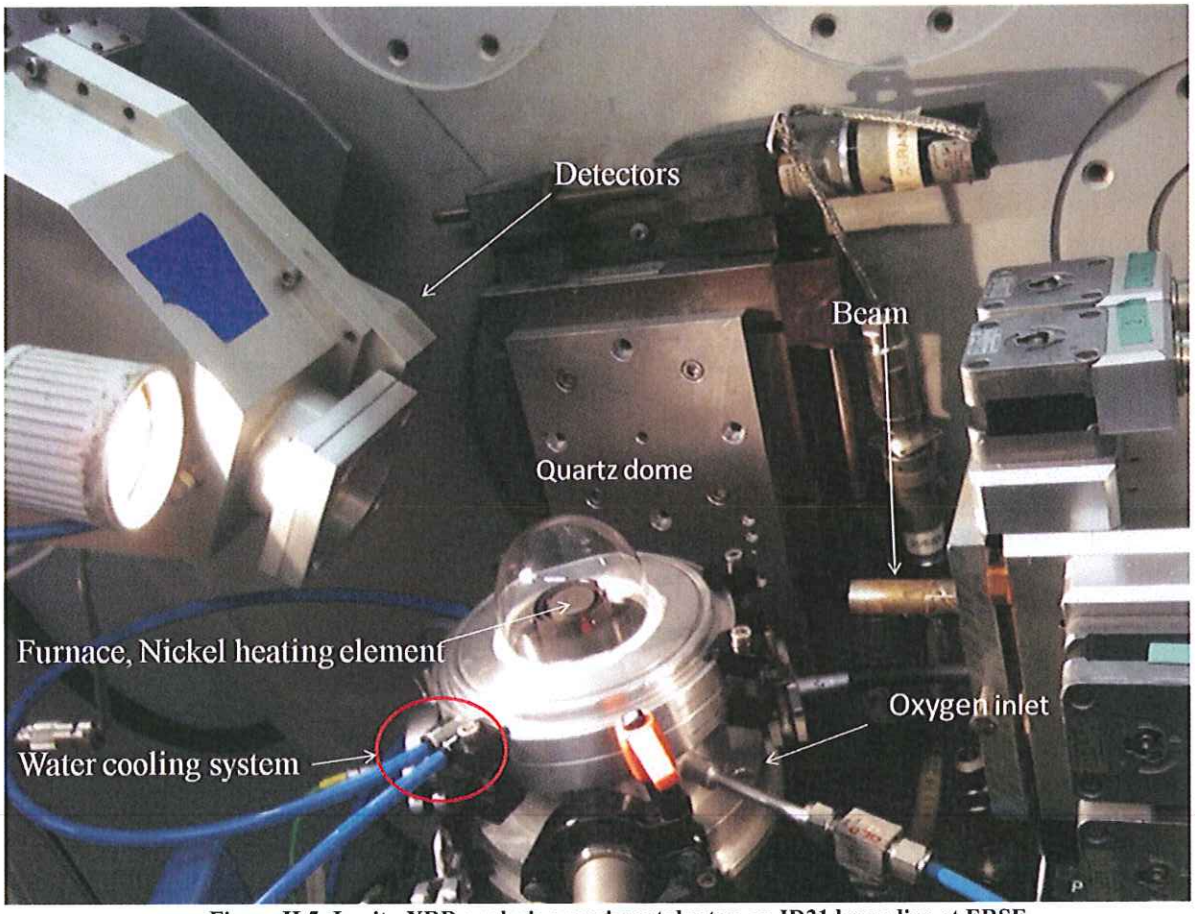

Figure II.5: In-situ XRD analysis experimental setup on ID31 beam line at ERSF

II.3.8 Secondary Ions Mass Spectroscopy (SIMS)

To better grasp the diffusion phenomenon during the oxidation reaction, and the effect of water vapour, Secondary Ions Mass Spectroscopy (SIMS) was performed on samples after isotopic labeling ageing tests. This type of spectroscopy analyzes mass and charge of the secondary ions produced by ion sputtering of the sample surface. The primary source consists of an inert argon ion (Ar +) beam (energy = 10 keV, intensity = 50 nA) with an incident angle of 45 °. The composition profiles were made with a spectrometer Cameca Riber. The area of analysis is approximately 250 µm x 250 µm. The SIMS results must be cautiously interpreted. Indeed, the SIMS signal, measured in counts per second, depends on element concentration but also other factors (ionization rate, target density, chemical surrounding...). It is therefore impossible to have a quantitative aspect of the detected items. The depth of craters, according to the time of abrasion was determined with a profilometer.

II.4 Diffusion process and oxidation mechanisms.

The growth of an oxide layer involves cationic and or anionic ions diffusion. A very interesting method to determine the oxide scale formation mechanism is the realization of two successive isothermal oxidations tests with oxygen isotopes. Therefore, isotopic labeling experiment was performed on 9% Cr steel at 650°C. The conditions were set according to the kinetic curve obtained during isothermal oxidation in air. The total marking time was determined to reach at the end of the experiment, the steady state observed on the kinetic curves corresponding to oxidation in laboratory air. The time marking in $^{16}O_2$ and $^{18}O_2$ are calculated to grow similar thickness of oxide in the two atmospheres. Figure II.6 is a picture of the experimental apparatus used for the isotopic experiments and developed by Aurelien Perron [16] during for the European project IDEAL CELL.

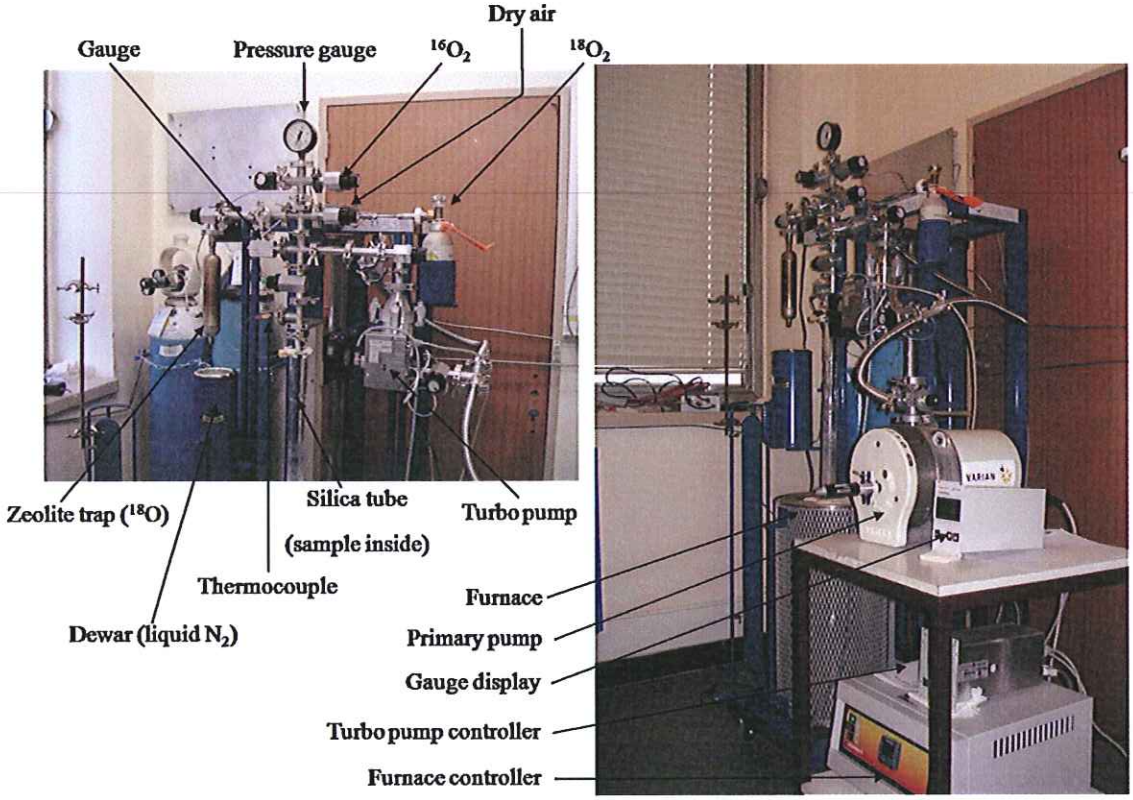

Figure II.6 : Isotopic exchange devices for reactivity study

A sample is placed under vacuum for several hours to reach around 9.10^{-4} mbar. $^{16}O_2$ is then introduced into the chamber under a pressure of 200 mbar. Once the oven reaches 650° C the heating zone is brought to the sample Level and the experiment marking begins. When the marking is completed in $^{16}O_2$, the vacuum is again obtained in the chamber to 10^{-3} mbar. The sample maintained at temperature to avoid thermal shock. At the correct vacuum (5 minutes later), 200 mbar of $^{18}O_2$ is introduced in the test chamber. At the end of the experiment, the

$^{18}O_2$ is trapped (due to its price) in 13X Zeolite cooled by liquid nitrogen. After isotopic labeling experiments, monitoring of isotope's chemical profiles by SIMS leads to understand the mechanisms of oxidation.

II.5 Metal Organic Chemical Vapour Deposition (MOCVD)

The positive effects of reactive elements and the thin film formed by MOCVD at high temperature were discussed earlier in the previous chapter (paragraphs I.10.3 and I.11). The literature insists on the positive effects of lanthanides and yttrium as reactive elements [17]. So during this experimental study, lanthanum oxide (La_2O_3), yttrium oxide (Y_2O_3) and neodymium oxide (Nd_2O_3) thin films deposited on 9% chromium content steel by MOCVD. The experimental device was built by Sebastien Chevalier during his PhD studies and the deposition method was clearly described in several papers [18-20]. Around 200 nm thick nanostructured coatings could be obtained by this chemical vapour technique; using metalo-organical precursors synthesized following a procedure proposed by Eisentrant[21]. Those precursors are β-diketonates: $La(thmd)_3$, $Nd(thmd)_3$ and $Y(thmd)_3$ (where thmd is tétra-méthyl-heptane-dionato $(CH_3)_3COCHCOC(CH_3)_3$). The coatings deposition conditions are listed in Table II.2.

	La_2O_3	Y_2O_3	Nd_2O_3
Precursor Mass (g)	0.3	0.3	0.3
Substrate Temperature (°C)	600	600	600
Precursor Temperature (°C)	200	215	215
Coating time (min)	25	25	25
O_2 flow (l/h)	2.5	2.5	2.5
N_2 flow (l/h)	7.5	7.5	7.5

Table II.2 : Coatings conditions function of the precursors [18, 22-23].

A Setaram γ-21A microbalance with an important sensibility (10^{-6}g) was used for calculating mass gain during the deposition process. In agreement with approximations according to which the film covers totally and homogeneously the surface, an accurate idea of the film thickness could be obtained using the following equation:

$$e = \frac{\Delta m}{A * \rho} \quad \text{Eq.II.1}$$

Where:

e: film thickness

Δm: mass of oxide coating on the substrate

A: substrate total Area

ρ : oxide apparent density ($g.cm^{-3}$) ($\rho_{La_2O_3}$=6.50, $\rho_{Y_2O_3}$=5.01, $\rho_{N_2O_3}$=7.24)

II.6 Aluminide Pack cementation coating

The aluminide pack cementation coating method is also a chemical vapour deposition process. The samples are introduced in an alumina crucibles containing a powder mixture composed of 82% weight of alumina (activated,-325mesh, 92% purity), 15 % wt. of aluminum (approx. 99% purity, particle size: 100 µm) and 3 % wt. of NH_4Cl. This pack composition was proposed in different papers [24-26]. Each of these powders has a defined role: The Aluminum is element to be deposited on the surface of the substrate. The NH_4Cl is the heat activator which intervenes in the aluminum diffusion through the pack by forming gaseous aluminum halides species. The alumina is the inert agent which prevent the pack mixture from sintering at high temperature. The crucibles are placed under an argon gas streaming for 15 hours. The samples are then subjected to heat treatment: 5 hours at 1000°C within the same inert atmosphere during the heating and cooling down process. The temperature ramp is about 10°C / min. The coated samples are then cleaned in an ethanol sonicated bath prior to any further experiment. Cross section SEM micrographs coupled with EDX profiles gave an idea of the obtained coating composition and thickness.

II.7 Casting preparation using a levitation melter

Certain elements are well known for their intrinsic good resistance behaviour at high temperature (Cr, Al, Si etc…). The modification of the 9% steel composition by adding or removing some alloying elements could lead to a significant improvement in the limit of temperature where it can be used. In this study, new castings were designed using a cold crucible levitation melter. The device allows us to handle small quantities (from 1g to 1kg) of experimental material with a minimal contamination by suspending and melting the conductive alloy using an important magnetic field. Blocks of raw material were introduced

with the desired alloying elements in a copper crucible which is cooled by a water system. A secondary vacuum (6.10^{-6} Pa) was then obtained in the melter chamber, prior to filling it with argon. This step is necessary to avoid any oxidation during the melting process. A strong magnetic field gradient is accomplished thank to the use of helical conical induction coils and the vertical stability was achieved by using a reverse direction coil (known as bucking plate) on the top of the conical coil. Those two parts of the induction furnace create a "null" where the metal remains. The metal melts by induction and the molten mass is maintained at the levitational point. The molten mass is free of impurity and mechanical interferences in this specific zone. At the end of the casting process, the molten alloy is dropped into a copper mold for forming when the magnetic field is shut down. The castings made by this method were then hot rolled and have followed a similar heat treatment as the reference material to obtained identical mechanical performances.

REFERENCES

[1] B. Pierragi, Oxidation of Metals , 27 (1987) 177.
[2] C. Choux, PhD thesis, University of Bourgogne, Dijon, France (2008).
[3] Groupement De Recherche du CNRS EVAPE n°3054 (Etude du vieillissement à haute température de matériaux métalliques sous vapeur d'eau), réunion du 03 et 04 Juillet 2008, Dijon, France (2008)
[4] A. Agüero, R. Muelas, M. Gutierrez, R. Van Vulpen, S. Osgerby, J.P. Banks, Surface Coatings Technology, 2001 (2007) 6253.
[5] A. Agüero, V. Gonzalez, M. Gutierrez, Defect and Diffusion Forum , 289 (2009) 243
[6] G. Plusquellec, Rapport de stage 2^{ième} année Ecole Supérieur d'Ingénieurs de Recherche En Matériaux (ESIREM), University of Bourgogne, Dijon , France (2009).
[7] J. Mougin, PhD thesis, Institut Polytechnique de Grenoble, Grenoble, France (2001).
[8] S. Henry, PhD thesis, Institut Polytechnique de Grenoble, Grenoble, France (2000).
[9] A. Brevet, PhD thesis, University of Bourgogne, Dijon , France (2004).
[10] R. Benadoud, P. Bouvier, J.P. Petit, Y. Wouters and A. Galerie, Journal of Nuclear Materials, 360 (2007) 151.
[11] S. Henry, J. Mougin , Y. Wouters, J.P. Petit and A. Galerie, Materials at High Temperatures, 17 (2000) 231.
[12] Y. Wouters, A. Galerie, P. Bouvier, M. Mermoux and J.P. Petit, Materials at High Temperatures, 22 (2005) 315.
[13] Y. Wouters, A. Galerie and J.P Petit, Materials Science Forum (2008).
[14] H.N. Evin, O. Heintz, C. Föjer, S. Jakani, A. Dhont, S.Chevalier, proceeding Eurocorr2009, Nice, France (2009).
[15] L. Baunier: Microscopie des défauts cristallins, Ecole thématique Saint Pierre d'Oléron 2001, Société Françaises des Microscopies, Chapitre III.4, 405.
[16] A. Perron, Periodic consortium report Y2 (D1.2), IDEAL-Cell project, 128.
[17] S. Chevalier, J. P. Larpin, Acta Materiala, 50 (2002) 3105.
[18] S. Chevalier PhD thesis, University of Bourgogne, Dijon, France (1998).
[19] S. Chevalier, G. Bonnet, J. P. Larpin , Applied Surface Science 167 (2000) 125
[20] S. Chevalier, M. Kilo, G. Borchardt, J. P. Larpin, Applied Surface Science, 205 (2003) 188.
[21] K. Eisentrant, R. E. Sievers : Journal of American Society , 20 (1965) 5254.
[22] C. Houngninou, PhD thesis, University of Bourgogne, Dijon, France (2004).
[23] G. Bertrand, PhD thesis, University of Bourgogne, Dijon, France (2000).
[24] C. Choux, A. Kulinska, S. Chevalier, Intermetallics, 16 (2008) 1.
[25] Z.D. Xiang, J.S. Burnell-Gray, P.K. Datta, Journal of Materials Science, 36 (2001) 5673.
[26] C. Houngninou, S. Chevalier, J.P. Larpin, Applied Surface Science, 236 (2004) 256.

III. Fire side corrosion of 9%Cr steel.

This chapter will introduce results obtained on 9% Cr steel in dry laboratory air, at 600°C, 650°C, 700°C, and 750°C. **A particular attention will be paid to 650°C which was the targeted temperature for this project**. Characterization of samples using different tools presented previously, were necessary from time to time for apprehending the oxide scale formation, its composition, and its long term behavior. Here, the results obtained at 600°C will be used to describe what happened during the first step of the oxidation. At 700°C or at higher temperatures the results will help to highlight the limits of the material. Indeed, the important effort of analysis and characterization realized in this part of the work will bring information on the oxide scale structure which is not presently available in the literature.

III.1 Kinetic study

Isothermal oxidation tests were performed on 9% Cr steel grade between 600°C and 750°C for 80 h in laboratory air in atmospheric pressure. Figure III.1 summarizes the oxidation kinetic curves ($\Delta m/A$) = f(t), where Δm is the net mass gain, and A the surface area of the coupons.

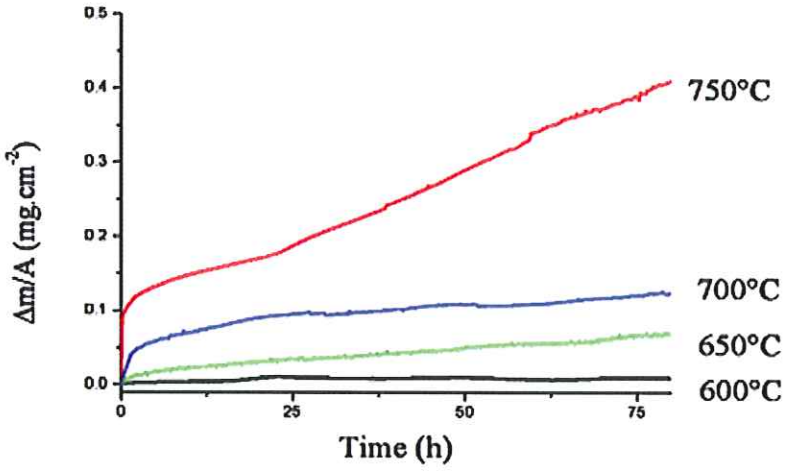

Figure III.1: Kinetics curves for 9%Cr steel grade after oxidation in laboratory air at atmospheric pressure for 100h between 600°C and 750°C

As a general trend, raising the temperature leads to an increase in the mass gain. A "breakaway" occurs at 750°C after 25 hours. A linear shape of the mass gain curve can be observed from that point until the end of the experiment. The kinetic curves obey appreciatively a parabolic rate law, except after the breakaway at 750 °C. Parabolic rate constants, k_p, calculated from the slope of the curve: $\Delta m/A=f(t^{1/2})$ [1], are listed in Table III.1. Activation energy of 391 $kJ.mol^{-1}$was calculated from Arrhenius' plot based on the parabolic rate constants. This activation energy is higher than that reported in the literature [2-4] for chromia forming alloys such as Fe30Cr. This difference could be explained by the lower amount of chromium contained in the bulk and the relative complexity of the oxide scale which is probably not a pure chromia layer as observed for Fe30Cr.

Temperature (°C)	600°C	650°C	700°C	750°C
k_p ($g^2 .cm^{-4} .s^{-1}$)	$1.3x10^{-16}$	$2.8x10^{-14}$	$1.7x10^{-14}$	$9.6x10^{-13}$

Table III.1: Kinetic rate constants between 600°C and 750°C.

Wavy variations are observed on the kinetics curves. Those slight variations are not entirely explained but a few ideas could be proposed:

- Volatilization of chromium oxide or oxo-hydroxide can take place which would be characterized by low mass loss of the samples. But, in our case, the periodicity of the variations are unlikely due to this phenomenon

- The local cracking of an oxide layer followed by its healing, which is the formation of another oxide between the cracks, may also be a good hypothesis for the explanation of the wavy variations observed on the samples mass gain curves.

- The most likely hypothesis concerning those undulations relies upon the changes in the room temperature where the thermobalance, used for the experiment, is situated. Indeed those temperature variations can have physical impacts on the properties of the head of the thermobalance by disrupting the data acquisition. Maintaining the temperature of the thermobalance head constant could prevent these measurement artifacts.

III.2 Oxide Scale morphologies

SEM micrographs coupled with EDX analyses show the oxide layer morphology at different temperatures (Figure III.2).

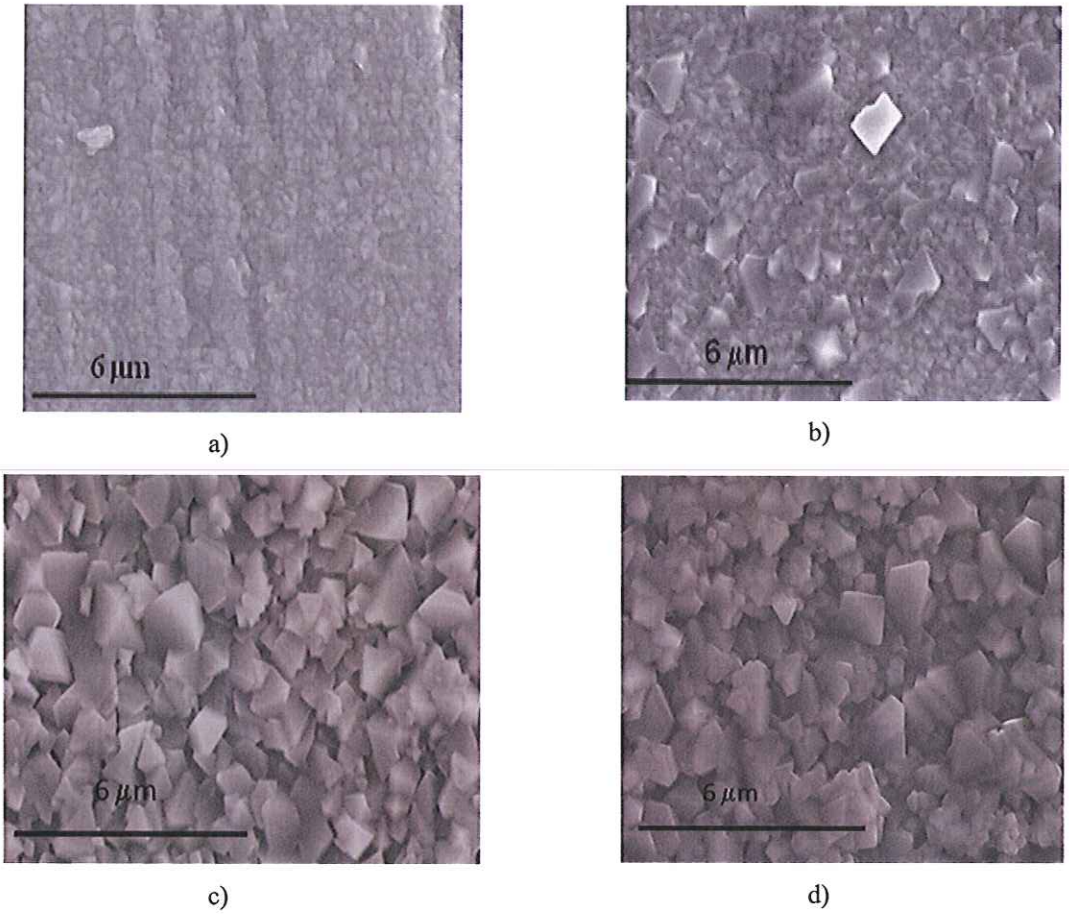

a) b) c) d)

Figure III.2: SEM micrographs of samples surface oxidized for 100 h in air at: a) 600°C, b) 650°C, c) 700°C, and d) 750°C.

At 600°C, (Figure III.2a)) a very thin oxide scale could be observed. Polishing marks made prior to the isothermal test are still visible. The oxide layer is composed of small spherical nodules made of iron, chromium, silicon and manganese according to the EDX analyses. After 100 hours at 650°C (Figure III.2b)), the oxide scale seems thin, and the sample is covered by an iron – chromium oxide scale, where it is possible to observe among the nodules some geometrical crystallites. Those geometrical crystallites are clearly visible on micrographs which were taken after 100 hours at 700°C (Figure III.2c). They grew over an iron chromium oxide scale. At 750°C after 100 hours (Figure III.2d), chromium oxide, chromium manganese

geometrical oxide (probably as a spinel oxide) and a chromium iron oxide scale beneath it are identified. Iron oxide needles are visible on many places on the sample surface oxidized at 750°C. They could be related to the breakaway observation on the kinetic curve.

XRD analyses were performed at low glancing angles in order to give information on phases grown in the thin oxide scales. At 600°C and 650°C, difficulties were faced to identify the growing phases due to the thickness of the scale and the close lattice parameters of chromia and hematite. Figure III.3, which is a superposition of patterns collected on samples oxidized for 100 hours at 600°C, 650°C, 700°C and 750°C underscored the similitude between the magnetite and the spinel oxides and revealed how delicate the patterns indexation can be.

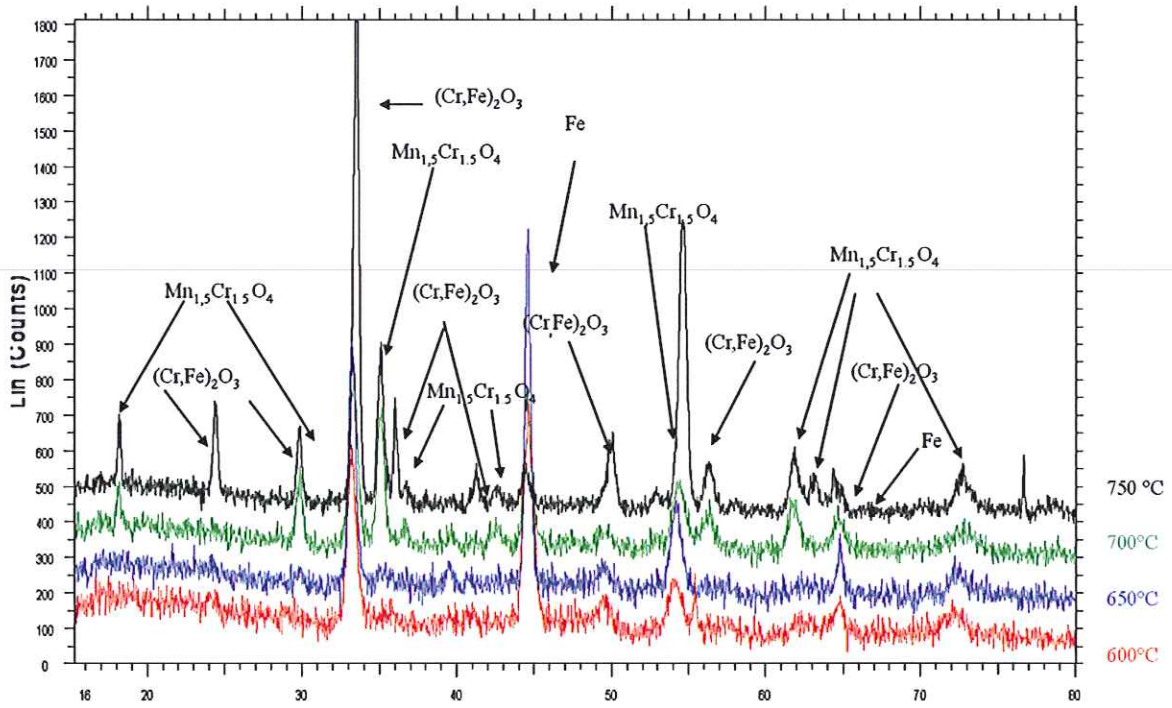

Figure III.3 : XRD pattern at low glancing angles (θ = 1°) of sample oxidized for 100 h at 600°C, 650°C, 700°C, and 750°C in laboratory air at atmospheric pressure.

At 700°C and 750°C presence of hematite and magnetite as well as $(Cr,Fe)_2O_3$ and spinel oxide ($Mn_{1.5}Cr_{1.5}O_4$ from ICDD n°033-0892, and/or $FeCr_2O_4$ slightly from ICDD n° 034-0412 and/or $MnFe_2O_4$ slightly from ICDD n°010-0319) is suspected. When the temperature increases, no more base material is detected on the pattern, which signifies that the oxide scale is thicker.

***Synthesis:* XRD at low glancing angles.**
At 600°C and 650°C difficulties to identify phases on thin oxide scales.
At 700°C and 750°C, Fe_2O_3, Fe_3O_4 are the main phases. $(Cr,Fe)_2O_3$ and spinel phases are also detected

III.3 Scale characterization, composition and mechanism

The previous analyses could not lead to a clear schematic of the composition of the oxide layer thermally grown on the 9% Cr steel used for this study. In order to further increase our knowledge on the oxide scale growth, several characterization tools were consequently used to gather information on the corrosion products. Put together, those data can give a clear idea of the oxidation process and the oxide scale composition when this 9%Cr steel is oxidized in a dry atmosphere.

III.3.1 PhotoElectroChemistry Spectroscopy results (PEC)

The PhotoElectroChemistry (PEC) experiment developed by Pr. Y.Wouters at the SIMaP laboratory Grenoble (Grenoble INP, France), allows us to identify oxide scale composition by characterizing the semi-conductivity behavior of the different oxides layers. Chromia shows two different band gaps for two semi-conduction behavior. A first bandgap at 3 eV, corresponding to a n type semi-conductivity and a band gap at 3,5 eV corresponding to a p type semi-conductivity. In case of iron oxides characteristic band gap is considered to be between 2 and 2.2 eV [5-8].

Figure III.4 summarizes the results obtained for samples oxidized at 600°C for 100h at fixed energy. On the left from top to bottom the total registered current, the phase angle and the photocurrent versus the energy are plotted. On the right from top to bottom, the corrected photocurrent versus the energy and the $(Iph \times h\nu)^{1/2} = f(h\nu)$ which will allow characterizing the gaps of the oxides within the scale.

A stable intensity current is observed, and no change in the phase signals is registered. Despite a low signal over noise ratio the photoelectrochemical response function of light energy showed one peak characteristic of a n-type semi-conductivity. The classical square root mathematical transform $(Iph \times h\nu)^{1/2}$ vs $h\nu$ leads to the determination of a bandgap value of 3eV (C1) .

Similar comments could be made on photoelectrochimical results obtained for the oxide scale grown on the sample oxidized at 650°C for 100h. As seen in Figure III.5, a highly defected

oxide layer gives a low signal over noise ratio; it is then difficult to stabilize the photocurrent. A 3eV (C1) band gap is highlighted by method similar to that previously described.

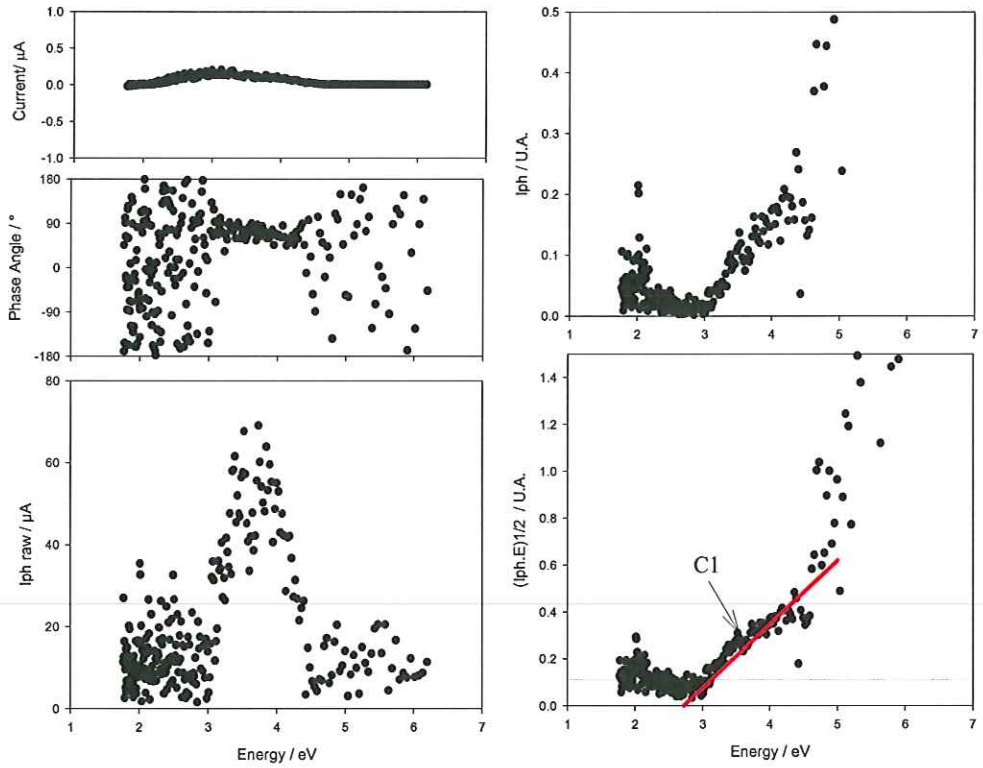

Figure III.4: Photoelectrochemical responses in energy measured in 0.1 mol.L^{-1} Na_2SO_4 for an oxide scale formed by thermal oxidation of P91 in laboratory air at 600°C for 100 h.

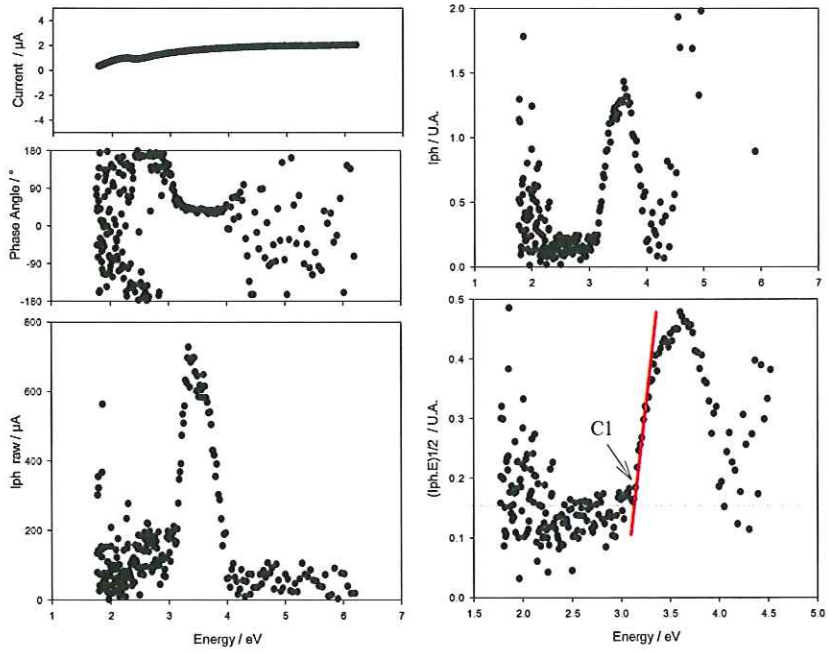

Figure III.5: Photoelectrochemical responses in energy measured in 0.1 mol.L^{-1} Na_2SO_4 for an oxide scale formed by thermal oxidation of P91 in laboratory air at 650°C for 100 h.

For characterizing the oxide scale grown on T91 after oxidation in laboratory air for 100 h at 700°C, a better signal over noise ratio is obtained. In Figure III.6, stable total intensity was registered. The non treated and treated photocurrent show clearly two n-type contributions which are highlighted by the changes of the slope of $(\text{Iph X } h\nu)^{1/2}$ vs $h\nu$ plotted curve. Therefore, two distinguished band gaps have been calculated the first one is 2.2 eV (C1) and the second one is 3eV(C2).

A 90° phase change is also observed which indicate a possible p-type semi-conductivity contribution in the photocurrent signal. Such a contribution is guessed on the $(\text{Iph X } h\nu)^{1/2}$ vs $h\nu$ plot with a bang gap at around 3.5 eV. But, as several contributions overlap each other, it is impossible to identify with certainty the last contribution peak foot.

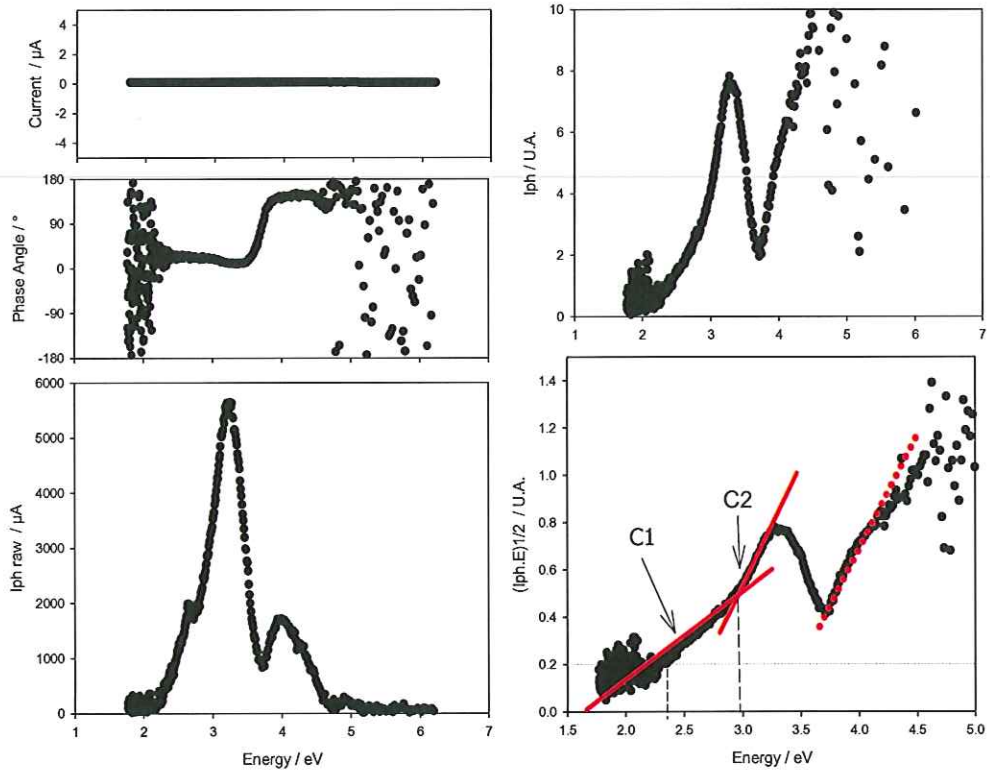

Figure III.6 : Photoelectrochemical responses in energy measured in 0.1 mol.L^{-1} Na_2SO_4 for an oxide scale formed by thermal oxidation of P91 in laboratory air at 700°C for 100 h.

At 750°C for 100h in laboratory air, similar photoelectrochimical results as previously commented are obtained. In Figure III.7, two n-type contributions are observed: A first one with a calculated band gap at 2 eV (C1) and a second one at 3 eV(C2). A third contribution with a band gap around 3.8 eV is also supposed in the $(\text{Iph X } h\nu)^{1/2}$ vs $h\nu$ curve.

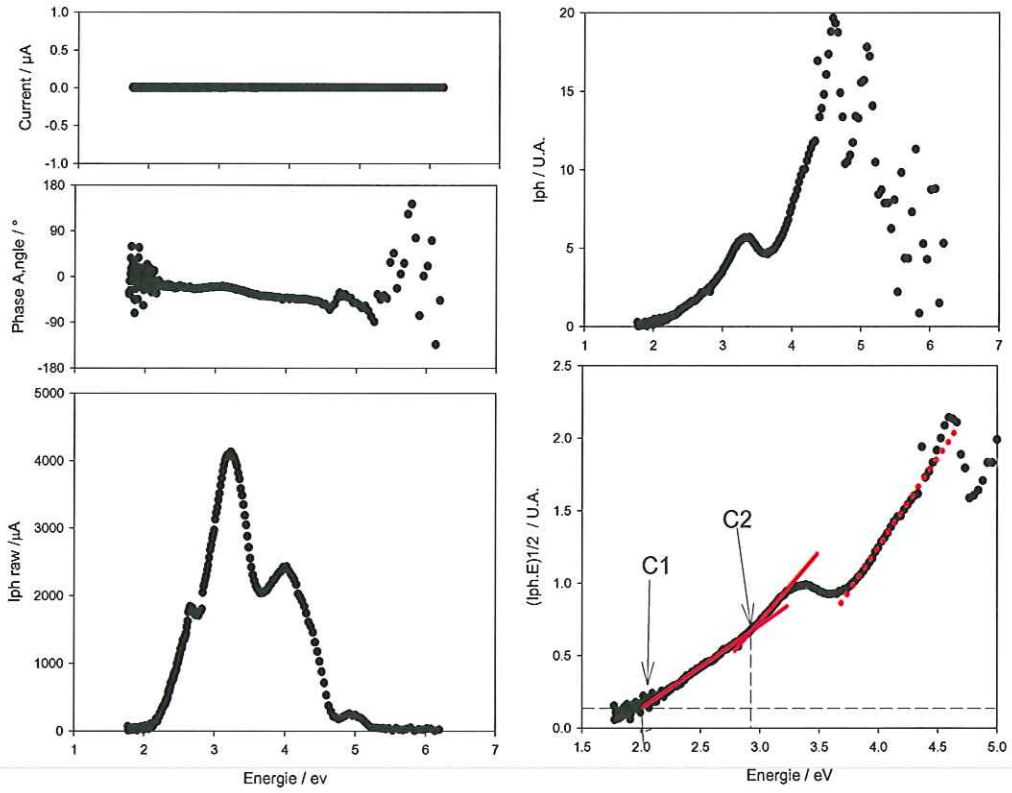

Figure III.7: Photoelectrochemical responses in energy measured in 0.1 mol.L^{-1} Na_2SO_4 for an oxide scale formed by thermal oxidation of P91 in laboratory air at 750°C for 100 h.

Figure III.4 and Figure III.5 clearly evidence the contribution of a n-type semi conductor. Considering the transformed $(Iph \times h\nu)^{1/2} = f(h\nu)$, a band gap value at around 3eV is calculated for both samples oxidized at 600°C and 650°C. Due to the important noise, no other band gap was possible to identify. According to the literature, this band gap corresponds to chromia grown at low oxygen partial pressure [6-8]. A highly disturbed oxide layer enriched in chromium could be formed at the top surface of the samples oxidized at those temperatures. After oxidation at 700°C and 750°C, less disturbed oxide scales grew on the samples. In Figure III.6 and Figure III.7, it is possible to distinguish two different n-type contributions: a first one with a band gap at around 2.2 eV and a second one with a band gap at around 3eV. These band gap values are respectively characteristic of iron oxide and chromia oxide [7-8]. Moreover, a 90°change in the phase angle in (Figure III.6) combined with a change observed in the slope of the curve $(Iph \times h\nu)^{1/2} = f(h\nu)$ (Figure III.6 and Figure III.7) allow us to suppose the existence of a third contribution which would be a p-type semiconductor with a band gap between 3.5-3.8 eV. Therefore, one could think that at temperature higher than 700°C the oxide layer is composed of iron oxide and chromia. As very little knowledge is available about iron chromium spinel oxides band gap values, it is

still possible to discuss the hypothesis relying on the formation of a chromium rich spinel oxide which will be enriched in iron oxide when increasing the temperature.

Synthesis:PhotoElectroChemistry				
	600°C	650°C	700°C	750°C
Band gap	3eV	3eV	2.2eV and 3eV	2.2 and 3eV
Possible phases	Chromium oxide at low P_{O_2}	Chromium oxide at low P_{O_2}	Iron oxide and Chromium oxide at low P_{O_2}	Iron oxide and Chromium oxide at low P_{O_2}

III.3.2 RAMAN Spectroscopy Results.

The thickness of the oxidation products after 100 hours at high temperature, seems to be the limiting element which generates troubles in the interpretation of the obtained data by EDX, XRD or even by photoelectrochemistry spectroscopy. Indeed, at 650°C for 100 hours of oxidation example the oxide layer is around 100 nm thick (Figure III.16 a)). Therefore, it has been decided to work on a cross section of a sample oxidized at 700°C for 700 hours where it is sure to have an oxide layer thick enough to be observed using SEM and RAMAN spectroscopy(Figure III.8). A relatively thick oxide scale (500 µm) is seen. Pores are observed both in the oxide layer and at the interface metal/oxide. The presence of these pores could be a sign of outward cation diffusion within the scale and their effect on the growth of oxide on top of the substrate. The EDX profiles give an idea of the repartition of the elements in the scales. At the upper surface, only iron and oxygen are present, chromium is detected at a distance of 180 µm from the top surface. Silicium is detected in the scale close to the oxide/metal interface.

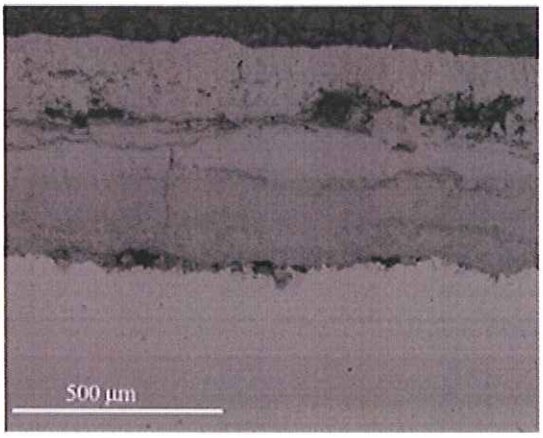

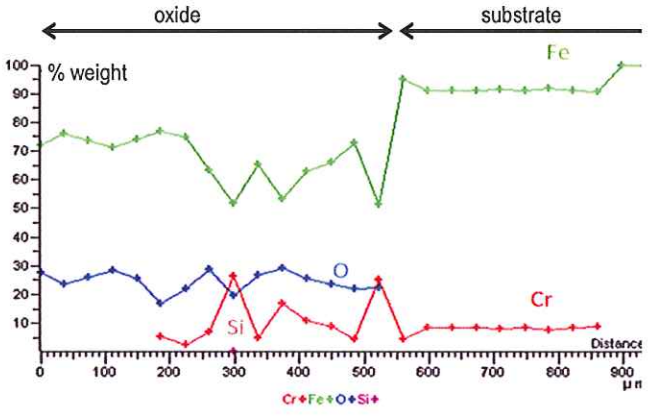

Figure III.8: SEM cross section and EDX profiles on 9%Cr steel oxidized for 700h at 700°C in laboratory air under atmospheric pressure.

Raman analyses were performed on this cross section of the samples oxidized at 700°C for 700 hours. Several spectra were registered from the top of the oxide scale to the substrate. Figure III.9 is a superposition of these spectra with the spectrum registered from commercial chromia and hematite powders.

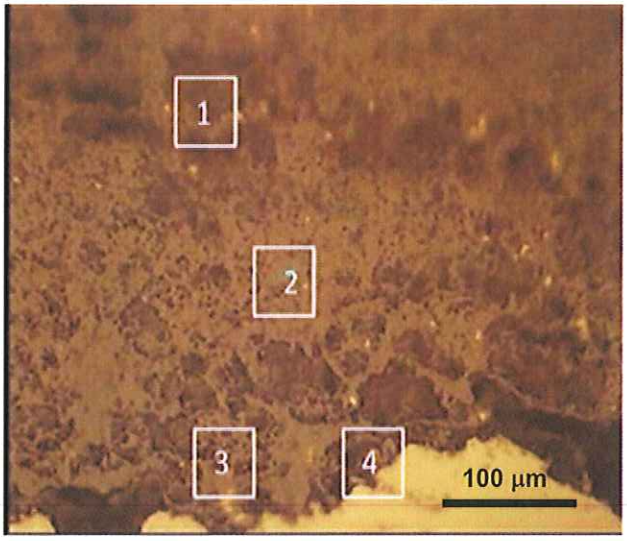

Analysis position in at the interface metal/oxide

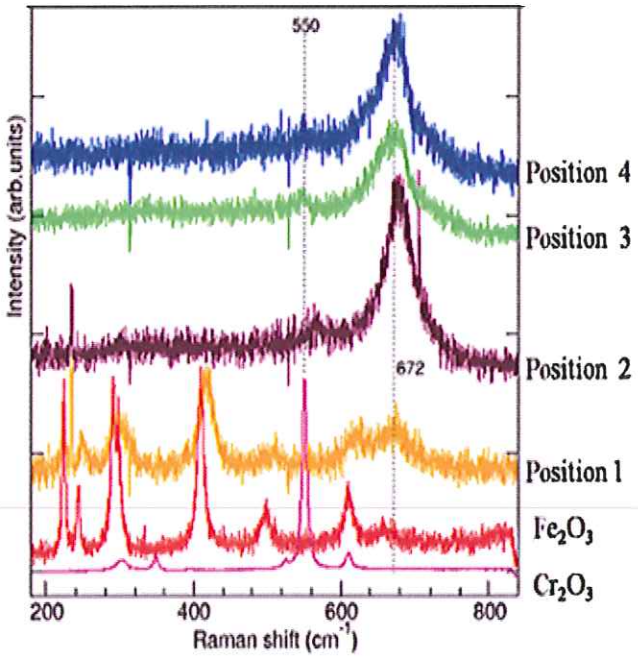

Figure III.9: Raman spectra registered on 9%Cr steel sample cross section after oxidation at 700°C for 700h in laboratory air under atmospheric pressure.

Close to the oxide top surface (Spectra 1), peaks, characteristic of hematite Fe_2O_3 but with an important broadening were highlighted. A peaks with low intensity at (672 cm^{-1}) was also observed. This band is linked to the presence of magnetite Fe_3O_4 in the layer.

Deeper in the layer, (spectrum 2), peaks characteristic of magnetite are mainly observed. Close to the substrate (spectra 3,4) peaks of magnetite are also identified nevertheless at 550 cm^{-1}, a band with low intensity exists and could be characteristic of chromium oxide. This observation should be taken cautiously, because magnetite has also a peak in this region (532 cm^{-1}).

***Synthesis:* Raman (Thickness of the oxide investigated 500µm)**
At the Top surface on Fe_2O_3 is detected. In the center of the layer (250-300 µm of deepness) Fe_3O_4 is detected. Close to the metal/oxide interface a mixture of Cr_2O_3 and Fe_3O_4 is suspected.

III.3.3 In-situ and ex-situ XPS results.

The information obtained thanks to the RAMAN spectroscopy are post "breakaway" data. Indeed, the cross section shows thick oxide scale mainly composed of iron oxide. Within the aim to prevent catastrophic oxidation behavior of the steel during its exposition at high temperature, it is necessary to have a set of data on the very first instants of oxidation.

Therefore, X-ray Photoelectron Spectroscopy analyses were performed on in-situ and ex-situ oxidized samples with the equipment described in chapter II paragraph II.3.5.

In-situ analyses were performed on samples oxidized at 600°C in laboratory air at atmospheric pressure for different time exposure. Figure III.10 summarizes the spectra registered after 5 min, 30 min, 1 hour of oxidation.

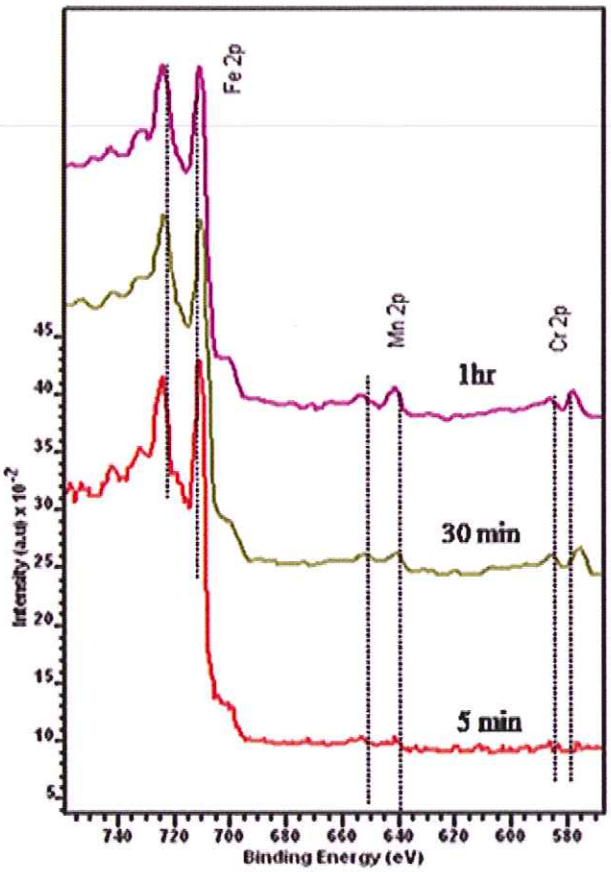

Figure III.10: XPS spectra registered on 9%Cr steel oxidized in situ at 600°C for (from bottom to top) 5 min, 30 min, 1h in air under atmospheric pressure.

For all samples Fe 2p signals exhibit two important peaks. The first one is close to 711 eV and the second one is centred at 724 eV. They correspond respectively to Fe $2p_{3/2}$ and $2p_{1/2}$ contributions of iron oxide. Figure III.11 compares the evolution of iron oxide peaks from the

starting material to samples oxidized at 600°C for 5 min, 30 min, and 1 h. Within the Fe $2p_{3/2}$ peaks, two distinct contributions, one at 710,6 eV and the other at 711,4 eV, could be identified thanks to data reported in previous work [9-15]. They correspond respectively to Fe (II) and Fe(III) oxidation level. Around 641.5eV and 654 eV signals corresponding to manganese oxide $2p_{3/2}$ and $2p_{1/2}$ are also identified. Similar values were reported in the literature [16,17]. It is worth noting that Mn signal intensities increase with oxidation time. Cr 2p contributions are also observed with two signals, $2p_{3/2}$ at around 576 eV and $2p_{1/2}$ at 588 eV. These signals show low intensity for 5 min oxidation time; their intensity becomes higher for 30 min and 1 h oxidation time. When focusing on the $2p_{3/2}$ contributions for Cr species for more than 30 min of exposition in oxidizing atmosphere a split into two different peaks is clearly visible in Figure III.12.

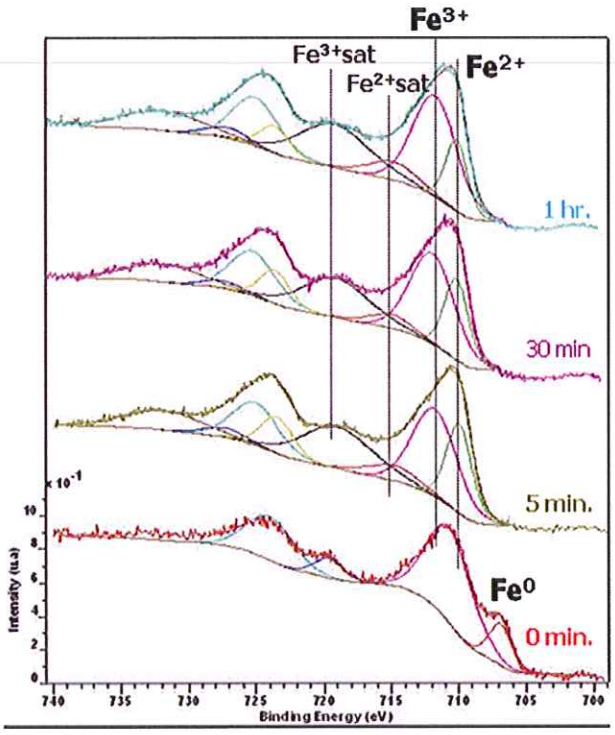

Figure III.11: Fe 2p level signals registered on 9%Cr steel samples oxidized in situ at 600°C for 5 min, 30 min, 1hour in air under atmospheric pressure.

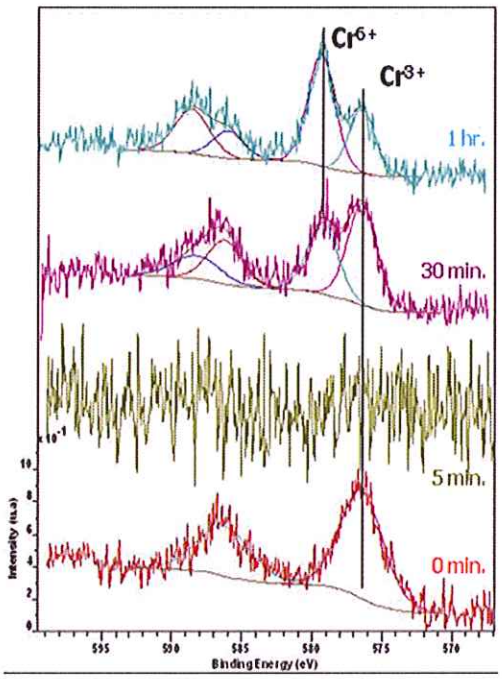

Figure III.12: Cr 2p level signals registered on 9%Cr steel samples oxidized in situ at 600°C for (from bottom to top) 5 min, 30 min, 1 h in air under atmospheric pressure.

The first one centred at 576 eV is characteristic of chromia and the second one is centred at 579 eV which is characteristic of Cr (VI) species. Such species have been identified in similar conditions in the literature [18,19]. The relative intensity between those two peaks changes as function of oxidation time as shown in Figure III.13.

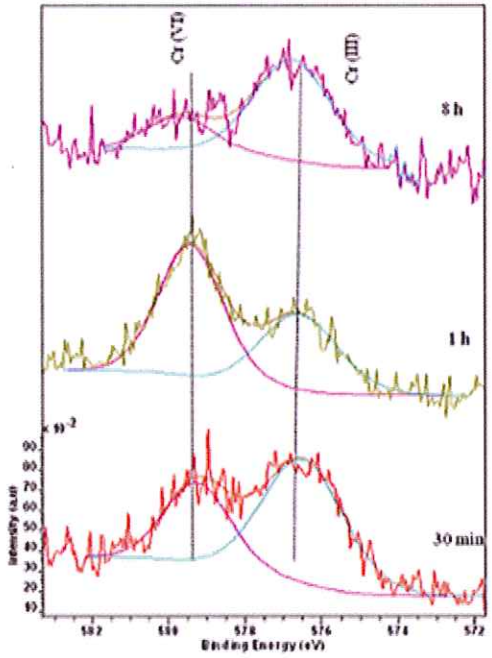

Figure III.13: XPS Cr $2p_{3/2}$ signals for sample after in situ oxidation f at 600°Cfor from bottom to top 30 min, 1 h, 8 h.

Complementary in-situ XPS analyses were performed for longer exposure time (15 min, 8 hours, 24 hours) in oxidizing atmosphere within the same condition as described in the previous section. As a general trend for the intensity evolution of Cr (VI) and Cr (III) peaks, one could state that for short oxidation time the main peak observed is characteristic of Cr (III). After 15 min of oxidation, Cr (VI) contribution is identified and is higher, than the Cr (III) contribution until 8 hours of oxidation. For periods longer than 8 hours, it is Cr (III) which is predominant among the Cr oxide species. Moreover, semi-quantification using calculation from signal areas corresponding to Fe, Mn and Cr species also gives a trend of the relative evolution of those species within the formed oxide scale (Table III.2).

Time	C1s %	Cr2p %	Fe2p %	Mn2p %	O1s %
5 min	14	0.1	35.	0.90	50
15 min	18	1.3	27.6	1.4	51.7
30 min	18.3	3.6	23.3	1.5	53.3
1 hour	7.3	3.8	24.7	2.2	62
8 hours	13.6	2.4	23.2	4.2	56.6
24 hours	18.8	1.1	17.5	6.5	56.1

Table III.2: XPS analyses semi-quantification

According to those results, iron oxide species appear to be the more prominent phase in the scale when oxidation time increases. Cr oxide species appear to be more present for short time exposure, whereas Mn oxide species follow the opposed evolution. To complete these analyses, XPS profiles were performed on samples oxidized ex-situ at 600°C for 100 hours in air at atmospheric pressure (Figure III.14).

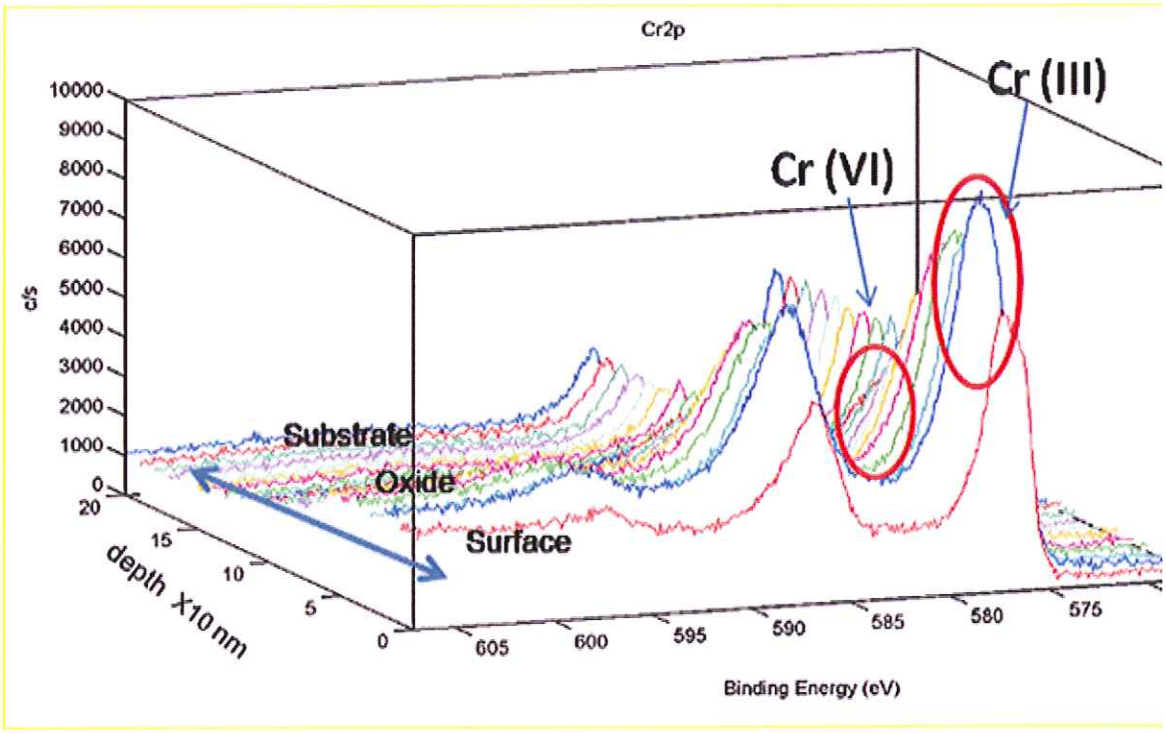

Figure III.14 : XPS Cr 2p profile for 9%Cr steel oxidized for 100 hours at 600°C in air under atmospheric pressure

Figure III.14 summarizes successive XPS spectrum for Cr 2p signals registered from the top surface of the oxide scale to the substrate. For the $2p_{3/2}$ energy level, Cr (III) peaks are the main contributions observed at the surface. Within the scale, a shoulder appears on the $2p_{3/2}$ signal, which is centred at 579 eV. Those results are in agreement with what was observed previously for the in-situ XPS spectra and indicate the presence of Cr (VI) species in the oxide scale. It is important to note that phase modification due to Ar sputtering effects could not have been responsible for the present results. Indeed, those effects usually lead to reduction of the species and not oxidation as observed in this case (Cr VI species).

To go further in the understanding of the oxide scale growth mechanism; the same substrate was oxidized at 650°C in-situ and analysed by XPS. Figure III.15 shows XPS results on short term in situ oxidized samples at 650°C for 15 min and 30 min. The iron and chromium signals observed at 650°C are similar to what has been previously seen for 600°C. Therefore similar conclusions could be proposed in both cases.

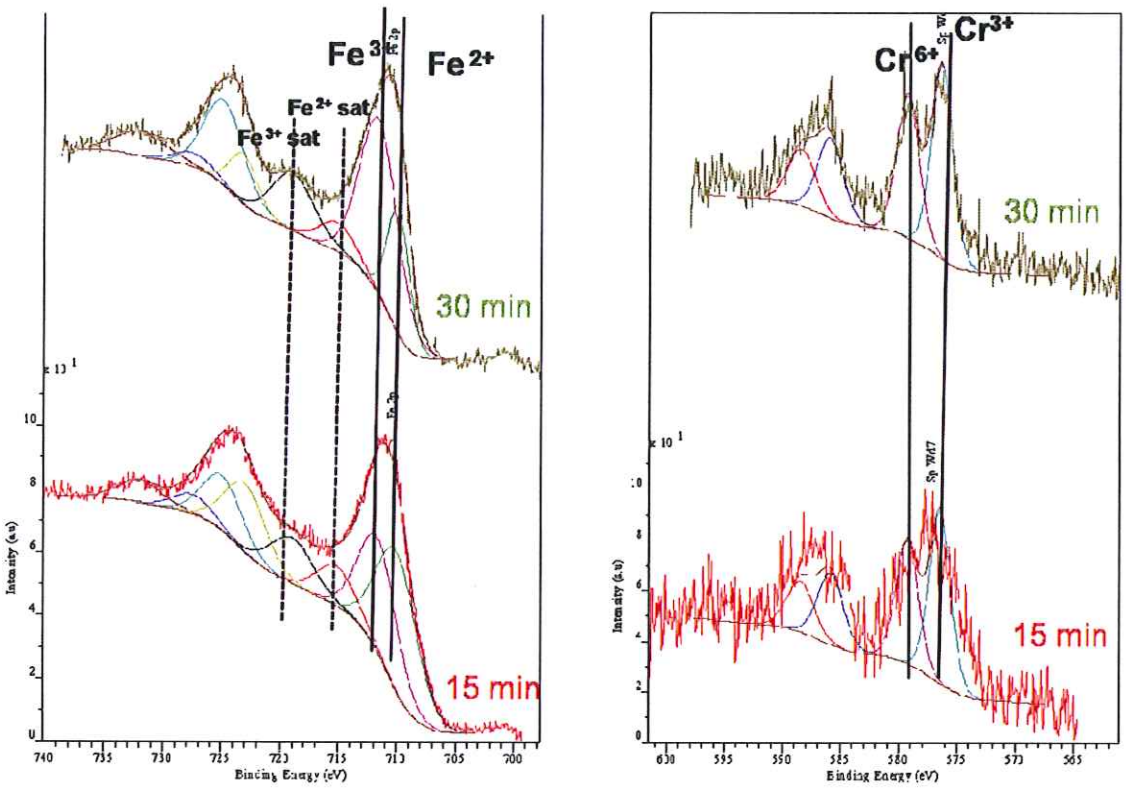

a) b)

Figure III.15 : a) Fe 2p level signals registered on 9%Cr steel oxidized in situ at 650°C for (from bottom to top) 15 min, 30 min in air under atmospheric pressure; b) Cr 2p level signals registered on 9%Cr steel samples oxidized in situ at 650°C for 15 min, 30 min in air under atmospheric pressure.

The XPS results show that the scale is mainly composed of iron oxide, which could be magnetite or a mixture of hematite and magnetite. This is in agreement with the main phases characterized by Ennis et al. [20]. Below the iron oxide layer, a zone enriched in chromium oxide species could be found. Two different scenari could be proposed for this sub layer. A first one where Cr (III) and Cr (VI) detection could suggest that during the first stage of oxidation, there is formation of a non protective, non compact and inhomogeneous Cr_2O_3 layer and a few nuclei of CrO_3 beneath it. A second scenario consists in the formation of a non continuous layer of mixed spinel such as $(Fe,Cr)_3O_4$ as proposed by Wright [21] and Bénard [22], or other solid solutions of chromium in iron oxide. In that case, at 600°C and/or 650°C, Cr supply in the oxide scale by diffusion in the steel is not sufficiently fast. Therefore a spinel with an important chromium defect could be formed and explain the Cr (VI) detection. This spinel could be presented as follow: (Fe (II) Cr (VI)) O_4 or $[Fe(II)Cr(III)V_{Cr}''']O_4$. As a matter of fact, oxide growth is governed by the Cr diffusion in

the base alloy, as well as in the oxide scale. The manganese found in the scale, could form spinel oxides with chromium such as $Mn_{1.5}Cr_{1.5}O_4$ in the inner layer and form iron manganese oxide spinel, such as $MnFe_2O_4$, in the outer layer where the chromium concentration is lower.

Synthesis:* *In situ XPS :
For short time experiments oxide scales thickness (<30 nm) : Cr (IV) then Cr (III) are detected. Presence of Fe (II) is firstly highlighted then Fe (III) appears for longer exposure time where detected. Oxide growth mechanism governed by Cr diffusion is proposed. In the first step of oxidation the formation of a spinel structure with important Cr cations vacancies is discussed.

III.3.4 TEM results on thin cross section prepared by FIB

FIB cross section was performed on 9% Cr steel oxidized at 650°C for 100h in laboratory air under atmospheric pressure (Figure III.16). EDX localized analyses were performed on this FIB prepared cross section. FigureIII.16 b) presents the spectra obtained from three spots corresponding to (1) the oxide layer, (2) the substrate bulk, (3) the metal/oxide interface.
On the EDX 1 evidences oxygen, iron, chromium and manganese. It confirms the fact that, at this temperature, a complex oxide scale is formed. On all the spectra, copper peaks are also seen, they correspond to the composition of the sample support holder. EDX 2 corresponds to the substrate and mainly shows iron and chromium peaks. The corresponding semi quantitative analysis, gives around 9 wt. % of chromium and 90 wt % of iron which are clearly the bulk composition.

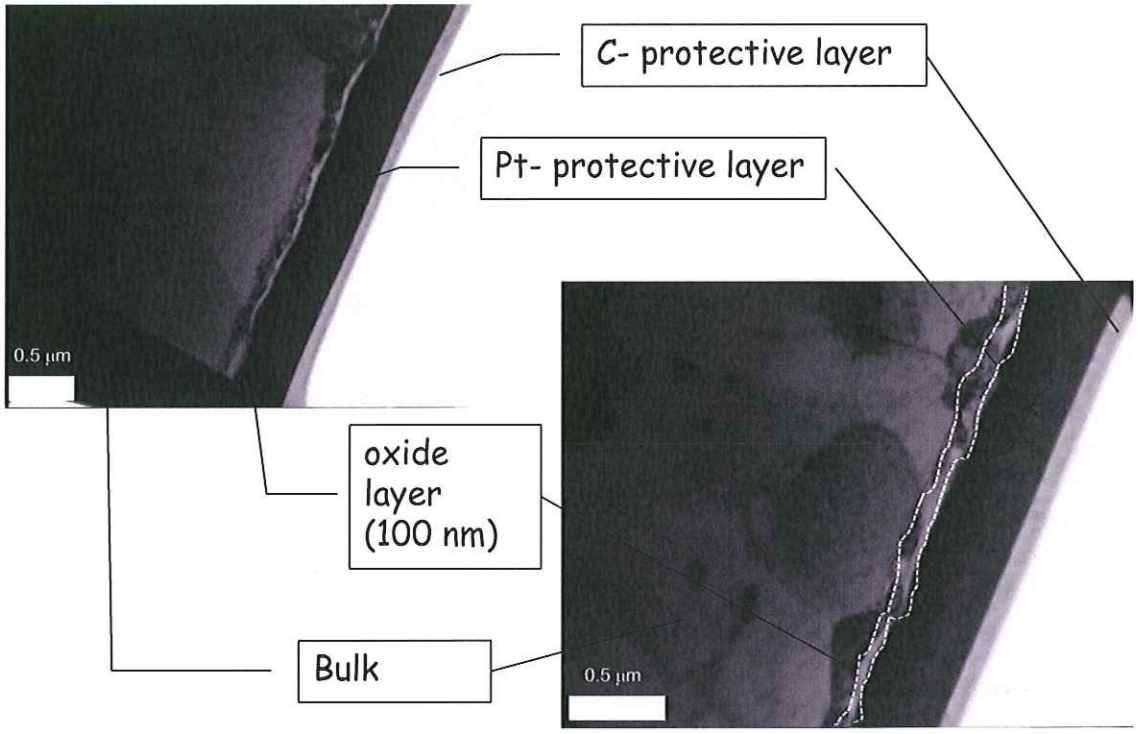

a)

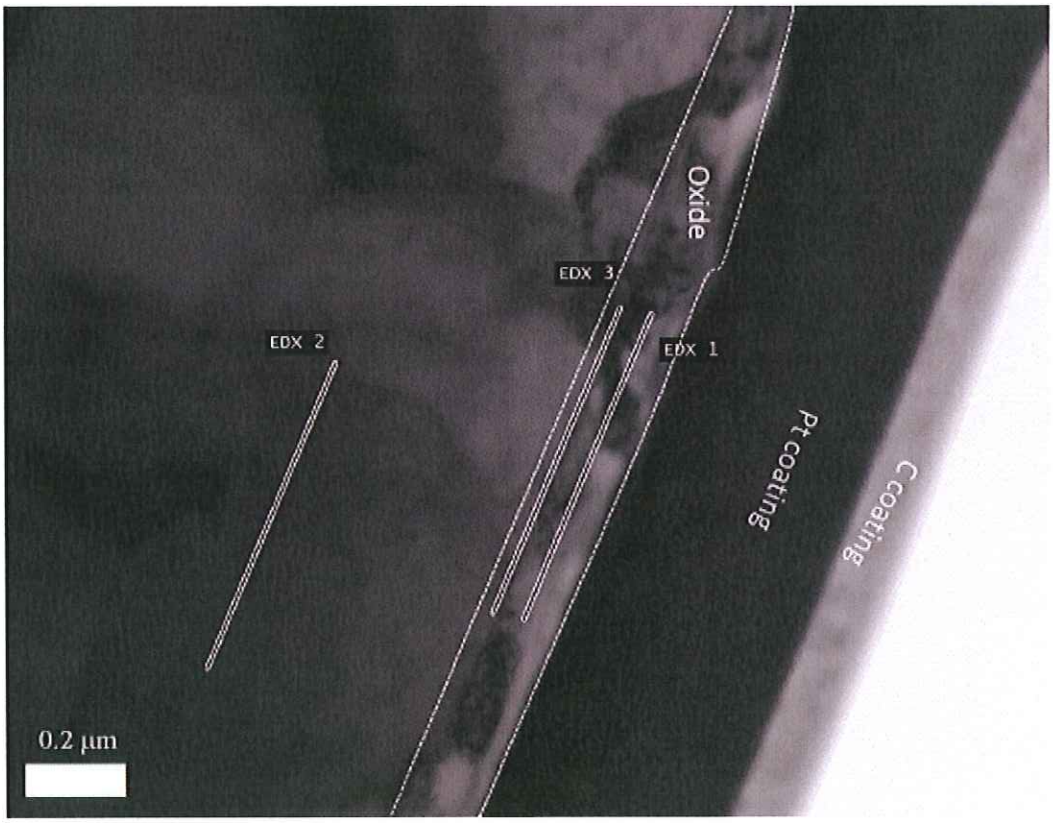

b)

Figure III.16: a) thin oxide film grown after 100 h at 650°C cross section realized by FIB, b) presentation of the EDX spots .

For the EDX 3, the analysis was performed at the metal/oxide interface. The results are similar to the one of EDX1. Nevertheless peaks characteristic of vanadium oxide and Silicon oxide are observed. Silicon is known to segregate at the metal/oxide interface and help to the oxide scale adhesion [23-29]. Vanadium is usually detrimental for the corrosion properties of steels [29].

Figure III.17 shows elementary mapping performed on the same FIB cross section previously discussed and gives an idea of the different element distribution within the oxide scale.

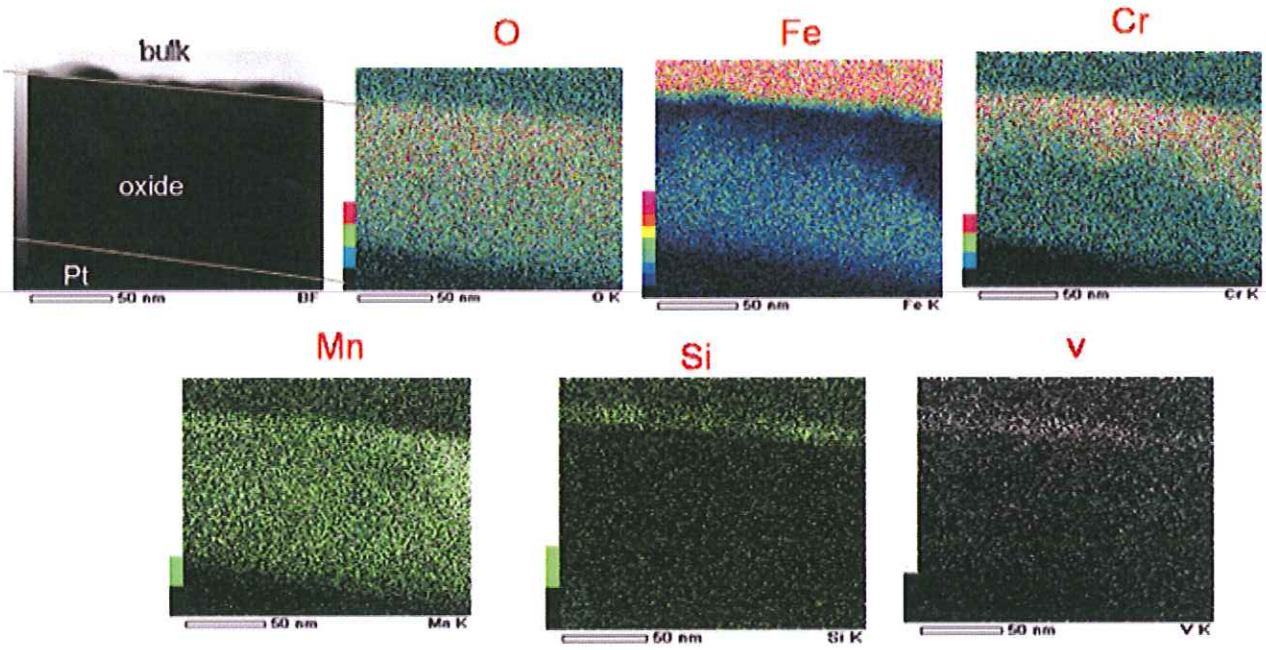

Figure III.17: EDX mapping performed on FIB thin of film after oxidation at 650°C for 100h

In Figure III.17, the different parts of the FIB cross section are designated by bulk, oxide, and Pt part. Oxygen is detected all over the surface of the samples with an important concentration in the oxide layer part. Iron is detected mainly in the bulk and from the middle to the top of the oxide scale. Chromium is mainly localized at the metal oxide interface. Manganese is present all over the sample and with a large concentration in the oxide scale. As previously observed, silicon and vanadium are present at the metal/oxide interface. This different information, leads us to propose an oxide scale with a multilayer structure. Indeed, at the interface metal/oxide, a thin layer of silicon and vanadium oxide is visible. Another layer with iron, chromium, and manganese oxides is formed close to the metal oxide interface. The top part of the scale is composed mainly of iron and manganese oxide.

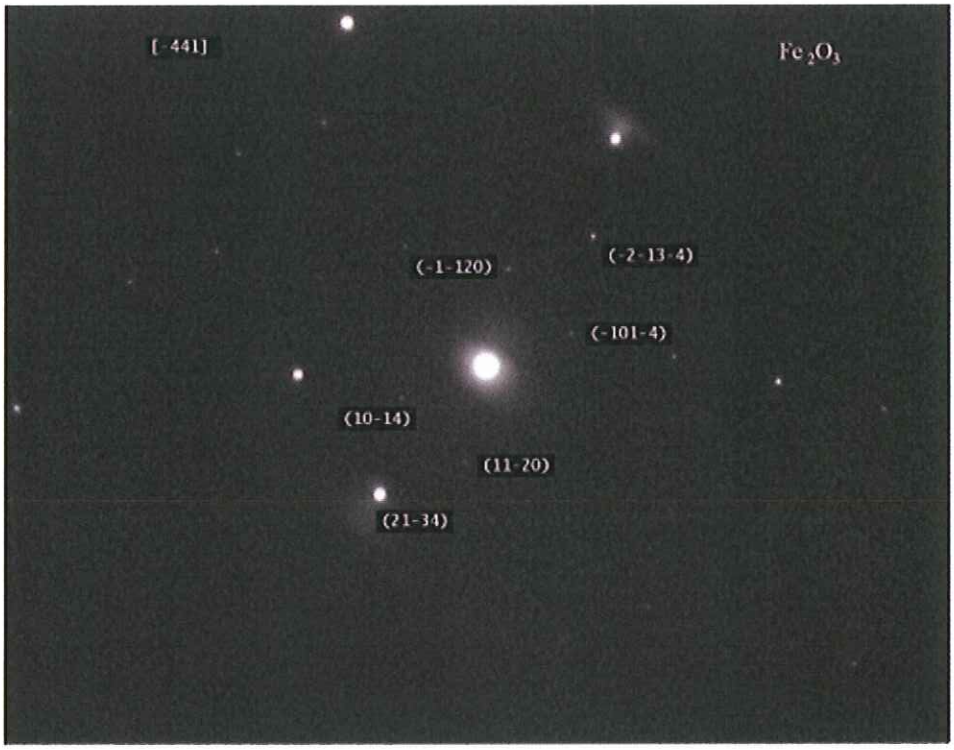

a)

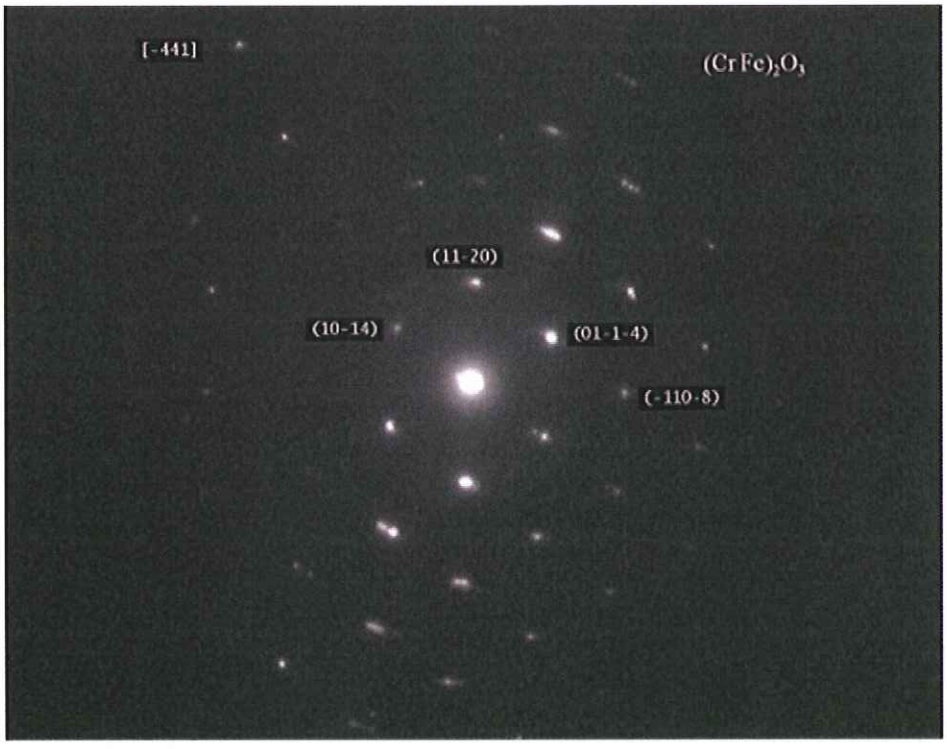

b)

Figure III.18: TEM selected area diffraction on thin film of 9%Cr steel oxidized at 650°C for 100 h in laboratory air at atmospheric pressure a) close to the gas/oxide interface b) close to the oxide/metal interface.

Selected Area Diffraction (Figure III.18 a) lead to the identification of Fe_2O_3 (corundum structure) as the main constituent forming the external part of the oxide scale.

This data confirms the hypothesis according to which the iron oxide found in the top part of the oxide layer is mainly hematite (Fe_2O_3).

Figure III. b) is a selected area diffraction of the inner part of the oxide scale. The EDX analyses and the measured interplanar spacings lead to characterize the presence of a chromium iron mix oxide $(Cr,Fe)_2O_3$.

***Synthesis:** TEM (oxide scale thickness < 100nm)*
Elements repartition within the oxide layer is presented. Cr is located in the inner layer; the outer layer is enriched in Fe; Mn is observed in all the scale. Si and Vanadium are seen at the metal/oxide interface. Fe_2O_3 is indentified in the outer part of the layer, and $(Cr,Fe)_2O_3$ presence is highlighted in the inner part of the oxide scale.

III.3.6 In-situ high resolution powder diffraction experiments using synchrotron facilities (ESRF Grenoble).

It has been clearly shown that the oxide scale thermally grown at high temperature on 9%Cr steel is composed of several phases. A high resolution diffraction experiment using the synchrotron facilities was necessary to characterize with accuracy the formed oxides. A proposal was submitted at the European ESRF in Grenoble; four days were allocated on the ID31 high resolution powder diffraction beamline. As the allocated beamtime do not allow long experiments at 650°C, in-situ diffraction analysis were carried out at 750°C on 9%Cr coupon in 200 mbar of oxygen, in order to underlined the sequence of apparition of the different phases as a function of the exposure time. Figure III.19 a) shows the presence of two different chromium iron oxides. The first one for $2\theta = 8.47°$ corresponds to the main peak of iron oxide enriched in chromium according to the ICDD n° 034-0412 that we will refer to as $(Fe,Cr)_2O_3$; the second one for a $2\theta = 8.54°$ corresponds to the main peak of a chromium oxide enriched in iron according to the ICDD n°035-1112 that we will refer to as $(Cr,Fe)_2O_3$. A Magnetite phase (ICDD n°071-6336) is also identified on the pattern for a $2\theta = 8.96°$. The presence of a magnetite phase enriched in chromium is also suspected with a main peak at $2\theta = 8.97°$. In Figure III.19 a), the peaks relative to $(Cr,Fe)_2O_3$ is of higher intensity. In Figure III.19 b) it could be seen that the intensity of the $(Cr,Fe)_2O_3$ peak increases, and a simultaneous growth of $(Fe,Cr)_2O_3$ peak is also observed. A hematite peak (ICCDD n°033-0664) at ($2\theta = 8.43°$) appears on the pattern. Figure III.19 c) underscored a change in the relative intensity of the iron chromium oxide. Indeed, the chromium rich phase $(Cr,Fe)_2O_3$ peak intensity is this time lower than the intensity of the peak relative to the iron rich phase $(Fe,Cr)_2O_3$.

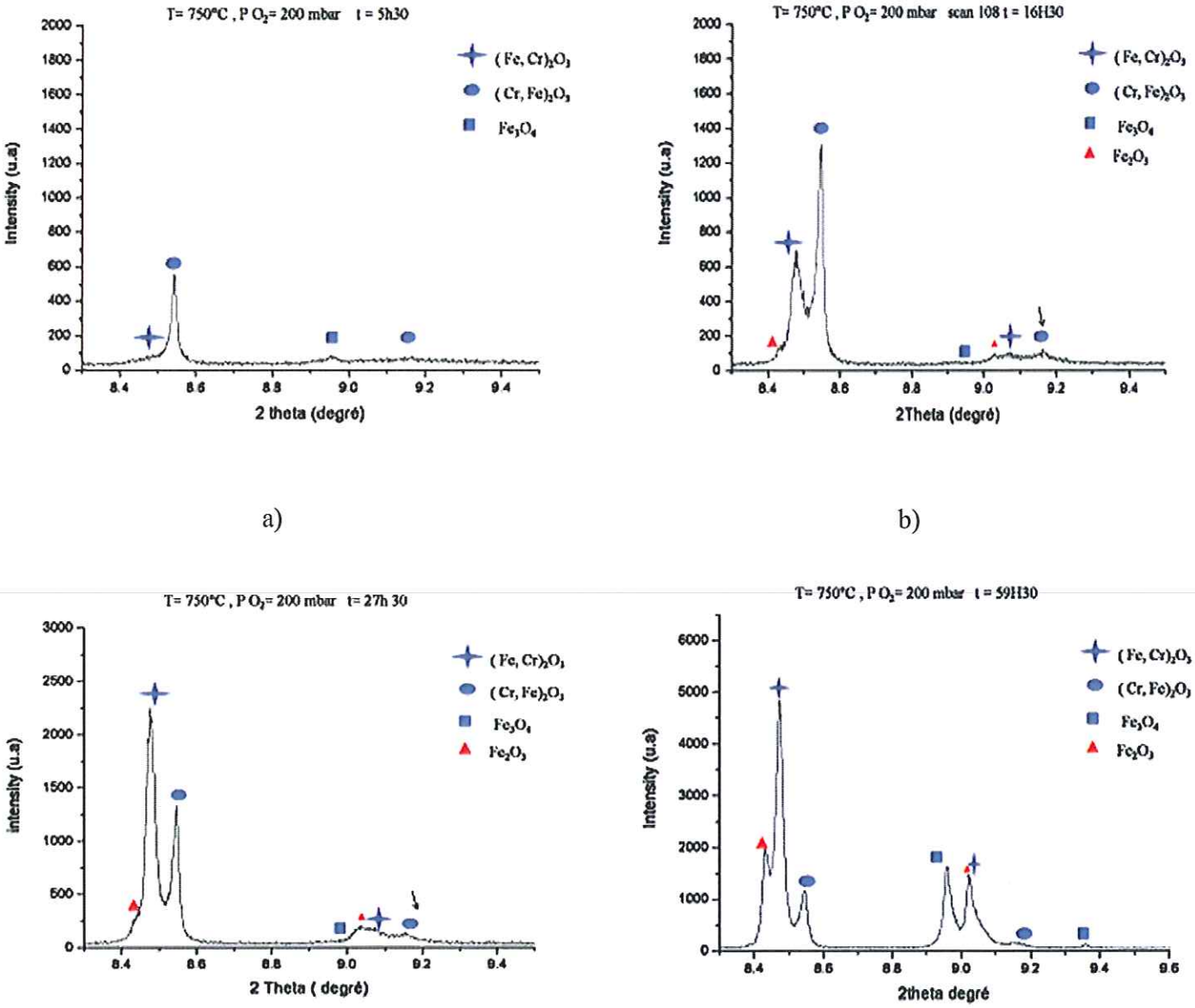

Figure III.19 : Synopsis of crystallites structures growth and evolution function of time exposure (t) on 9%Cr at 750°C in 200 mbar of O_2 for a) t= 5h30, b) t= 16h30 c) t= 27h30, d) t= 59h30.

After approximately 60 h the iron rich phases are predominant; indeed, $(Fe,Cr)_2O_3$ is the crystallite structure which displays the peak with the highest intensity. Moreover, a rapid growth of hematite and magnetite are also highlighted. This is characteristic of a catastrophic oxidation.

The intensity of peaks characteristics of the identified phases versus time are plotted in Figure III.. The evolution of these intensities brings information about both the kinetic of the

reaction and the diffusion phenomena occurring during the oxidation. Indeed, one could note that in Figure III.20 a), the intensity of the peak relative to $(Cr,Fe)_2O_3$, after a fast increase part during the ten first a hours, become constant or seems to diminish. In Figure III.20b) the intensity peak relative to the iron chromium oxide phase, rich in iron $(Fe,Cr)_2O_3$, starts to increase after 15 hours until the end of the experiment. Furthermore, the iron oxide Fe_2O_3 and Fe_3O_4 and the intensity of their peak characteristics (Figure III.20 c) d)) increase, following what one could call a linear regime after 40 hours. This could be linked to the breakaway phenomenon registered on the kinetic curves.

As an interpretation of such evolution, the diffusion of chromium from the bulk to surface should be considered. Indeed, at the beginning of the oxidation, it seems that chromium diffusion is ensured and thus the formation of a temporary protective chromium rich oxide $(Cr, Fe)_2O_3$ is obtained. When the underlying substrate is depleted in chromium, formation of $(Fe,Cr)_2O_3$ occurs. This is closely followed by the formation of a porous pure iron oxide, such as hematite and magnetite.

To clearly understand the mechanism leading to the formation of such oxide scale, isotopic labeling (O^{16}/O^{18}) followed by SIMS analyses were performed.

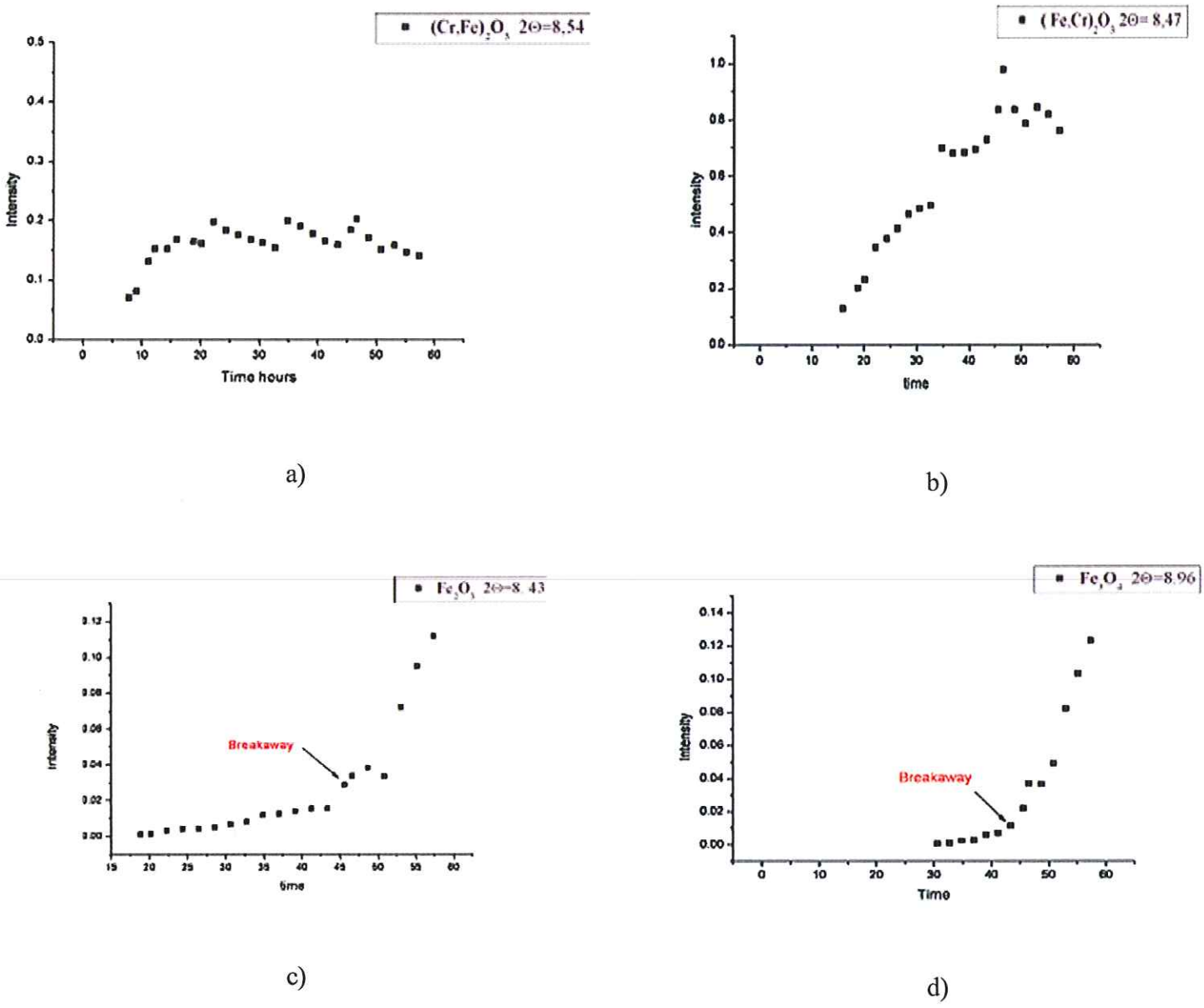

Figure III.20 Intensity versus time for the main crystallite phases detected by high resolution XRD a) $(Cr,Fe)_2O_3$, b) $(Fe,Cr)_2O_3$, C) Fe_2O_3, d) Fe_3O_4.

Synthesis: ***Synchroton ESRF high resolution diffraction.***
Progressive growth of oxide scale is followed in situ. Progressive enrichment of in iron of the scale function of time is observed from $(Cr,Fe)_2O_3$ to $(Fe,Cr)_2O_3$. For longer exposure time, Fe_3O_4 and Fe_2O_3 are the faster growing phases.

IIII.3.6 Isotopic labeling assessment tool of species diffusion for thermally grown oxide scale.

The isotopic labeling O^{16}/O^{18} associated to SIMS analyses is a technical procedure developed at the University of Burgundy to underline the ions diffusion phenomena which can occur during high temperature oxidation in a reactive atmosphere. 9%Cr sample was thus oxidized at 650°C for 100h in O^{16}/O^{18} in condition as described in chapter II paragraph II.4, aiming to grow similar oxide thickness in both atmospheres. SIMS analyses were subsequently carried out the obtained samples. Figure III.21 below displays the SIMS analyses obtained results.

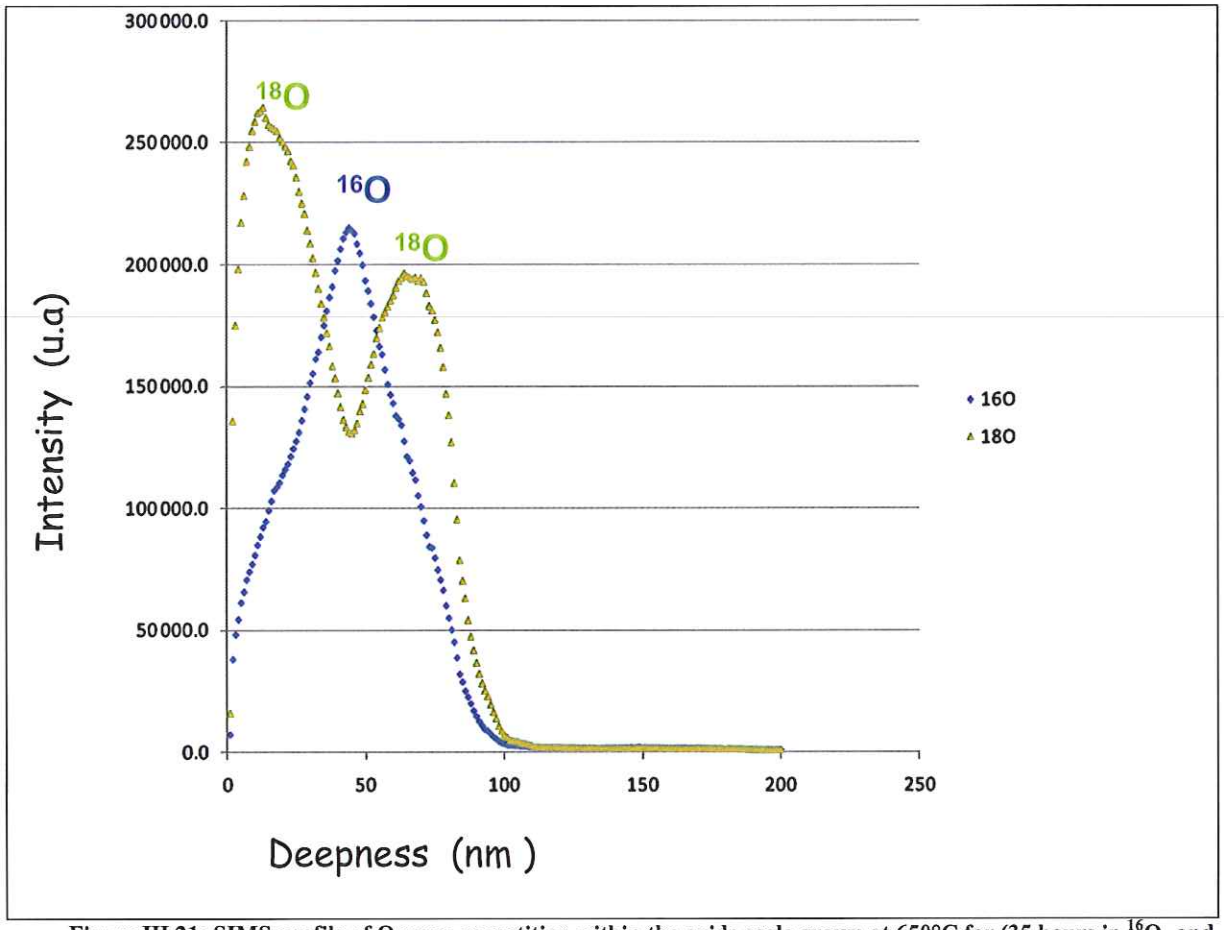

Figure III.21: SIMS profile of Oxygen repartition within the oxide scale grown at 650°C for (35 hours in $^{16}O_2$ and 65 hours $^{18}O_2$)

Presence of Oxygen ^{18}O has been detected in both the outer and inner oxide layer whereas ^{16}O was detected in the middle part of the oxide layer. This Oxygen profile within the oxide scale, according to Chevalier's study [4], is characteristic of an oxidation mechanism ruled by both outwards cations diffusion, and inwards anions diffusion. Indeed the presence of oxide formed mainly with ^{18}O in the inner part of the scale highlights the diffusion of $^{18}O^{2-}$ species through the existing layer to react at the metal/oxide interface and to form $(Cr,Fe)_2O_3$. On the other hand formation of the outer layer also mainly containing ^{18}O confirms the existence of a

cationic (Fe cation) diffusion phenomenon which nourishes the reaction at the oxide/gas interface to form Fe_2O_3.

Synthesis: ***Isotopic labelling***
Outer Cation mainly Fe) diffusion phenomenon to react at the gas/oxide interface and to form Fe_2O_3 has been assessed. Inner Oxygen diffusion phenomenon is also observed, and by reacting at the metal/oxide interface, is responsible for the formation of an inner layer enriched in chromium.

III.4 Discussion and general summary for high temperature corrosion in laboratory air

In this chapter, the high temperature oxidation process of 9% chromium steel was studied. As a general trend, when the temperature and exposition time in oxidizing environment increase, mass gain of the specimens increases. A lot of information concerning the oxide layer grown on the substrate at 650°C was brought by different characterization tools. When SEM coupled with EDX or XRD analyses at low glancing angles show their limit in the identification of the oxide developed in those severe conditions, the photoelectrochemistry spectroscopy highlights, the formation of chromium rich phases at 650°C after 100h of oxidation.

However, the substrate is not a chromia forming alloy and as suspected by Piron Abellan et al. [30], it is more likely a temporary protective chromium iron oxide mixture which is formed in the first step of the oxidation process. The in situ and ex situ XPS agree with this assumption. They show that both iron oxide and chromium oxide are formed for short time exposure at 650°C. They also evidence the presence of Cr (VI) within the formed oxide. This could suggest that a non continuous layer of mixed spinel is formed, as proposed by Wright and Bénard [21,22], or other solid solutions of chromium in iron oxide. In that case, at 650°C and at this pressure, Cr supply in the oxide scale by diffusion in the steel is not sufficiently fast. Therefore, a spinel with considerable chromium defects could be formed and then explained the Cr (VI) detection. As a matter of fact, oxide growth is governed by the Cr diffusion in the base alloy, as well as in the oxide scale. High resolution diffraction results are in favour of such theory. Indeed, they show the evolution of the formed layer from a chromium rich oxide doped by iron cation $(Cr, Fe)_2O_3$ to a iron rich oxide doped by chromium $(Fe,Cr)_2O_3$.

When fitting the magnetite peak present from the outset of the reaction, using Topas©4.2 software, it is possible to identify a $(Fe,Cr)_3O_4$ (2θ= 8,97; ICDD n° 075-3312). This crystallite structure could during the first instant show a lack of chromium and could be written as follow (Fe (II) Cr (VI)) O_4 or $[Fe(II)Cr(III)V_{Cr}''']O_4$.

High resolution diffraction patterns stressed also that when chromium diffusion from the substrate to the surface is stopped, or when there is a chromium depletion, both magnetite and hematite grow on the samples.

For exposure time higher than 100h at 650°C or for high temperatures, the scale is mainly composed of iron oxide: magnetite in the inner part and hematite in the outer part of the scale. These observations were confirmed by both Raman and TEM analyses and are in agreement with what was reported in the literature [31-35].Figure III.22 is a schematic of what could be proposed as the oxide scale structure.

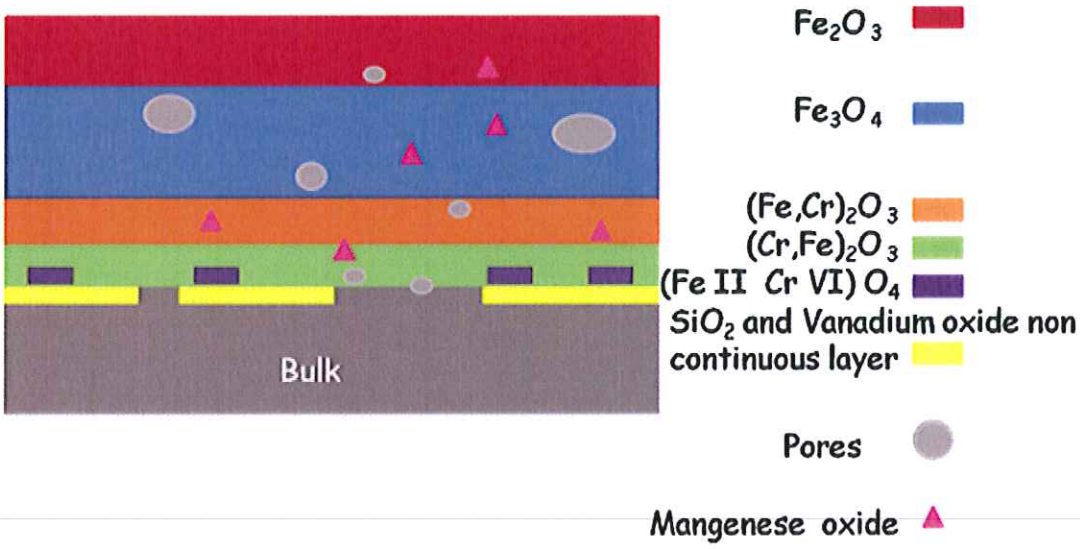

Figure III.22: Oxide scale structure of 9%Cr steel oxidized in dry atmosphere at 650°C

The manganese found in the scale, could form spinel oxides with chromium such as $Mn_{1.5}Cr_{1.5}O_4$ in the inner layer and form iron manganese oxide spinel, such as $MnFe_2O_4$, in the outer layer where the chromium concentration is lower. At the metal/oxide interface vanadium and silicon oxide are detected. Silicon could help to the scale adherence whereas vanadium is known to be detrimental to high temperature corrosion resistance of steel causing it to form an oxide (V_2O_5) which is volatile around 630°C .

Formation of the oxide layer could be linked to a mix diffusion phenomenon. Indeed both metal cations outwards diffusion and oxygen anions inward diffusion during the oxidation process were assessed. Reactions between the different species are supposed to take place at the metal/oxide and the oxide/gas interfaces.

REFERENCES

[1] B. Pierragi, Oxidation of Metals, 27 (1987) 177.
[2] S. Chevalier, C. Valot, G. Bonnet, J. C. Colson, J. P. Larpin, Material Science and Engineering, A 343 (2003) 257
[3] G. Cabouro, G. Caboche, S. Chevalier, P. Piccardo, Journal of Power sources, 156 (2006) 39.
[4]Sébastien Chevalier: Traitements de surface et nouveaux matériaux : Quelles solutions pour lutter contre la dégradation des matériaux à haute température, Editions Universitaires de Dijon, collection Sciences, Dijon (2007).
[5] R. Benadoud, P. Bouvier, J.P. Petit, Y. Wouters and A. Galerie, Journal of Nuclear Materials, 360 (2007) 151.
[6] S. Henry, J. Mougin , Y. Wouters, J.P. Petit and A. Galerie, Materials at High Temperatures,17 (2000) 231.
[7] Y. Wouters, A. Galerie, P. Bouvier, M. Mermoux and J.P. Petit, Materials at High Temperatures, 22 (2005) 315.
[8] Y. Wouters, A. Galerie and J.P Petit, Materials Science Forum, 598 (2008) 1181.
[9] D. Brion, Applied Surface Science, 5 (1980) 133.
[10] E. Matsubara, H. Inoue, M. Oku, M. Saito, S. Suzuki, T. Kosaka, Y. Waseda, Scripta Materiala, 36 (1997) 841.
[11] C.R Brundle, T.J Chuang, K Wandelt, Surface Science, 68 (1977) 459.
[12] C.R. Brundle, Surface Science,66 (1977) 581
[13] M. Muhler, R. Schlögl, G. Ertl, Journal of Catalysis, 138 (1992) 413.
[14] M. Muhler, J. Schütze, M. Wesemann, T. Rayment, A. Dent, R. Schlögl, G. Ertl, Journal of Catalysis, 126 (1990) 339
[15] T.L. Barr, Journal of Physics and Chemistry, 82 (1978) 801.
[16] S. Ciampi, V. Di Castro, Surface Science, 333 (1995) 294.
[17] D. Briggs, M.P. Seah, John Willey & sons. Vol. 1, second edition 1993.
[18] B. Stypula and J. Stoch, Corrosion Science, 36 (1994) 2159.
[19] C. Donik, A. Kocijan, D. Mandrino, I. Paulin, M. Jenko, B. Pihlar, Applied Surface Science, 255 (2009) 7056.
[20] P. J. Ennis, W. J. Quadakkers, International Journal of Pressure Vessels and Piping, 84 (2007) 75
[21] I. G. Wright, Metal handbook, Corrosion 9th edition , ASM Metals Park, OH (1987) 97.
[22] J. Bénard, Gauthier-Villard Edt., Paris (1964).
[23] S. Sroda, D. Baxter and M. Arponen, Materials and Corrosion, 56 (2005) 791.
[24] K. Berreth, K. Maile and A. Lyutovich, Materials and Corrosion, 56 (2005) 916.
[25] A. M. Huntz, V. Bague, G. Beauple, C. Haut, C. Severac, P. Lecour, X. Longaygue and F. Ropital, Applied Surface Science, 207 (2003) 255.
[26] J. M. Brossard, M. P. Hierro, J. A. Trilleros, M. C. Carpintero, L. Sanchez, F. J. Bolivar and F.J. Perez, Surface and Coatings Technology, 201 (2007) 5743.
[27] H. Nickel, Y. Wouters, M. Thiele and W. J. Quadakkers, Fresenius' Journal of Analytical Chemistry, 361 (1998) 540.
[28] J. Zurek, E. Wessel, L. Niewolak, F. Schmitz, T. U. Kern, L. Singheiser and W. J.Quadakkers, Corrosion Science, 46 (2004) 2301.
[29] J. Purmensky, V. Foldyna and Z. Kubon, Key Engineering Materials, 171 (2000) 419.
[30] J. Piron Abellan, T. Olszewski, G. H. Meier, L. Singheiser, W. J Quadakkers, International Journal of Materials Research, 101 (2010) 2.

[31] M. Schütze , D. Renusch, M. Schorr, Corrosion Engineering, Science and Technology, 39 (2004) 157.
[32] J.P.T.Vossen, P. Gawenda, K. Rahts , M. Röhrig , M. Schorr, M. Schütze, Materials at High Temperatures, 14 (1997) 387
[33] H.J. Grabke, E.M. Müller-Lorenz, B. Eltester, M. Lucas, D. Monceau, Steel research International, 68 (1997) 179
[34] F. J. Perez and S. I. Castaneda, Surface and Coatings Technology, 201 (2007) 6239.
[35] J. Ehlers, D. J. Young, E. J. Smaardijk, A. K. Tyagi, H. J. Penkalla, L. Singheiser and W. J. Quadakkers, Corrosion Science, 48 (2006) 3428.

IV. Effect of water vapour and steam.

The effects of water vapour or steam on steel behavior at high temperature are of great interest. In 1988 Koftad [1] wrote:" It is well known that most technical steels oxidize faster in water vapour or in air or combustion gases containing water vapour, than in dry oxygen. The reasons for this are poorly understood". Since then, several works [2-6] have been done on the possible detrimental effects of wet atmosphere on steels at high temperature, but the mechanisms responsible for the increase of the oxidation rate are still not clear. In this chapter, we will focus on the behavior of 9%Cr steel in two different wet environments: "pure steam" with a pressure of 2.10^{-2} bar and air enriched with 12% vol. of water vapour at atmospheric pressure.

IV.1 Kinetic study and scale characterization

IV.1.1 Effect of air enriched with 12%vol. of water vapour

Isothermal tests were performed on samples in air enriched with 12% vol. of water vapour for 100h at 600°C, 650°C, 700°C and 750°C under atmospheric pressure using the experimental setup presented in Chapter II (paragraph II.22). The samples were weighted prior to and after the oxidizing tests. Figure IV.1 compares mass gains obtained in wet atmosphere to the ones obtained in laboratory air in similar conditions.

Table IV.1 lists the final mass gain registered for the different experiments. Higher mass gain is observed in the case of samples oxidized in air enriched with 12%vol. of water vapour at 600°C, 650°C and 700°C. The maximum weight variation is observed when the temperature reaches 700°C. At 750°C, lower mass gain is observed in wet atmosphere than what was registered in laboratory air.

Similar behavior was identified by Nickel et al. [7] in their study on low chromium steel. Indeed, they remarked a bell shape relationship between mass gain and temperature when the oxidation occurred in wet condition.

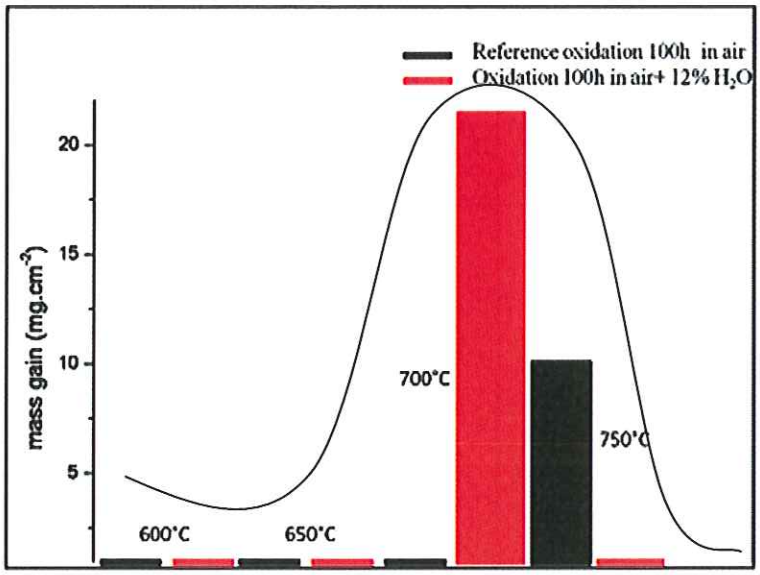

a)

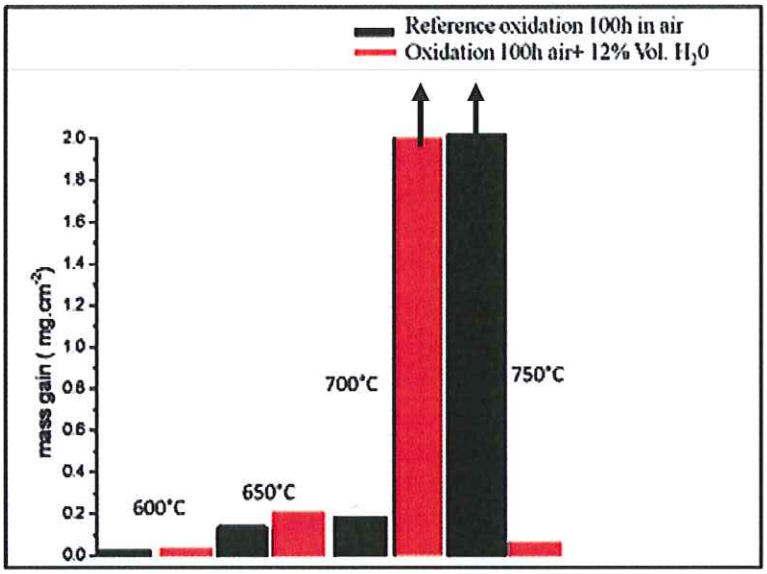

b)

Figure IV.1: a) zoom out, b) zoom in of mass gain obtained after oxidation for 100 h in air enriched with 12%vol. water vapour compared to mass gain obtained after oxidation for 100 h in laboratory air.

Temperature (°C)	Mass gain (mg.cm^{-2})
600	0.01 (± 5x10^{-4})
650	0.2 (± 9x10^{-3})
700	21.1 (± 1.1)
750	0.09 (± 7x10^{-3})

Table IV.1: Mass gain registered after oxidation for 100h in air enriched with 12%vol. water vapour.

Changes in the activity of elements such as Cr when increasing the temperature could play an important part in the explanation of such phenomena. When increasing the temperature diffusion of Cr from the bulk to the surface is accelerated and could help the formation of a temporary protective layer. One can suppose that for longer time exposure in water vapour containing environment at 750°C, important mass gain could be also observed.

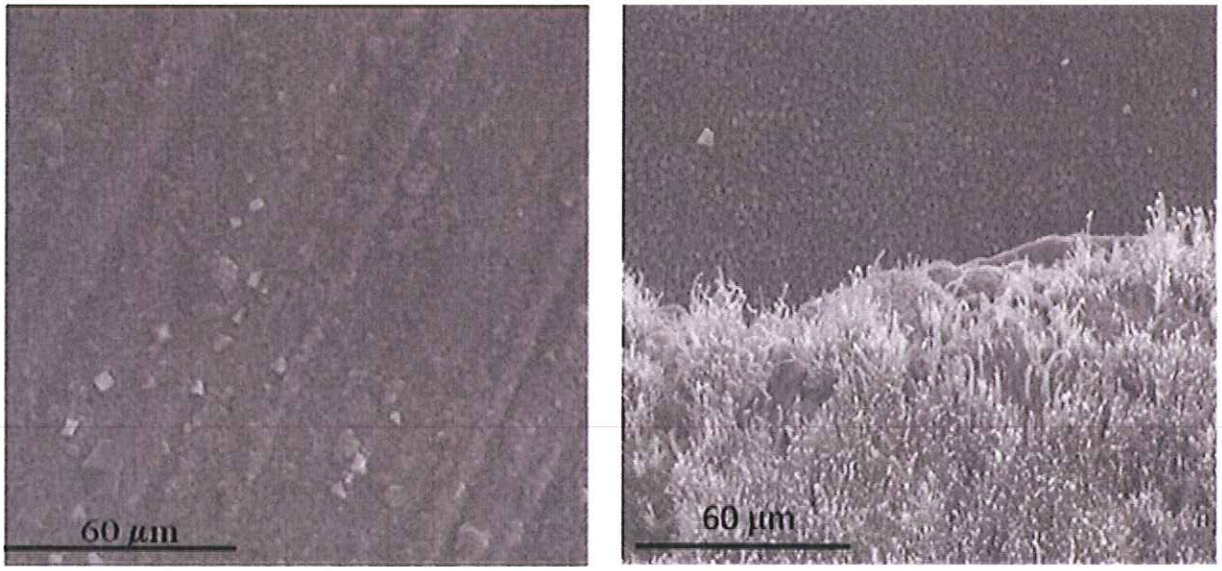

a) b)

Figure IV.2: SEM micrographs after oxidation under water vapour containing environment at a) 650°C and b) 700°C.

Figure IV.2 presents micrographs of the surface of the samples after oxidation. For sample oxidized at 650°C for 100h in air +12% vol H_2O, scratches due to the polishing steps are still visible. Following those scratches, nodules of chromium – iron oxide are observed according to the EDX results. Spalled areas can be seen on the sample oxidized at 700°C for 100h in air + 12 % vol. H_2O. The scales seem to be composed of two distinct layers. A first one, where iron oxides shaped in needles are identified. Beneath this scale, another oxide layer composed of manganese, chromium and iron is highlighted. Those micrographs give an idea of the thickness of the oxide scales. The scale characterized for the sample oxidized at 700°C looks thicker than the one observed at 650°C.

IV.1.2 Effect of Steam.

The XPS oxidation chamber described in chapter II paragraph II.3.5 was used for a 100h ageing test at 650°C in steam on a 9% Cr steel sample. Important mass gain was

registered $\Delta m/A = 8.5$ mg.cm^{-2}. This value is higher than that observed at the same temperature in dry air or in air enriched with 12% vol of water vapour.

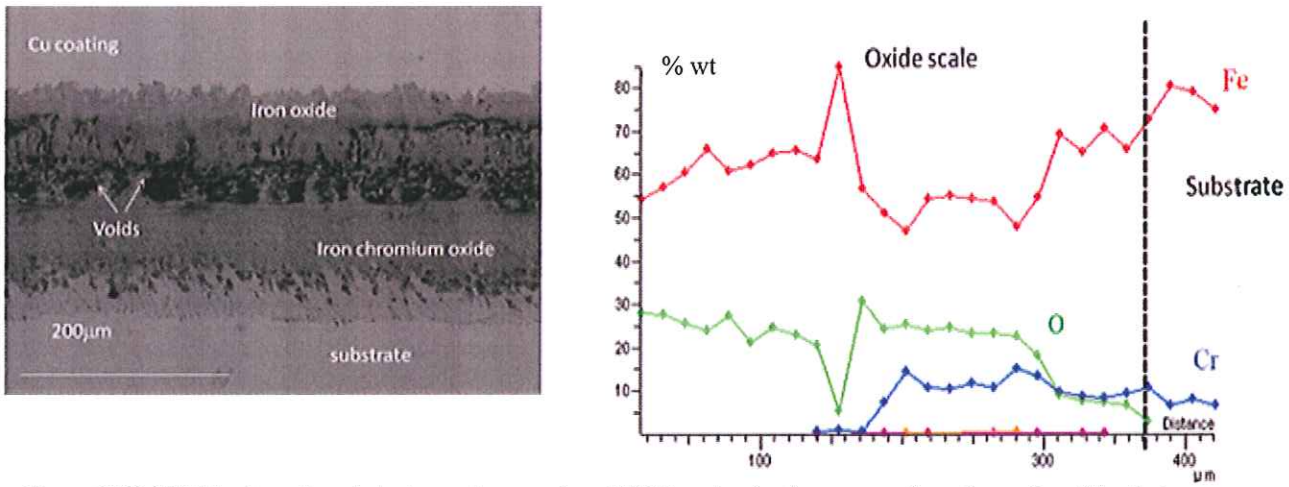

Figure IV.3: SEM back scattered electron micrograph and EDX analaysis of a cross section of sample oxidized at 650°C for 100h in steam.

Figure IV.3 presents the SEM cross section micrograph and the EDX analyses relative to this sample. A thick oxide scale is observed in Figure IV.3 (380 µm) with important closed pores and cracks within the scale and at the interface metal oxide. The EDX analyses show a layer mainly composed of iron oxide at the top surface over another layer in which chromium oxide and iron oxide are detected. This structure is similar to what is reported in the literature for P91 oxidized in wet atmosphere [8-9].

Within the objective to understand the oxide layer growth mechanism on 9%Cr steel occurring in this environment, short term oxidation reaction followed by XPS analyses were performed.

IV.2 In situ XPS analysis results and steam effect

In-situ XPS analyses were then performed on samples oxidized at 600°C in steam at atmospheric pressure for different exposure time to highlight the differences with dry atmosphere. In Figure IV.4 the results obtained for samples oxidized for 5 min, 30 min, 1 hour in steam are superposed. In all cases, XPS Fe 2p signals exhibit two important peaks, one at 711eV and another around 724 eV corresponding to the $2p_{3/2}$ and $2p_{1/2}$ of iron oxide. When focusing on the $2p_{3/2}$ peak reconstruction, it is possible to characterize the level of oxidation Fe (II) and Fe (III) (Figure IV.5). Moreover, an evolution in intensity of those contributions is observed, underlining that with increasing time exposure, Fe (II) species take over Fe(III) species within the scale, in those oxidizing conditions.

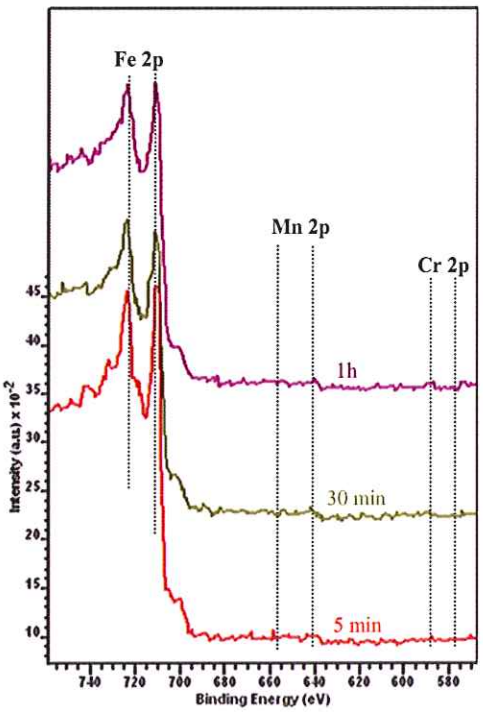

Figure IV.4: XPS spectra registered on samples oxidized in situ at 600°C for 5 min, 30 min, 1hour in steam.

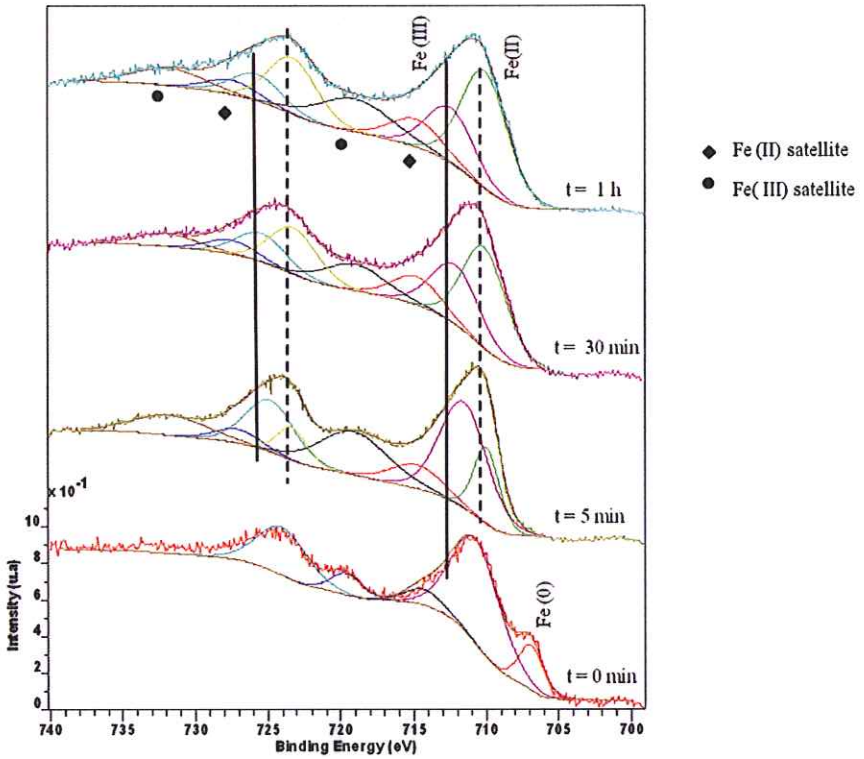

Figure IV.5: XPS spectra showing Fe 2p signals after 0 min, 5 min, 30 min, 1h of oxidation in steam at 600°C.

This could lead to think that for long term exposure, mainly magnetite is formed. To verify this hypothesis, XRD analyses at low glancing angles (θ=1°) were performed on samples

oxidized for 5 min and 1 hour in steam. Indeed, in Figure IV.6, the corresponding XRD patterns are plotted. For the 5 min oxidized sample (Figure IV.6 a)) a thin oxide scale is detected, iron peaks corresponding to the substrate are still visible, hematite and magnetite crystalline structure were highlighted. For the one hour oxidized sample, (Figure IV.6 b)), only magnetite is identified; no signal corresponding to the substrate was registered.

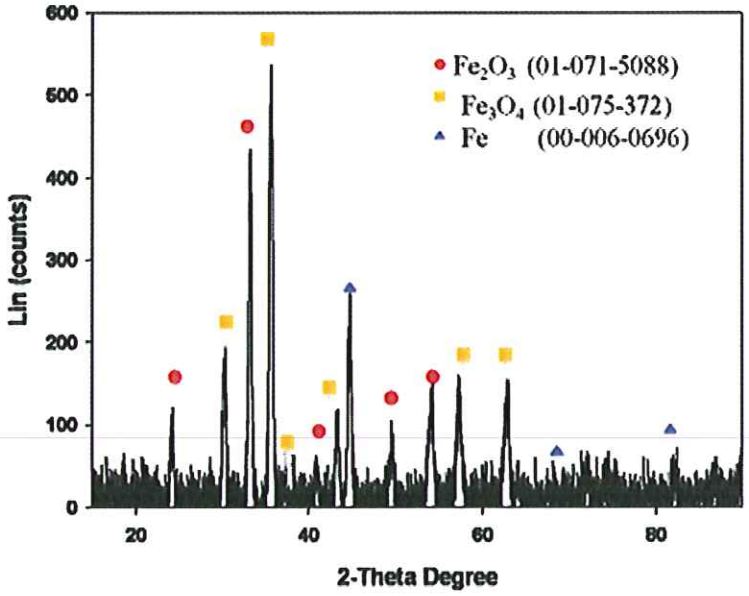

a)

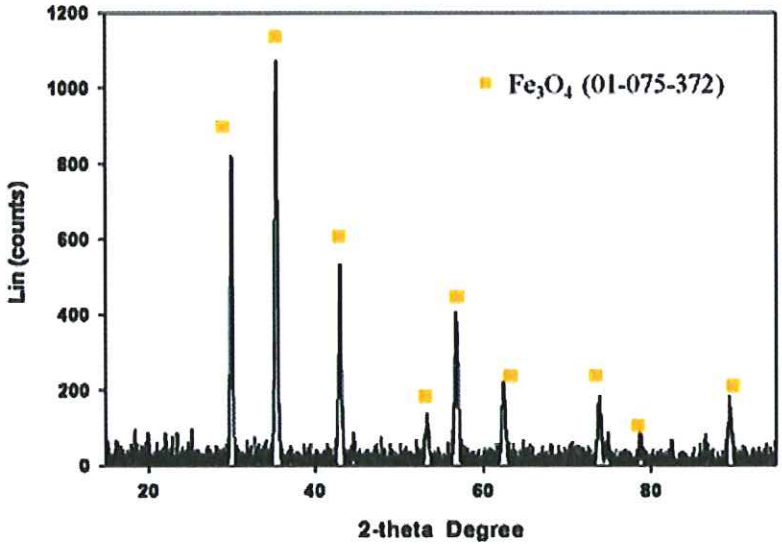

b)

Figure IV.6: XRD patterns for samples oxidized at 600°C for a) 5 min and b)1 hour in steam.

One could state that thicker oxide scale grew on the coupons after oxidation at 600°C for 1hour in steam compared to that obtained in dry air.

Furthermore, no signal was registered for Cr 2p, as shown in Figure IV.7. The same observation could be made for Mn 2p signal. This is the main difference with the in situ XPS results obtained in dry air.

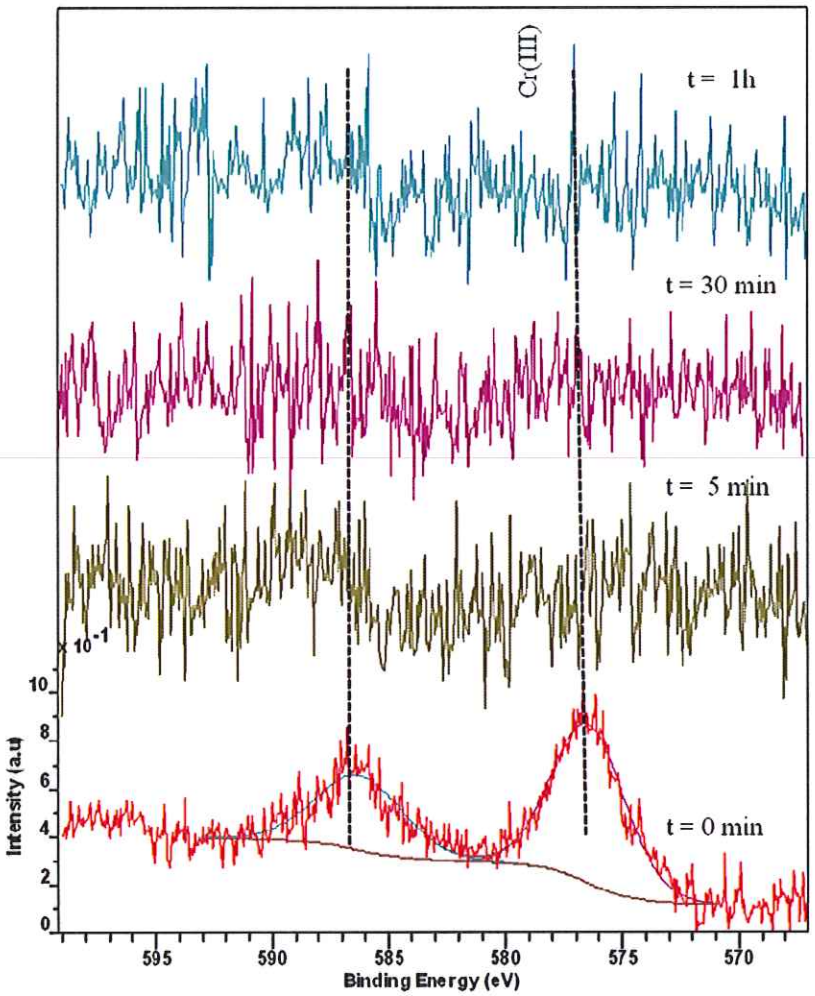

Figure IV.7: XPS spectra showing Cr 2p signals after 0 min, 5 min, 30 min , 1 h of oxidation in steam.

Absence of Cr 2p signal on the XPS spectra could be explained either by the fact that there is no chromium oxide formation, or by the formation of chromium hydroxide or oxohydroxide volatile species [10] which could lead to chromium depletion in the material during the oxidation process. Another hypothesis could be proposed. Indeed, the formation of a thick oxide scale could also be an explanation for the absence of Cr 2p signal on the spectra corresponding to exposure in steam at high temperature. This high oxidation rate could be linked to a catalytic effect of water. Therefore, the XPS tool, giving information only on the

first nanometers of the oxide layer, could not give access to the inner layer, where chromium oxide may exist. Nickel et al. [7] developed a theory according to which the nature of the defects in the scale could be changed by water vapour and, thus, the diffusion phenomenon at the origin of the oxidation process increases the reaction kinetics.

Henry et al. [11] stated that hydroxide species, OH^-, could substitute oxygen anions in the layer and easily diffuse in the scale because of its effective electrical charge and its size (0.095 nm OH^- for 0.140 nm for O^{2-}). If the H_2O/O_2 ratio is high, the kinetic of the oxidation process increases.

The hypothesis of a thicker oxide scale formed on the 9%Cr steel exposed in pure steam could be consolidated by SEM surface and cross section analyses.

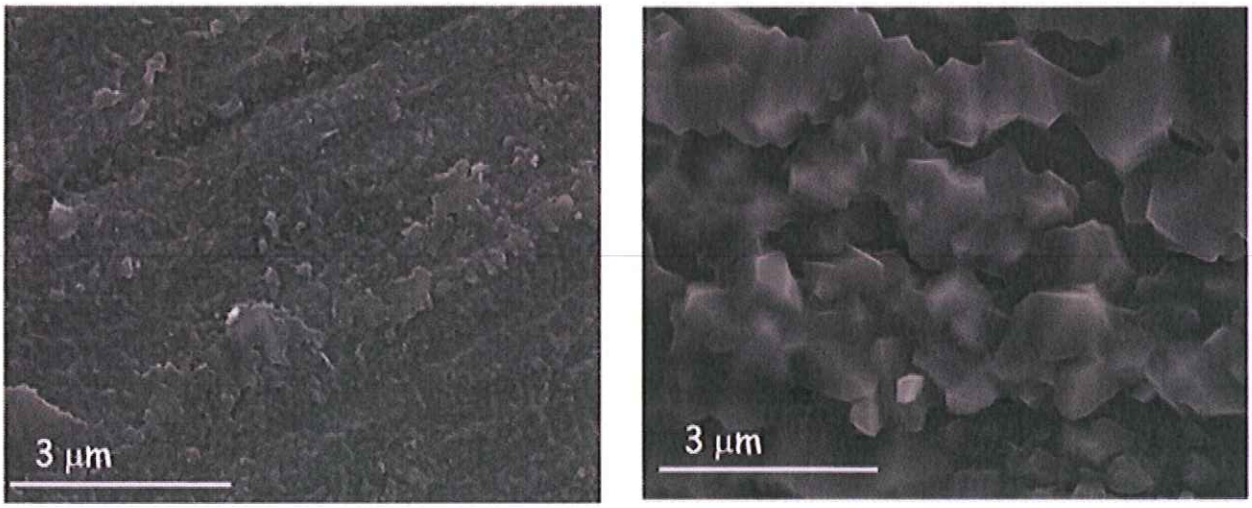

a) b)

Figure IV.8: SEM surface micrographs: a) in situ oxidized sample for 30 min at 600°C in laboratory air; b) in situ oxidized sample for 30 min at 600°C in steam.

In Figure IV.8 a), polishing marks due to the sample preparation are still visible. The oxide layer is composed of small spherical nodules made of iron, chromium, manganese according to EDX analyses. For the same exposure time and temperature in steam, Figure IV.8 b) displays larger oxide crystallites. The scratches due to the polishing steps are not visible. The oxide scale seems thicker for the oxidation in steam than in air.

Moreover, a 24 hours oxidation test using the XPS oxidation chamber was also performed in steam at 2.10^{-2} bar total pressure. Figure IV.9 presents a cross section of the obtained corrosion products and the corresponding EDX analyses.

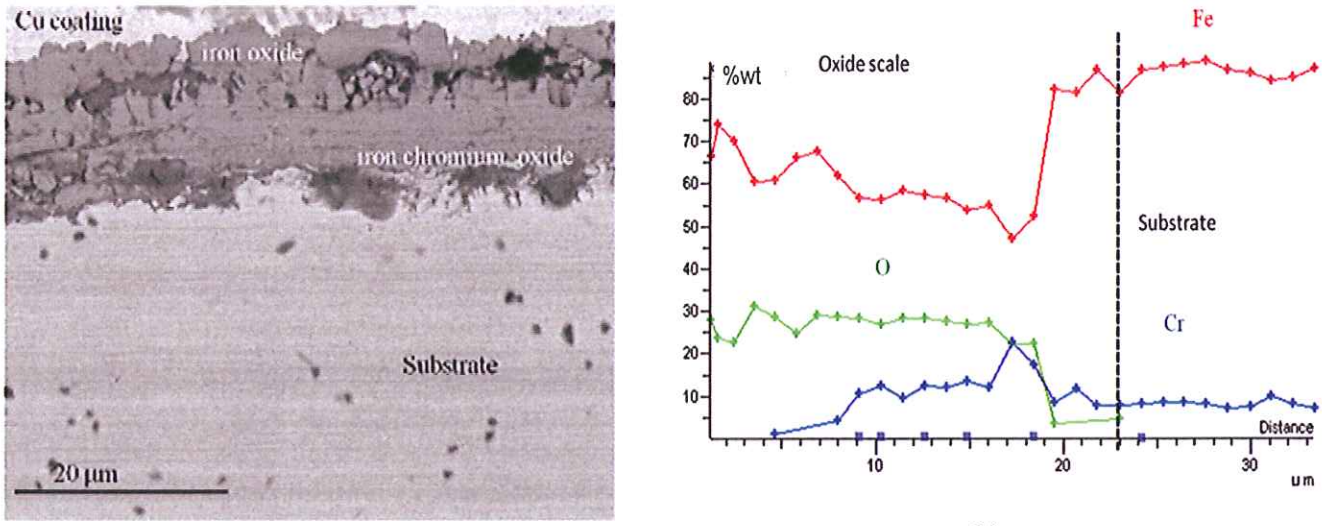

a) b)

Figure IV.9 : a) SEM cross section micrograph and b) EDX analysis of samples oxidized for 24 h at 600°C in steam

An oxide scale of around 25 µm thick is observed in Figure IV.9 a). Pores are clearly visible within the oxide layer. The EDX analyses help to distinguish two different layers in the oxide scale (Figure IV.9 b)). Indeed, a first layer of 5 micrometers in thickness at the top surface where only iron oxide is detected and beneath it, a second layer composed of iron oxide and chromium oxide is also identified. It confirms the hypothesis according to which chromium oxides are formed in the inner part of a thick oxide scale and that the limitation on the XPS technique is responsible for the results obtained on the spectra shown in Figure IV.7

The top surface of this sample was also investigated by XRD. The results give a clear idea of the iron oxide crystallographic structure.

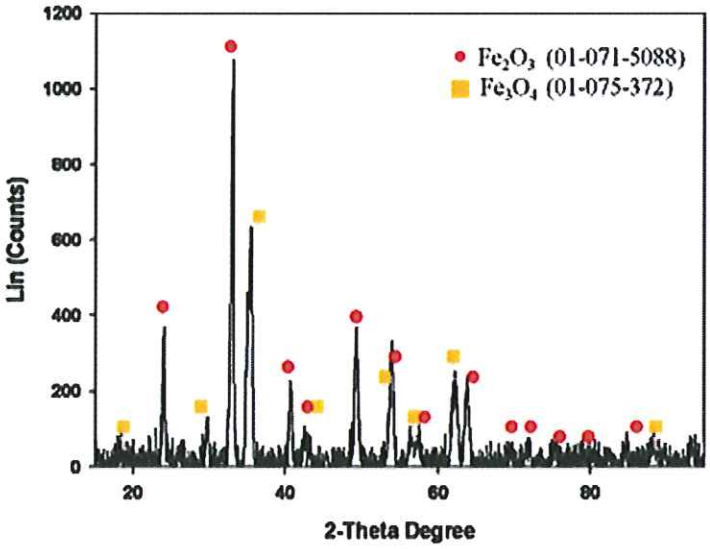

Figure IV.10: XRD analysis of sample oxidized for 24 hours in pure steam at 600°C.

Magnetite and hematite were highlighted on the XRD pattern in Figure IV.10, whereas only magnetite was detected after one hour of oxidation in similar condition (Figure IV.6 b). This could mean that the final oxide scale is composed of non protective chromium iron oxide overlaid by a magnetite scale. On the top of these two sub layers, grows a hematite rich scale.

IV.3 Investigation of corrosion products by TEM

Oxidation experiment was performed on 9% Cr steel at 650°C for 100h in steam with a pressure of 2.10^{-2} bar using the XPS oxidation chamber described previously. A thin film of a cross section of this corrosion product was prepared by FIB prior to observation by TEM. Figure IV.3 evidenced that a thick oxide scale (more than 300 µm) was formed and shows important closed pore density within the scale. The thin foil preparation, in that case requires some cautiousness. The substrate in that case has not been reached. Due the complexity of those steps and the presence of holes in the layer, the prepared film was investigated in two goes times.

Figure IV.11 presents the two different parts of FIB cross section. On the left, is represented the bottom part of the scale is represented and on the right the top part of the scale.

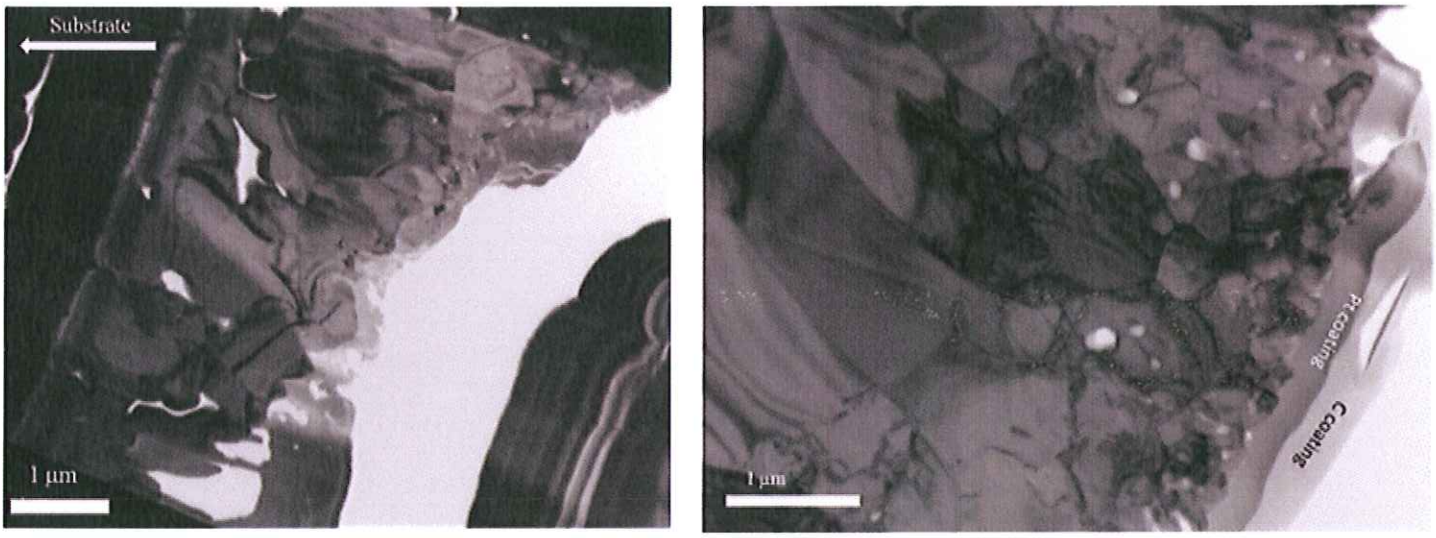

Figure IV.11: FIB cross section of 9%Cr steel oxidized for 100 h in steam. Bottom part of the sample (left micrograph). Top part of the sample (right micrograph).

Big oxide grains are observed on the bottom part of the thin film corresponding to the inner oxide layer. Pores are clearly visible between the grains. The top part of the foil on the other hand is composed of smaller oxide grains. EDX analyses and selected area diffraction on both part of the samples give the same results. The EDX semi quantitative analyses results are listed in Table IV.2

Elements	% weight	% atomic
O	35.6	65.8
Cr	0.6	0.4
Fe	63.8	33.8

Table IV.2 : EDX semi quantitative analysis on FIB cross section after oxidation for 100h at 650°C in steam.

According to the EDX results, the Fe/O atomic ratio is close to the one corresponding to hematite. The corundum structure is confirmed by selected area diffraction pattern in Figure IV.12.

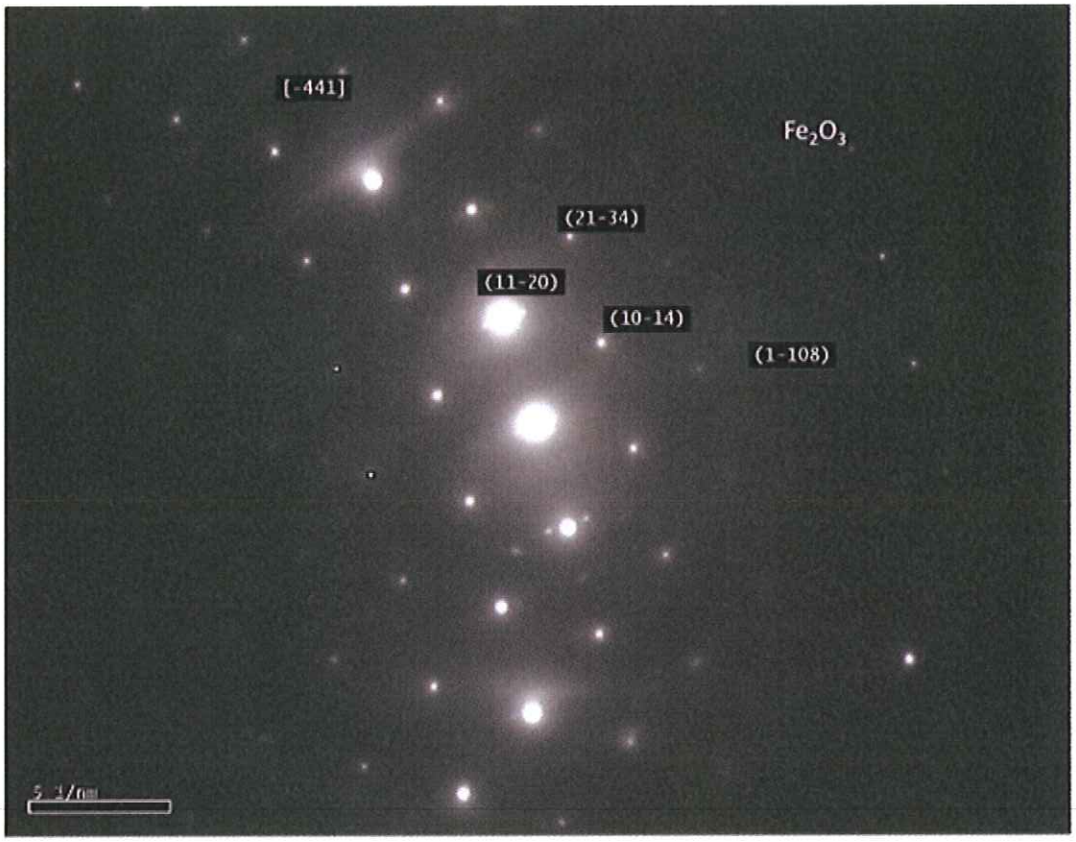

Figure IV.12: Selected area diffraction pattern for FIB cross section of sample oxidized for 100 h at 650°C in steam.

The TEM investigation of the oxide scale microstructure confirms what was highlighted by XRD patterns (Figure IV.10). Oxidation in steam at 650°C in this pressure condition , clearly evidences hematite in the outer most layer of the oxide scale thermally grown on 9%Cr steel grade.

IV.4 Discussion and general summary for oxidation at high temperature in steam and water vapour.

As a general discussion, the steam oxidation resistance of 9%chromium steels depends mainly on the chromium content and to a lesser extent on the presence of minor alloying elements, and on the water vapour content in the environment.

Discontinuous kinetics data registered in air enriched with 12% Vol. water vapour and plotted in Figure IV.1 exhibit an anomalous temperature dependence of the oxidation behaviour in the temperature range 600-750°C. The maximum oxidation rates may be observed at lower temperatures (650 or 700°C) than that observed in laboratory air. This was also observed by Nickel and Quadakkers [7] during their work on high temperature corrosion resistance of 9%Cr steel in Ar enriched in oxygen and water vapour within the same temperature range. The bell shape relationship observed between mass gain and temperature could be due to Cr activity and diffusion process which change when increasing the temperature. Indeed, one can suppose that there is a transition in chromium diffusion from the bulk to the top surface between 700°C and 750°C. Therefore, at 750°C a temporary protective chromium rich scale could be formed and explained the difference in total mass gain after 100 hours exposure in the same wet environment.

Initially, all studied samples tend to form a Cr-rich oxide. Nevertheless, oxidation of low chromium steels is frequently observed to produce iron rich scales containing closed pores and internal fissures. 9%Cr steels are known for forming an iron chromium spinel and magnetite in particular at 650°C in water vapour containing gas [8, 12].

In this chapter, XRD coupled with in-situ XPS and TEM experiments gave a clear idea of the composition of the oxide scale. The important mass gain observed could be associated with the formation of an outer hematite layer and a porous inner scale mainly consisting of Fe_3O_4 and more or less chromium rich oxide as $(Fe,Cr)_3O_4$. Figure IV.13 is a schematic of the proposed oxide scale composition. The sequence of apparition of those different layers (first the spinel, then the magnetite and the hematite) is in total agreement with what is reported by Quadakers et al. [13].

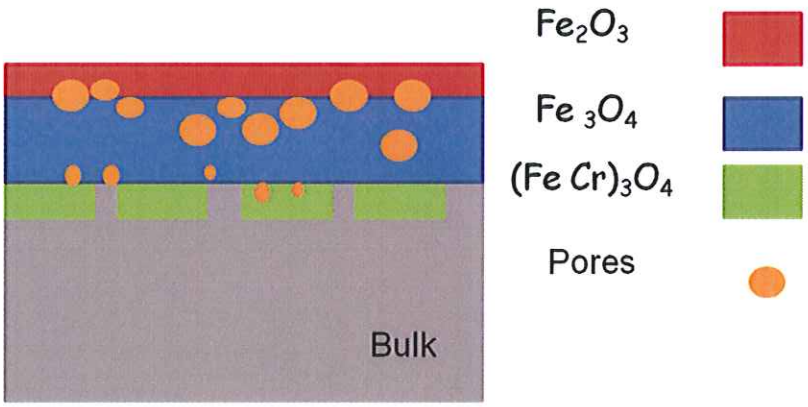

Figure IV.13 : Schematic of the composition of the oxide layer thermally grown in wet atmosphere on 9%Cr steel samples at 650°C.

According to the literature [14], scale growth could be determined by the surface reaction at the gas/oxide interface. The water molecule is very stable with respect to its dissociation ($\Delta G°$= -530 kJ.mol^{-1} at 650°C). Therefore the decomposition process could be the rate limiting step in the reaction involving a metal and pure steam and it has been observed that in many cases oxidation rates in pure steam are lower than in O_2 [15].

Nevertheless in our cases important mass gain is observed during oxidation at 650°C in pure steam (2.10^{-2} bar total pressure). Indeed, after 100h of oxidation a thick oxide scale (300 µm thick) grew on the 9%Cr steel samples. This phenomenon was observed for the growth of oxide scale where the diffusion of species is mainly anionic. According to Galerie's work [11, 16] the hydroxide species, $OH,^-$ could substitute oxygen anions in the layer and easily diffuse in the scale because of its effective electrical charge and its size (0.095 nm OH^- for 0.140 nm for O^{2-}). As a consequence, if the ratio H_2O/O_2 is high, oxidation rate increases.

In many cases, the scale growth mechanisms intrinsically lead to the formation of in-scale pores and gaps. This could be due to vacancy condensation at the scale metal interface [17] or within the scale [18] resulting from the rapid cation transport in the magnetite layer. When water vapour or OH^- access the inner scale, oxygen mobility is enhanced and those voids grow [9].

Rahmel and Tobolski [19] and Fujii and Meussner [20-21] support this idea. They stated that H_2O within the pores will provide the gaseous mass transport necessary for the oxide scale growth. As illustrated in Chapter I (Figure I.16), fast inward H_2O transport into the pores could insure a partial pressure of H_2O in the cavities close to the ambient gas. The oxygen transport is therefore ensured by this water vapour decomposition occurring at the side of the cavity near the metal. H_2 is a product of the decomposition reaction and its effect on the oxidation behavior of the alloys in wet environment is still not well understood.

The formation of pores and gaps is the dominating factor which can affect the mechanical integrity of the scale-substrate system. Spalling often occurs for steam grown oxide scales. For the overall oxidation resistance, the interface where the oxide spalls is of major importance. Because the defect structure of the oxide scales varies with the exposure duration, it is difficult to predict when spalling will occur.

In water vapour enriched environment at 650°C, 9% Cr steel shows its limits. The porous and thick scale developed makes it improper for a long term industrial use in the targeted service conditions. It is thus necessary to propose solutions for improving the high temperature oxidation behavior of this alloy especially in wet environment.

REFERENCES

[1] P. Kofstad, High Temperature Corrosion, Elsevier Applied Science, London (1988).
[2] D. Laverde, T. Gomez-Acebo and F. Castro, Corrosion Science, 46 (2004) 613.
[3] J. Jianmin, M. Montgomery, O. H. Larsen and S. A. Jensen, Materials and Corrosion, 56 (2005) 459.
[4] V. Lepingle, G. Louis, D. Allue, B. Lefebvre and B. Vandenberghe, Corrosion Science, 50 (2008) 1011
[5] W.J. Quadakkers, P.J. Ennis, J. Zurek and M. Michalik, Materials at High Temperatures, 22 (2005) 47.
[6] A. Rahmel and J. Tobolski, Corrosion Science, 5 (1965) 333.
[7] H. Nickel, Y. Wouters, M. Thiele and W. J. Quadakkers, Fresenius' Journal of Analytical Chemistry, 361 (1998) 540.
[8] J. Ehlers, D. J. Young, E. J. Smaardijk, A. K. Tyagi, H. J. Penkalla, L. Singheiser and W. J. Quadakkers, Corrosion Science, 48 (2006) 3428.
[9] D. J. Young, High Temperature Oxidation and Corrosion of Metals, Elsevier Corrosion series, Cambridge (2008).
[10] G.C Fryburg, R. A. Miller, F.J Khol and C. A. Stearns, Journal of Electrochemical Society, 124 (1977) 1738.
[11] S. Henry, Ph.D thesis , Institut National Polytechnique de Grenoble, Grenoble, France (2000).
[12] W.J Quadakkers, M. Thiele, P.J Ennis, H. Teichmann, W. Schwarz in Eurocorr 97, proceeding, European Federation of Corrosion, 2 (1997) 35.
[13] W.J. Quadakkers, P.J. Ennis, J. Zurek and M. Michalik, Materials at High Temperatures, 22 (2005) 47.
[14] P. J. Ennis, W. J. Quadakkers, International Journal of Pressure Vessels and Piping, 84 (2007) 75
[15] A. Galerie, B. Pieraggi. M. Soustelle, Oxidation des Matériaux Metalliques comportement à haute température, directed by A.M Huntz, B. Pierragi , Lavoisier (2003) 99
[16] A. Galerie, Y. Wouters, M. Caillet, Materials Science Forum, 369 (2000) 231
[17] S.R. J. Saunders, L.N. Mac Cartney, Materials Science Forum, 522 (2006) 119
[18] M. Michalik, M. Hänsel, J.Zurek, L.Singhheiser, W.J. Quadakkers , Materials at High Temperature, 22 (2005) 213.
[19] A. Rahmel, J. Tobolski, Corrosion Science, 5 (1965)333
[20] C.T Fujii, R. A. Meussner , Journal of the Electochemistry Society, 110 (1963) 1195
[21] C.T Fujii, R. A. Meussner , Journal of the Electochemistry Society,111 (1964) 1215

V. Ways to improve 9%Cr steel high temperature corrosion resistance

The two previous chapters pointed out the limits of 9%Cr steel at 650°C in both dry and wet environment. Indeed at high temperature and under high pressure, engineering pieces (heat exchanger, boilers etc…) made from this grade could form thick non protective oxide scale which could spall and lead to material degradation. Moreover, the oxide could be responsible for thermal isolation and component overheating in service conditions [1]. To conserve the use of such material which has shown important mechanical performance, several ways to improve its high temperature corrosion behavior will be discussed in this chapter. During this work, several solutions were tested such as aluminide coatings by pack cementation process in order to form the Fe/Al intermetallic species which could form a protective scale of alumina (Al_2O_3) during oxidation. Metal Organic Coating Vapour Deposition technique was also used for applying rare earth oxide coatings on substrate samples. The effect of alloying elements addition in the bulk of the steel is a major part of this PhD work. A set of new castings based on different known properties of alloying was proposed and realized using the levitation melter method.

Those prepared solutions were tested in laboratory air and in air enriched in water vapour at 700°C and 750°C in order to have access to critical information and to guarantee the validation of the solution between 50°C and 100°C higher than the targeted working temperature. Cyclic oxidation test were also carried out at 650°C in similar atmosphere and the obtained results will be presented in the following sections.

V.1 Coatings and high temperature oxidation resistance

V.1.1 Pack cementation coatings

The objective of this surface treatment is to develop an intermetallic phase FeAl enable the growth of a protective alumina scale during oxidation. Indeed, deposition of aluminum is widespread for high temperature industrial applications; several deposition methods such as CVD and slurry coatings, were shown as pertinent in the literature [2-6]. Pack cementation

aluminide coatings were realized on 9%Cr steel specimens following the pack preparation and the method developed by Houngninou [7] and described in chapter II (paragraph II.6).

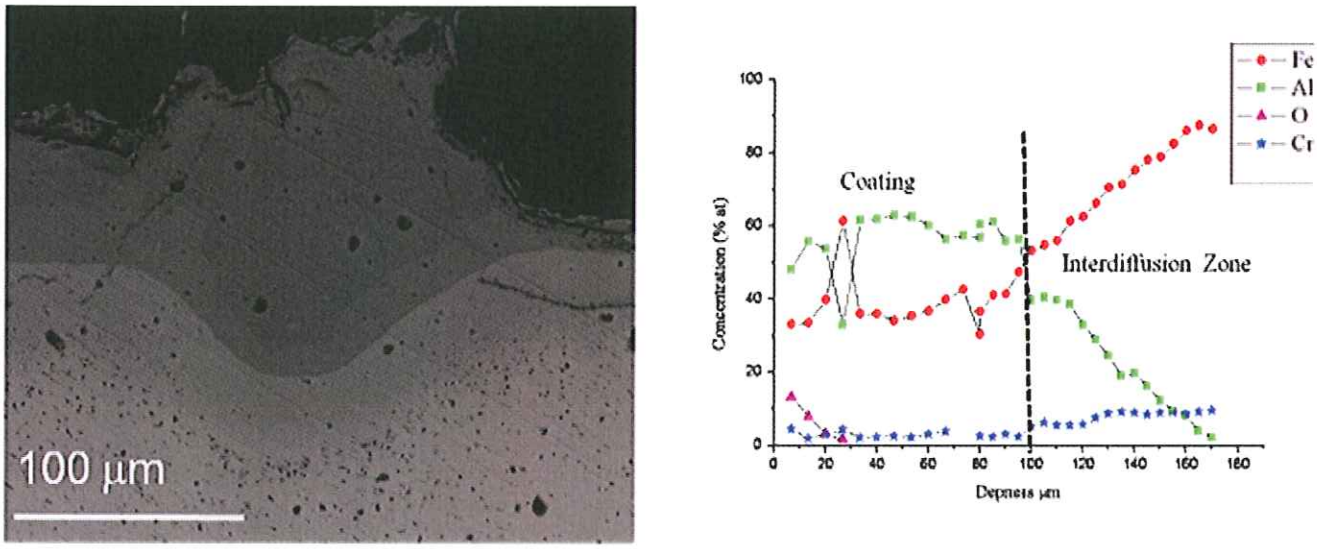

a) b)

Figure V.1: a) SEM cross section micrograph of aluminide coated sample. b) EDX analysis on the cross section.

Cross sections of the samples were investigated by means of SEM/EDX analyses. Figure V.1 presents the SEM micrograph using back scattered electron beam, of an aluminized sample cross section. Heterogeneity in the coating thickness is observed with punctually intermetallic zone which could measure more 100 µm thick.

Different layers are highlighted on both the SEM micrograph Figure V.1 and on the EDX profiles. Rich aluminum phases $FeAl_2$ is identified at the top of coating; beneath it several composition of iron aluminide compound could be seen. If the aim of this technique is to enrich the top surface of aluminum, a too rich phase could be detrimental to the mechanical properties of the steel.

An improvement of the aluminide coating process could be proposed by controlling parameters such as the temperature or the metal content in the pack mixture. In the literature papers proposed to decrease the aluminum activity by choosing Cr 75%/ Al 25% as the metallic fine powder for the pack mixture [9-10].

Then an experimental pack cementation containing a mixture of 58 wt % of Al_2O_3 (activated, -325mesh, 92% purity), 2 wt % of NH_4Cl and 48 wt % Cr85%/Al 15% (approx. 99% purity, particle size: 100 µm) was also studied. The dwelling temperature and time were fixed at 700°C and 12 hours. The obtained results were different from those reported earlier.

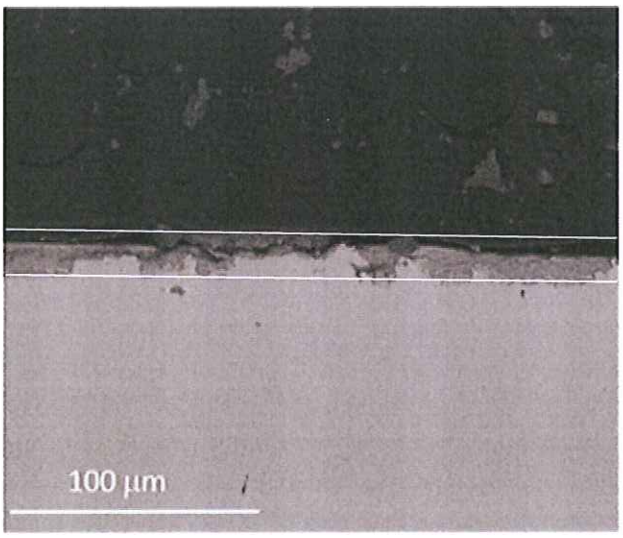

Figure V.2: SEM cross section micrograph of samples coated by pack cementation where the metallic part of the pack is a Cr85% Al 15% containing powder.

A coating layer of around 15 µm is observed in the micrograph shown in Figure V.2. According to the EDX analysis, no aluminum was detected in the coating layer. Indeed chromium rich phases ($Fe9Cr_3$) which were mainly formed on the top of the samples.

Oxidation test was carried out in laboratory air at 750°C for 100 hours on sample coated using this pack mixture.

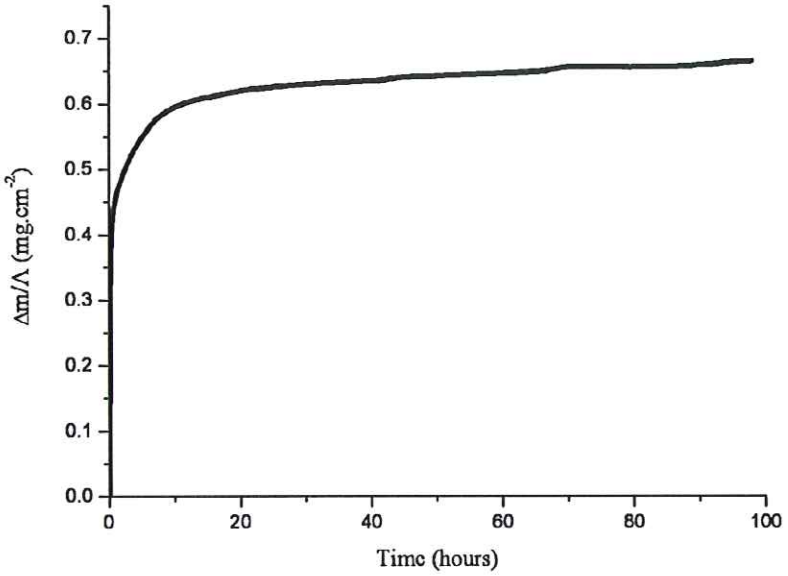

Figure V.3: kinetic curves of sample coated with low activity aluminum pack mixture and oxidized at 750°C for 100 h in laboratory air under atmospheric pressure.

In Figure V.3, mass gain followed a parabolic rate law. No breakaway is observed on that curve whereas a linear rate law was established after less than 30 hours of exposure at this temperature for non coated sample.

Parabolic rate constant was calculated from the slope of the transformed curve $\left(\frac{\Delta m}{A}\right) = f(\sqrt{t})$; $k_p = 2.1 \times 10^{-14}$ $g^2.cm^{-4}.s^{-1}$, is then obtained which is two order of magnitude less than that obtained for uncoated samples ($k_p = 9.6 \times 10^{-13}$ $g^2.cm^{-4}.s^{-1}$).

One can states that in this case, the coating has a beneficial effect on the behavior of the 9%Cr steel at high temperature. This could be due to the formation of a protective chromia scale which grew from iron chromium rich zone obtained after the pack cementation coating.

Other CVD coating methods were also tested for improving the 9% Cr steel high temperature corrosion behaviour, among them, the Metal Organic Chemical Vapour Deposition of rare earth.

V.1.2 Reactive element oxide coating by Metal Organic Chemical Vapour Deposition (MOCVD).

The beneficial effects of reactive elements (better adhesion of oxide scale, nuclei for germination of oxide, modification of the diffusion of species within the oxide scales etc...) were highlighted in several works [10-12]. Therefore thin layer of lanthanum oxide (La_2O_3) neodymium oxide (Nd_2O_3), and yttrium oxide (Y_2O_3) were deposited on samples using the Metal Organic Chemical Vapour Deposition technique (MOCVD). Coatings around 200-400 nm thick were obtained for each specimen. Isothermal tests were performed on La_2O_3 and Y_2O_3 coated samples for 200h in laboratory air at 700°C under atmospheric pressure.

Samples	$\Delta m/A$ ($mg.cm^{-2}$)
Uncoated sample (Reference)	0.13
La_2O_3 coating	0.25
Y_2O_3 Coating	0.16

Table V.1: Mass gain obtained after oxidation in laboratory air at 700°C for 200h for uncoated and coated samples

Table V.1 shows that higher mass gain is observed for the coated samples than the uncoated one, which was not really what was expected.

Figure V.4 shows SEM micrographs taken after oxidation of the samples. For the La_2O_3 coated sample on Figure V.4 a) a non homogenous surface is visible. Bumps are formed all over the coatings scale. According to the EDX analyses, lanthanum, manganese, chromium

and iron are identified in the scale. For the Y_2O_3 coated sample (Figure V.4b)) a homogenous surface could be observed; EDX analysis characterized Y and O as the main element constituting the scale. But, cracks in the protective oxide coating are formed. White nodules enriched in chromium and manganese oxide grow along those cracks.

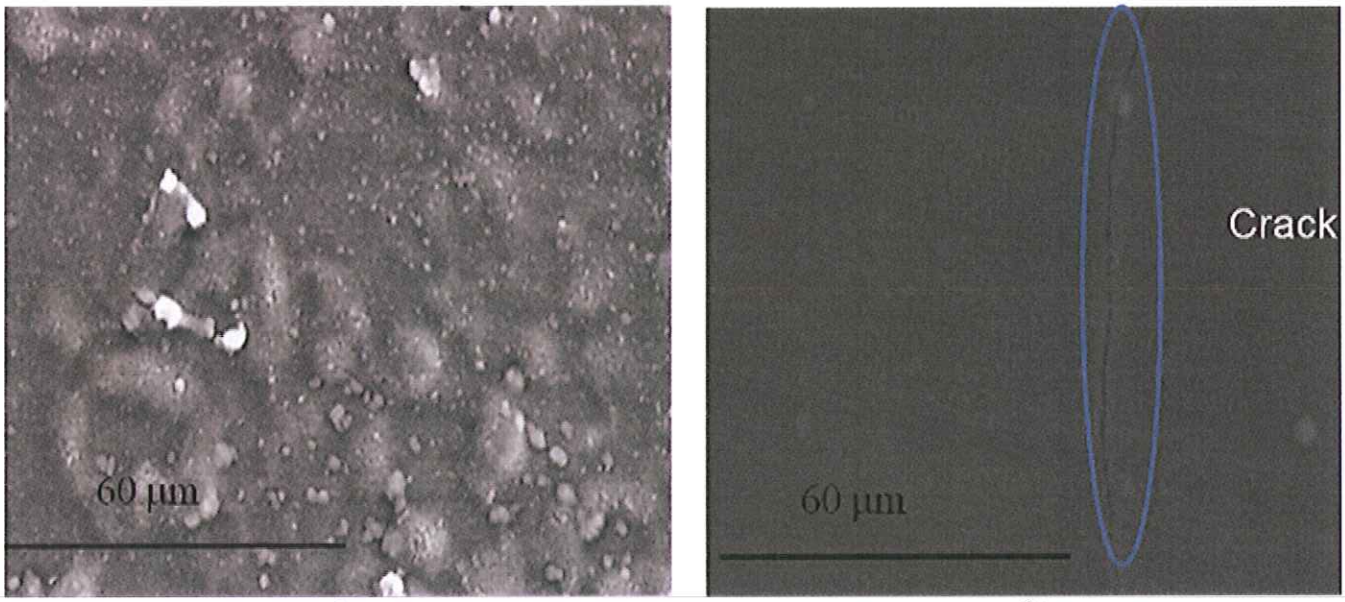

a) b)

Figure V.4: SEM surface micrograph of a) La_2O_3 coated sample, b) Y_2O_3 coated sample after oxidation for 200h at 700°C in laboratory air.

Isothermal test at 750°C for 200 hours was also performed on La_2O_3 coated sample. Table V.2 lists the final mass gain observed for the uncoated and the coated sample after this oxidation test.

Samples	$\Delta m/A$ ($mg.cm^{-2}$)
Uncoated sample (Reference)	1.4
La_2O_3 coating	1.3

Table V.2: Mass gain obtained after oxidation in laboratory air at 750°C for 200h for uncoated and coated sample

Figure V.5 a micrograph of La_2O_3 coated 9%Cr steel oxidized 200h at 750 h in air. Spalling of the rare earth oxide coating is observed and the growth of chromium oxides, iron chromium spinel, chromium and /or iron -manganese spinel oxides are seen beneath the spaled layer (left part of Figure V.5). The spall of the coating could be due to a difference of thermal expansion coefficient between the substrate and the lanthanum oxide. But, one can also state that no clear interaction was made between the 9%Cr steel grade and its coating during the MOCVD deposition process. The two entities have therefore their own behavior independently from each other at high temperature.

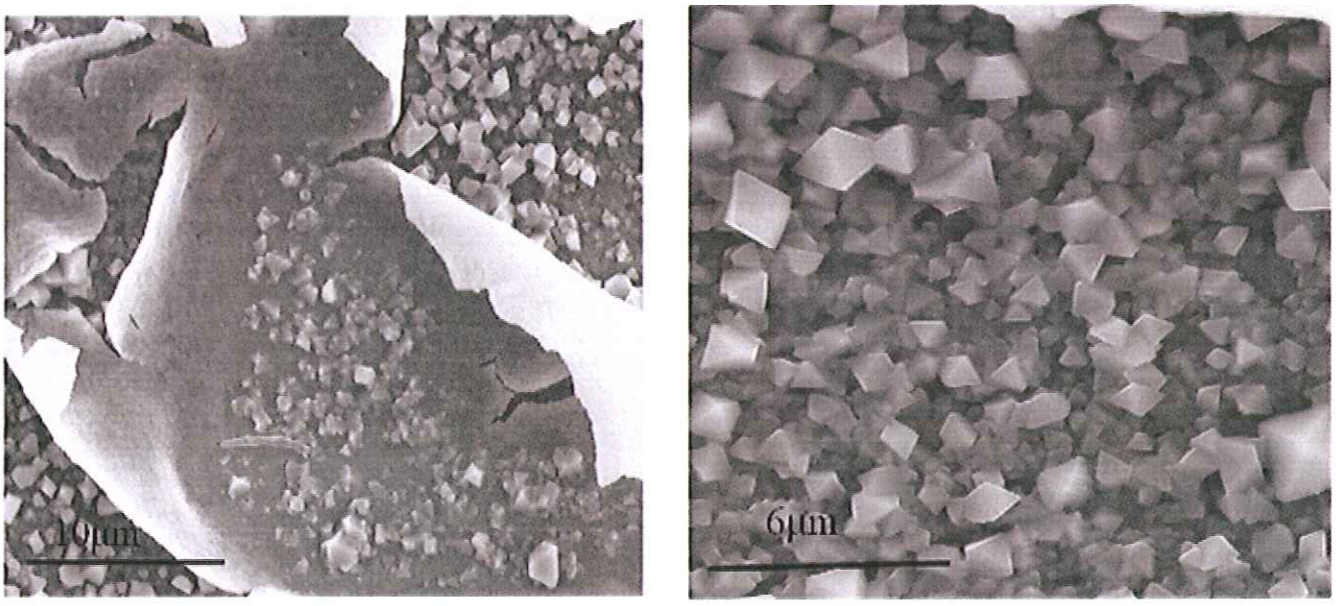

Figure V.5: SEM surface micrograph of La_2O_3 coated sample after oxidation for 200h at 750°C in laboratory air.

V.1.3 Cyclic tests at 700°C in laboratory air.

Both aluminide coated samples and MOCVD coated samples were submitted at high temperatures cyclic tests experiment in order to evaluate the resistance of those solutions. The La_2O_3 coated sample was pre-oxidized for 30min in a muffle furnace at 800°C in lab air under atmospheric pressure. Indeed, according to Fontana's work [97], pre-oxidized treatment on MOCVD coatings can be favorable for high temperature corrosion behavior of Cr containing alloys. Indeed, the pre-oxidation could allow greater segregation of the reactive elements inside the grain boundaries of the chromium rich oxide scale formed during the first instant of oxidation. The segregated reactive elements could act as a barrier and impede the cationic outward diffusion. Cyclic experiments were performed on uncoated sample (reference), La_2O_3 coated and pre-oxidized, La_2O_3 coated, Y_2O_3 coated, Nd_2O_3 coated samples and an aluminide coated samples. Each cycle was composed of a 24h exposure at 700°C in lab air under atmospheric pressure, and an air quenching until reaching room temperature.

In total, 28 cycles were performed, corresponding to 672 hours of exposure at 700°C. Figure V.6 summarizes mass evolution for those samples.

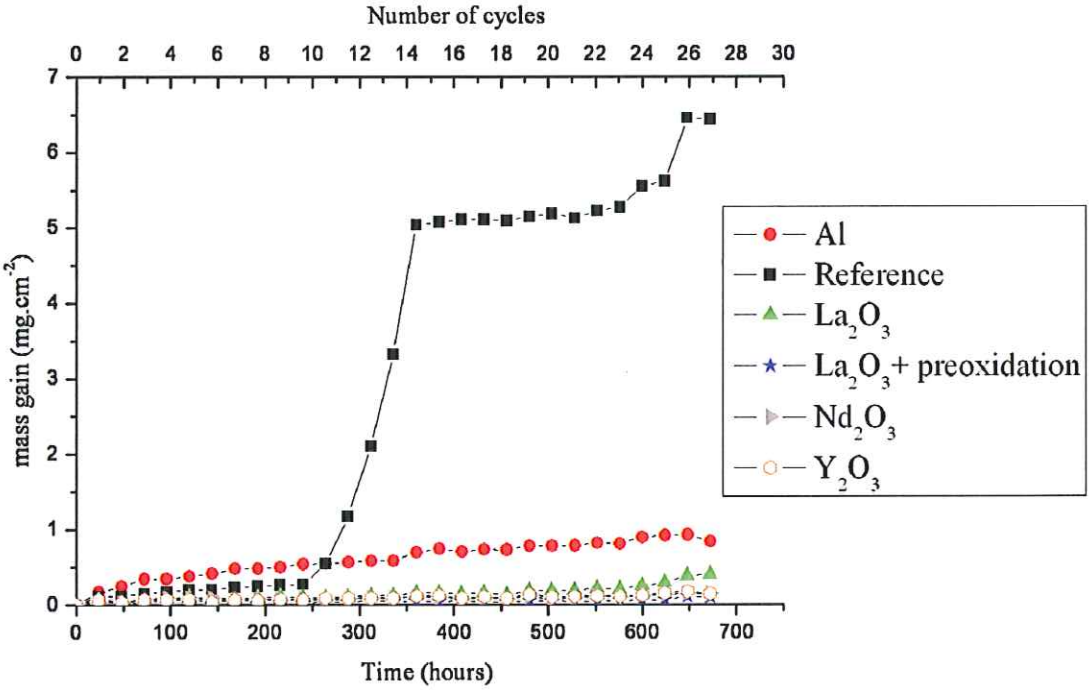

a)

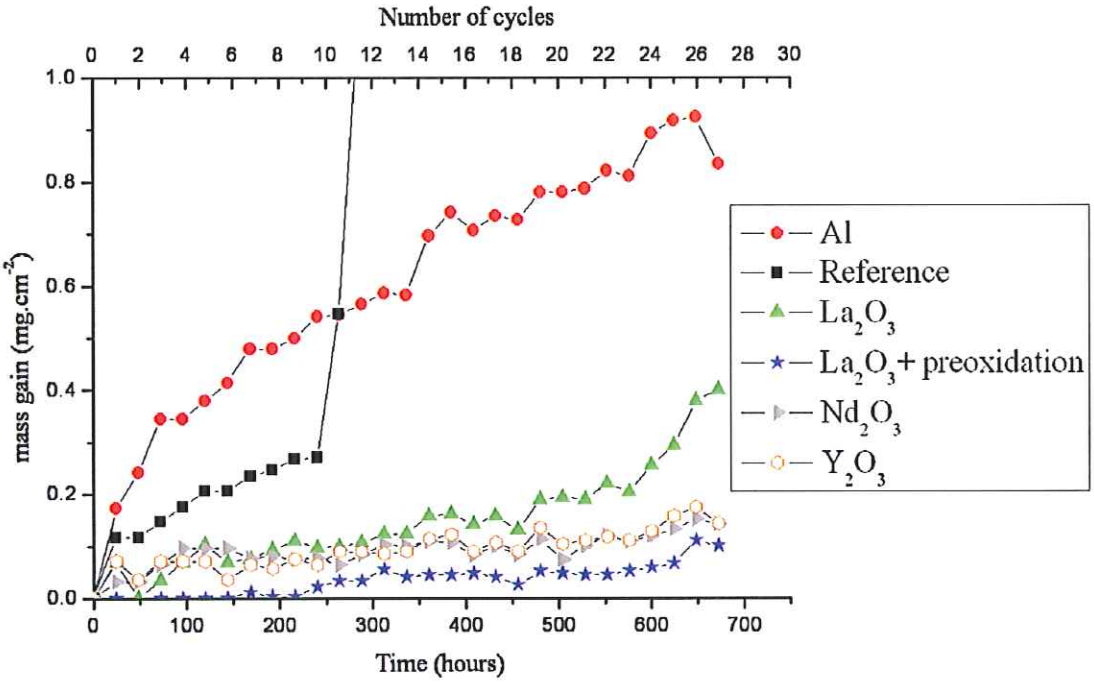

b)

Figure V.6: a) Kinetic curves for uncoated and coated samples after 28 cycles of 24 hours at 700°C in lab under atmospheric pressure. b) Scale Zoom

After 9 cycles, the uncoated sample mass increased quickly. The kinetic of the reaction changes from a parabolic to a linear law; "breakaway" phenomenon is observed. All coated samples still follow a parabolic kinetic mass evolution and really low mass gains are registered. Among the coated samples, aluminide coated sample which displays the highest mass gain whereas La_2O_3 coated and La_2O_3 coated and followed by a pre-oxidation display the lowest mass evolution. The nature and the density of the formed oxide on those coated samples could explain the difference of mass gain registered in each case.

Samples	Reference	La_2O_3	La_2O_3 Preox	Nd_2O_3	Y_2O_3	Aluminide coating
k_p cyclic tests at 700°C in ($g.cm^{-4}.s^{-1}$)	$9.5x10^{-14}$	$2.1x10^{-17}$	$4.2\ x10^{-18}$	$1.x\ 10^{-17}$	$1.3\ x10^{-17}$	$3.6x10^{-16}$

Table V.3: Kinetic rate constants for coated and uncoated samples after 29 cycles at 700°C.

In Table V.3 kinetic rate constants are listed for the coated and uncoated samples after the cyclic test. La_2O_3 coated and pre oxidized sample show the smallest kinetic rate constants $4.2\ x10^{-18}\ g^2.cm^{-4}.s^{-1}$ respectively. This value is 4 orders of magnitude lower than the k_p calculated for the reference ($9.5x10^{-14}\ g^2.cm^{-4}.s^{-1}$).

Beneficial effects of rare earth elements are highlighted here in cyclic conditions. Nevertheless coating and especially MOCVD coating could be difficult to adapt at industrial scale. Indeed, application of such coatings on engineering pieces could be difficult moreover the impact on the thermal conductivity and the welding performance of the coated tubes should be investigated. Therefore other ways to enhance 9%Cr steel high temperature corrosion resistance have been propose in this work.

V.2 Effect of alloying elements addition

The effects of alloying element addition on high temperature oxidation behavior of steel were discussed at the end of Chapter I. Castings were done at OCAS N.V using the levitation melter Each ingot was hot rolled, then normalized at 1050°C for 30min, then tempered at 790°C for 60 min and air cooled. In table V.4 are listed the castings which have been prepared during this work.

Cast Code	Composition in (wt %)																		
	C	Mn	Si	P	S	Al	Ti	Nb	Cu	Cr	Ni	Sn	O	N	B	Mo	V	Y	Ce
Fe9Cr (ss V)		0.38	0.19	0.002		0.12	0.0007	0.069	0.004	9.11	0.092					0.92	0.011		
Fe9Cr		0.36	0.19	0.002		0.11	0.0008	0.090	0.005	8.67	0.087					0.99	0.19		
Fe9Cr (1% Si)		0.37	0.84	0.002		0.11	0.0009	0.087	0.007	8.52	0.091					0.92	0.19		
Fe9Cr (3% Si)		0.36	2.62	0.003		0.11	0.0034	0.083	0.007	8.15	0.086					0.89	0.18		
Fe9Cr (Y)	0.065	0.38	0.22	0.0023	0.0016	0.0078	0.0026	0.079	0.014	8.55	0.098	0.0032	0.0055	0.013	0.0005	1.08	0.19	0.025	
Fe9Cr (Ce)	0.072	0.37	0.22	0.0023	0.0012	0.0073	0.0026	0.077	0.014	8.26	0.094	0.0032	0.0035	0.0072	0.0005	1.05	0.19		0.021
Fe9Cr (Al)	0.025	0.36	0.2	0.0023	0.003	0.47*	0.0026	0.08	0.014	8.43	0.099	0.0034	0.0018	0.0032	0.0006	1.08	0.19		
Fe9Cr (Ni)	0.059	0.38	0.23	0.0024	0.0025	0.008	0.0028	0.078	0.015	8.59	0.562	0.0034	0.0018	0.0029	0.0005	1.06	0.19		
Fe9Cr (0.5% Si)	0.074	0.37	0.54	0.0024	0.0026	0.0071	0.0026	0.074	0.013	8.17	0.093	0.0032	0.0022	0.0059	0.0005	1.02	0.19		
Fe9Cr (1.5% Si)	0.069	0.36	1.48	0.0033	0.0029	0.0069	0.0032	0.075	0.017	8.5	0.092	0.0039	0.0027	0.0068	0.0005	1.06	0.17		
Fe9Cr (2% Si)	0.063	0.37	2.01	0.0033	0.0029	0.0067	0.0035	0.076	0.018	8.49	0.093	0.0048	0.0023	0.0068	0.0006	1.05	0.18		
Fe9Cr (2.5% Si)	0.072	0.35	2.21	0.0033	0.0031	0.0056	0.0032	0.072	0.018	8.1	0.095	0.0053	0.0027	0.011	0.0006	1.01	0.18		
Fe9Cr ('4% Si)	0.077	0.36	4.07	0.0037	0.0038	0.0065	0.0049	0.073	0.018	8.27	0.093	0.0063	0.0036	0.013	0.0007	1.02	0.17		

Table V.4: Casting composition according to ICPMS and combustion test analyses.

The main idea behind the castings composition were in the case of rare earth addition in the bulk to produce the well known reactive element effects [10-12] which could increase the high temperature corrosion behavior of alloys by doping the formed oxide scale, increasing their adherence to the substrate or serve as nuclei for the germination of a protective oxide layer with small grain sizes. In the case of aluminum and Nickel addition to the substrate, the formation of stable NiO or Al_2O_3 which was targeted when exposed in oxidizing atmosphere. For the casting where silicon was added, the objective was to provide enough silicon to form a continuous thin SiO_2 layer which could help to enhanced 9% Cr steel corrosion resistance behavior by slowing down species diffusion. Casting without vanadium was also proposed and have also been tested. Vanadium is usually added as a structural element in steel in order to form vanadium carbide which precipitate and increase mechanical properties of the steel. But, detrimental volatile oxide such as V_2O_5 could be formed at high temperature in oxidizing condition. Figure V.7 presents oxide morphology formed on 9% Cr steel after oxidation at 700°C for several hundred hours. Oxides in form of droplets are seen on the surface.

Vanadium is the main element characterized in those droplets. It could be V_2O_5 which is a vanadium oxide with a melting point around this temperature. Such an oxide may have detrimental effects on the corrosion resistance of the materials.

Moreover, a 9%Cr steel casting was realized without any alloying element addition in order compare its behaviour to the reference materials. This casting will be noted as follow "Fe9Cr". It will be used to show that the casting realization method and the subsequent thermal treatment cannot be held as responsible for the improvement observed in the case of the new castings.

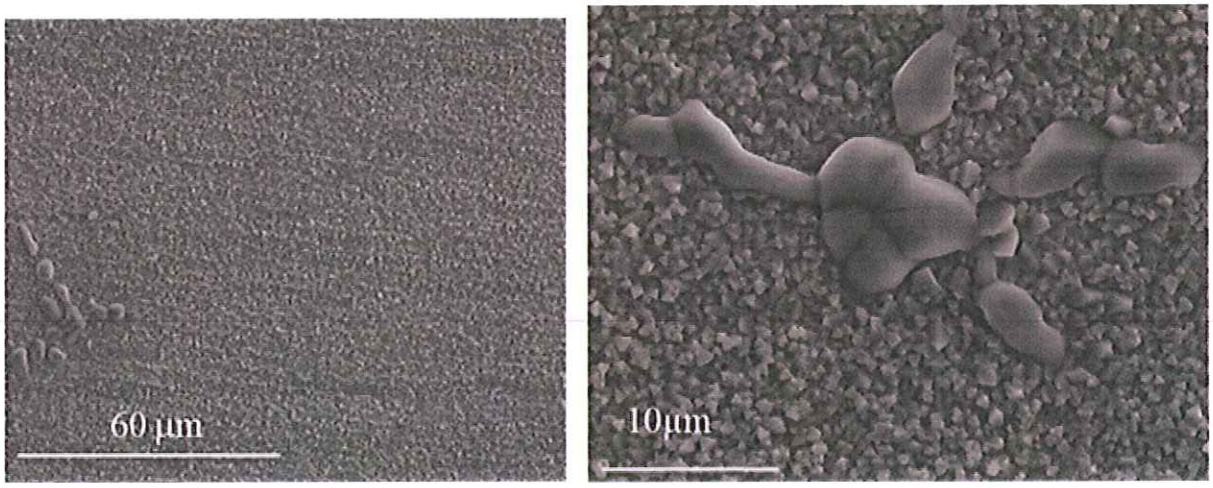

Figure V.7: SEM surface micrographs oxide 9%Cr steel oxidized in laboratory air at 700°C for 400 h.

One should keep in mind that when changing the casting composition, a compromise should be found between high temperature behavior of the steel and its mechanical properties for the desired application.

V.2.1 Fire side corrosion tests

V.2.1.1 Isothermal test at 750°C in laboratory air

The behavior at high temperature of silicon enriched 9%Cr steel and casting without vanadium was investigated and the obtained results are reported in this section. Isothermal tests were performed at 750°C for 100h in laboratory air under atmospheric pressure on silicon containing alloys Fe9Cr (0.5 wt % Si), Fe9Cr (1.5 wt % Si) and Fe9Cr (no Vanadium) and compare to similar experiment run on the 9% Cr steel grade use as reference.

Low mass gain is observed at 750°C for the casting containing (0.5wt % Si) after 100 hour of oxidation, (see Figure V.8). A parabolic rate constant was calculated from the slope of this curve k_p = 2.2x $10^{-14} g^2 .cm^{-4} .s^{-1}$. This value is two orders of magnitude lower than the one calculated for the reference in the same oxidizing condition.

Indeed a k_p =1x10^{-12} g^2 $.cm^{-4}$ $.s^{-1}$ was calculated from the parabolic part of the reference sample curve after oxidation a 750°C. Figure V.8 allows to compare the mass gain of the reference sample to the one observed for Fe9Cr (0.5 wt % Si). No breakaway is observed in the case of the new casting after oxidation at 750°C. The mass obtained in the case of the casting enriched in silicon could be compared to that obtained for 9%Cr, which is used as reference, after oxidation at 650°C. A clearly beneficial effect is thus observed in this case.

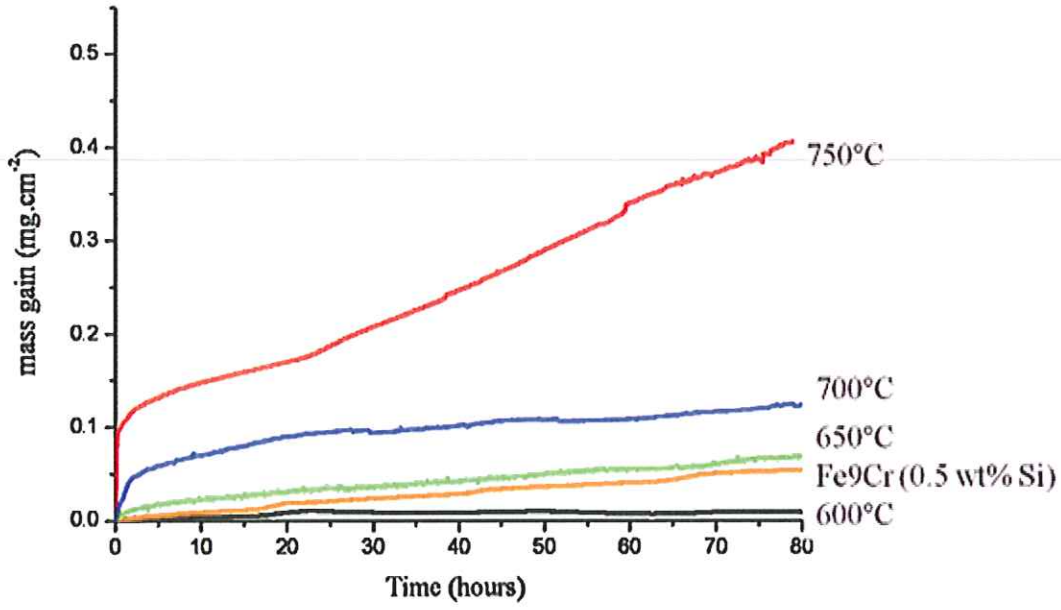

Figure V.8: Mass gain observed at 750°C for 100 h on Fe9Cr (0.5 wt % Si) and comparison with the reference

The results obtained for isothermal oxidation on samples enriched with 1.5 wt % of Si are presented below. Here also low mass gain is observed (Figure V.9) for the sample enriched in silicon.

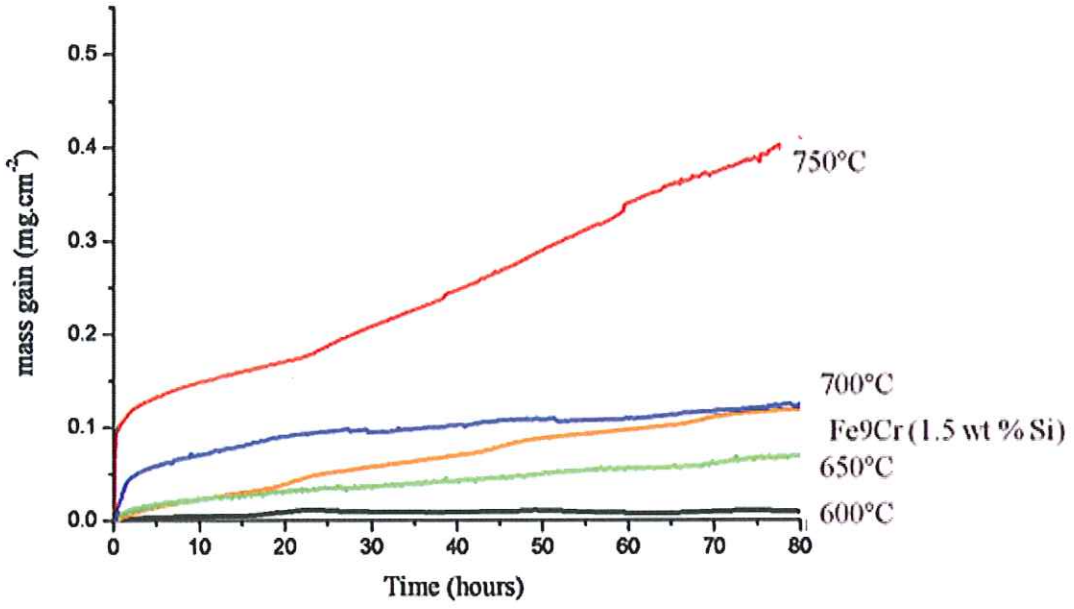

Figure V.9: Mass gain observed at 750°C for 100 h on Fe9Cr (1.5wt % Si) and comparison with the reference

Parabolic rate constant calculated in this case ($k_p = 8.5x10^{-14}$ g^2 $.cm^{-4}$ $.s^{-1}$) is also two orders of magnitude lower than the one calculated for the reference after similar oxidation test. But this time when comparing Fe9Cr (1.5 wt % Si) with mass gain obtained for the 9%Cr steel reference grade (Figure V.9), it could be concluded that we have a final mass gain relatively equal to the reference one when oxidized at 700°C . Nevertheless for Fe9Cr (1.5 wt % Si) a beneficial effect of silicon addition is clearly observed.

Figure V.10 presents mass gain followed by thermogravimetry at 750°C for 100 hours in laboratory air under atmospheric pressure for the casting with almost no vanadium in its composition. Low mass gain is observed.

The calculated parabolic rate constant $k_p = 2.8$ $x10^{-14}$ g^2 $.cm^{-4}$ $.s^{-1}$ is smaller than the one observed for reference at 750°C. Indeed, when comparing the mass gain of both castings in the same oxidizing condition, it is clearly visible that the casting without vanadium has a better behavior. Nevertheless the final mass gain is higher than that obtained for example at 700°C for the 9%Cr steel reference grade (Figure V.10).

Figure V.11 is a superposition of the kinetic data registered for Fe9Cr (0.5 wt % Si), Fe9Cr (1.5 wt % Si) and Fe9Cr (0.01 wt % V) oxidized at 750°C in laboratory air under atmospheric pressure. Figure V.11 displays for all new castings lower mass gain at 750°C than for the reference sample. Changes in the casting composition had clearly an impact on the high temperature corrosion behavior. No "breakaway" is observed after 25h whereas it is

the case for the reference. The casting with 0.5 wt % Si has the lower mass gain. The low vanadium casting has at 750°C the worst oxidation resistance behavior among the new tested castings but the difference in final gain with Fe9Cr (1.5 wt % Si) is not significant . Comparison between the casting with 0.5 wt % Si and the one with 1.5 wt % Si leads to think that there is an optimum amount of silicon where its effect is maximum on the corrosion resistance behavior. This optimum amount should be determined by further experiments. Nevertheless the hypothesis of the formation of a dense and thick SiO_2 layer due to the presence of more Si in the composition of the casting with 1.5 wt % Si could be an explanation to the difference of mass gain observed when comparing with the casting containing 0.5 wt % Si.

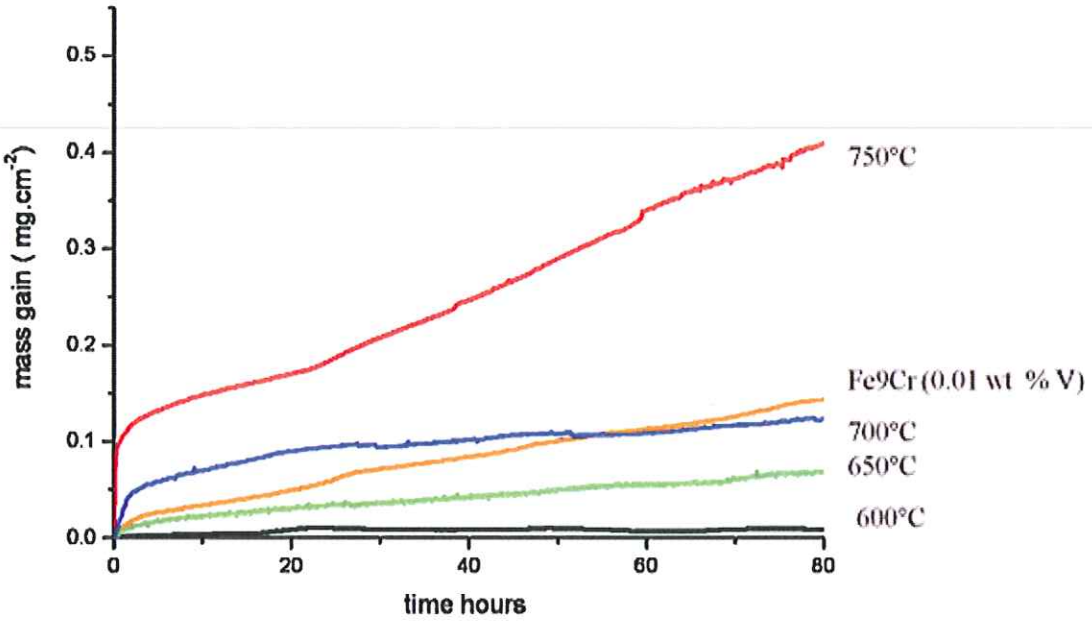

Figure V.10: Mass gain observed at 750°C for 100 h on Fe9Cr (0.01 wt % V) and comparison with the reference

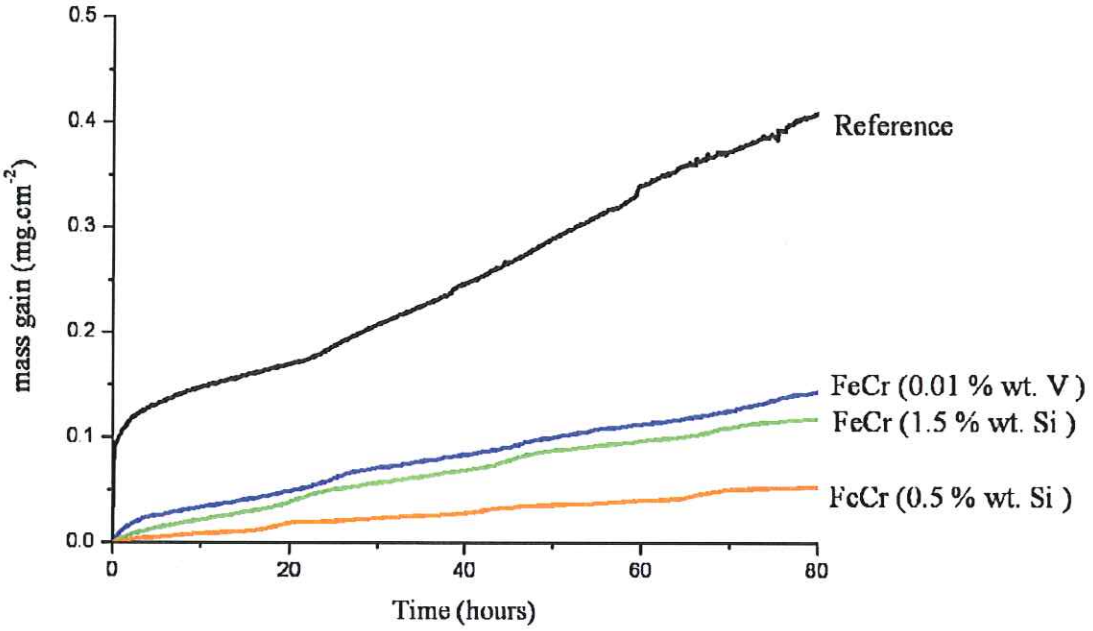

Figure V.11: Mass gain observed at 750°C for 100 h for Fe9Cr (0.01 wt % V), Fe9Cr (0.5wt % Si), Fe9Cr (1.5wt % Si) and comparison with the reference.

V.2.1.2 TEM results for casting enriched in silicon

Casting enriched in silicon such as Fe9Cr (0.5 wt % Si) and Fe9Cr (1.5 wt % Si) were aged at 650°C in laboratory air for 100h in order to investigate their formed oxide scales by TEM. FIB Cross section of the corrosion products grown on Fe9Cr (0.5 wt % Si) is shown in Figure V.12. A 150 nm thick oxide is formed on the top of the Fe9Cr (0.5 wt % Si) exposed in dry oxidizing atmosphere for 100h at 650°C. The metal oxide interface can be distinguished thanks to the presence of a white border (red bubble on Figure V.). EDX analysis performed on this sample give an idea of the oxide scale composition. Attention was paid to the metal/oxide interface composition and to the upper most part of the oxide scale. At the metal oxide interface, silicon oxide and vanadium oxide was detected by EDX. The composition of the upper part of the oxide scale is presented in Table V.5 below. These results highlight the formation of an oxide scale rich in chromium, and poor in iron which is the total opposite of what was observed in the same condition for the reference. Manganese oxide and silicon oxide are also present in the layer.

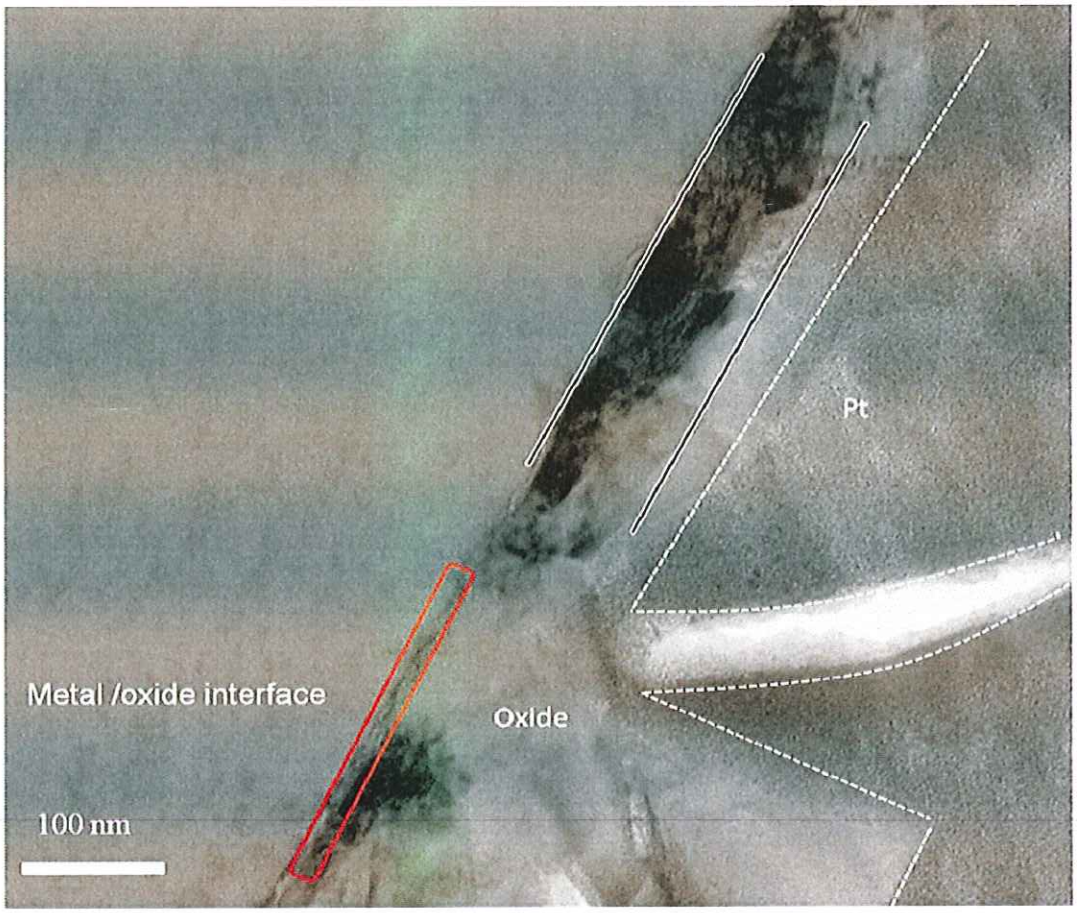

Figure V.12: TEM micrograph of oxide scale thermally grown on Fe9Cr (0.5 wt % Si) after exposure at 650°C for 100h in laboratory air.

Elts	O	Cr	Fe	Si	Mn
% weight	37.4	42.5	11.4	3.4	5.3
% atomic	65.3	23	5.7	3.3	2.7

Table V.5: EDX Semi quantitative analyses of the top the oxide scale grown on Fe9Cr (0.5wt % Si) after exposure at 650°C for 100 h in laboratory air.

Similar investigation was carried out on Fe9Cr (1.5wt % Si) oxidized for 100h at 650°C in laboratory air. In that case the oxide scale thickness was around 200 nm (Figure V.13 a)). Figure V.13 b) is a high magnification TEM micrograph. It displays clearly a continuous 1.5 nm thick oxide border at the interface between the metal and the oxide layer. Mainly amorphous silica was identified as constituent of the metal/oxide border. Moreover, the top surface scale composition, in that case, is also rich in chromium and poor in iron

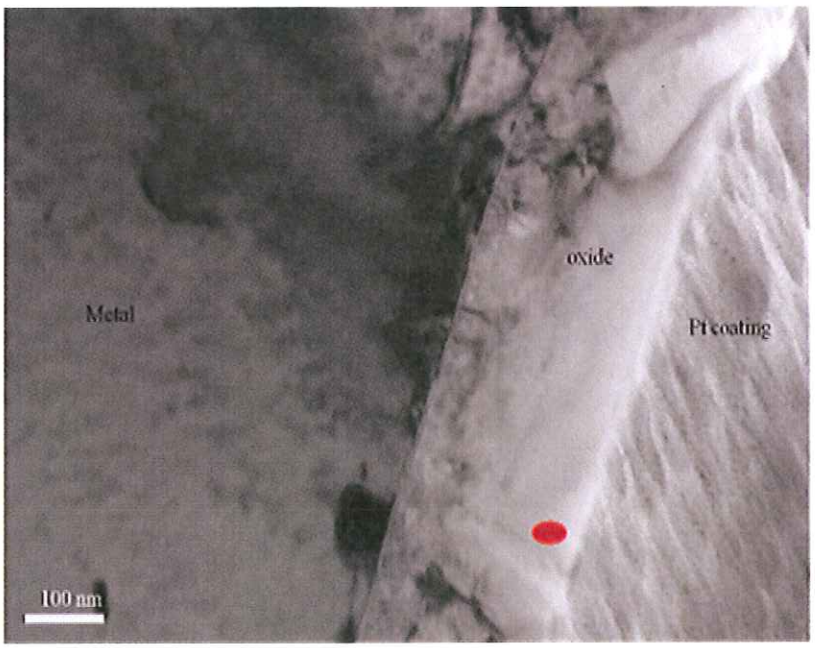

a)

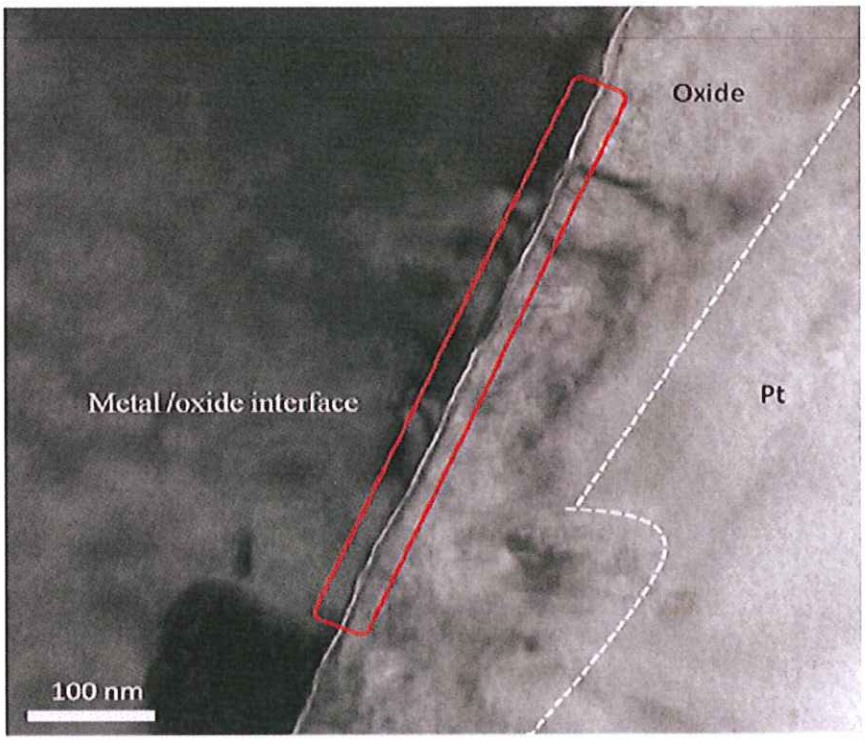

b

Figure V.13: a) TEM micrograph of oxide scale thermally grown on Fe9Cr (1.5 wt % Si) after exposure at 650°C for 100 h in laboratory air (red dot is an EDX analysis spot) b) High magnification TEM micrograph which highlighted the continuous metal/oxide interface.

The formation of a mixed iron chromium spinel oxide rich in chromium could be proposed as the main consequence of the addition of silicon in the bulk of the 9%Cr steel. Such an oxide scale could have a protective effect for the substrate. The presence of an amorphous silica phase at the interface metal/oxide could be responsible for some changes in cations outward diffusion. It could explain the fact that low iron concentration was detected in the outer most part of the formed oxide scale. As a result of the silicon addition effect, no Fe_2O_3 in the scale is the main difference observed with the corrosion products obtained for the reference steel oxidized in identical conditions.

V.2.1.3 Cyclic oxidation tests

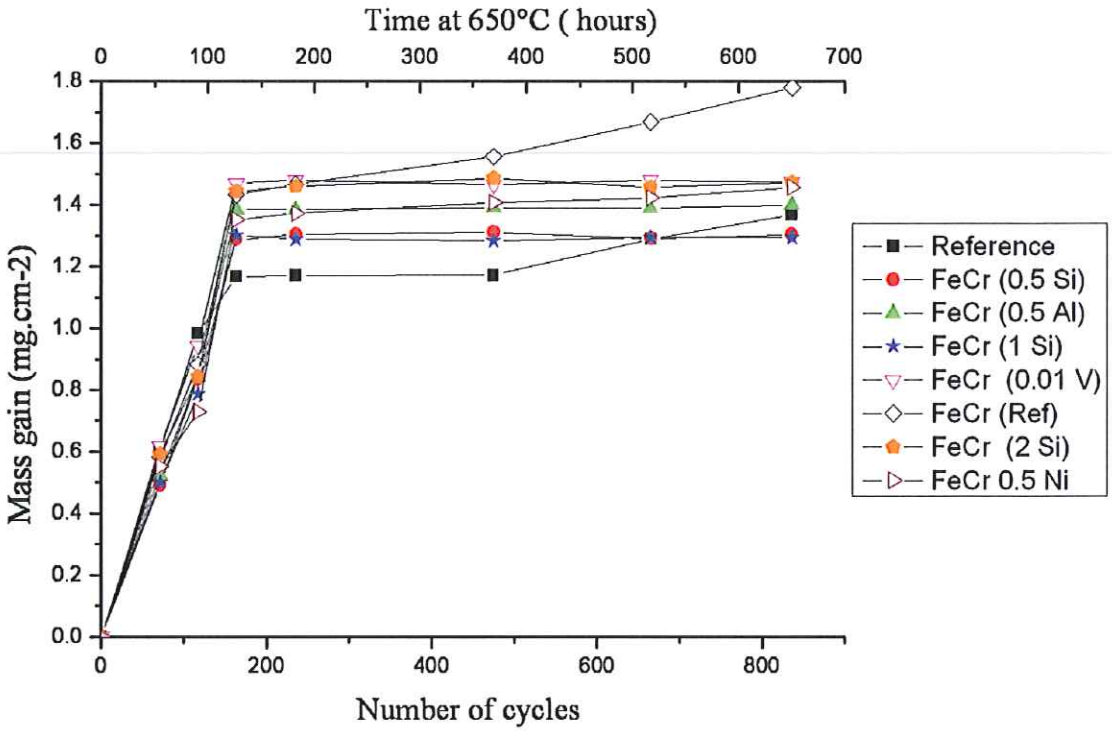

Figure V.14: 800 Cycles at 650°C in laboratory air under atmospheric pressure for Fe9Cr (reference sample for the new castings no composition modification in comparison with 9%Cr steel reference used for this study), Reference, Fe9Cr (0.01wt % V), Fe9Cr (1wt % Si), Fe9Cr (0.5wt % Si), Fe9Cr (2 wt % Si), Fe9Cr (0.5wt % Al), and Fe9Cr (0.5wt % Ni).

The new castings corrosion resistance was also tested in cyclic condition using the device presented in Chapter II (paragraph II.2.3). In Figure V.14 the first 800 hours of oxidation at 650°C in laboratory air under atmospheric pressure for the reference sample, Fe9Cr (reference samples for the new castings; no composition modification in comparison with the 9%Cr steel

reference used for this study), Fe9Cr (0.01 wt % V), Fe9Cr (1 wt % Si), Fe9Cr (0.5 wt % Si), Fe9Cr (2 wt % Si), Fe9Cr (0.5 wt % Al), and Fe9Cr (0.5 wt % Ni) are plotted.

No spallation of the oxide layer formed on those samples is observed during the cyclic oxidation tests. At the beginning of the experiment it is the reference which displays the higher total mass gain. After 150 hours, for all castings higher mass gains than for the reference are observed. This could be due to a difference in the nature of the oxide scale which grows at the surface of the samples with a modified composition. After 400 cycles, a breakaway is observed for both the reference sample and Fe9Cr. On the other hand all the other castings show no significant mass variation after 150 cycles. Fe9Cr (1 wt % Si), and Fe9Cr (0.5 wt % Si), have among the new castings the lowest mass gain. Ni and Al enriched samples show intermediary mass gain compare to the other new casting whereas the highest value of mass gain for modified samples are shown by Fe9Cr (0.01 wt % V) and Fe9Cr (2 wt % Si). But as mentioned before those slight differences in the measured mass gain among the new casting could be due to the nature of the oxide formed during the oxidation process and to their relative density.

Nevertheless it is clear that the minor changes made on the casting composition have a real effect on the high temperature corrosion resistance of 9%Cr steel especially in delaying the establishment of a linear kinetic regime of oxidation in cyclic conditions.

V.2.2 Effect of water vapour and steam.

V.2.2.1 Isothermal tests in water vapour environment and scale characterization

In chapter IV (paragraph IV.1.1) the bell shape relationship existing between temperature and mass gain for 9% Cr steel oxidized at high temperature in air enriched 12% vol. of water vapour have been highlighted. Maximum mass gain was observed at 700°C. Thus, isothermal tests in air enriched with 12% water vapour were also performed on the new castings using the experimental set-up described Chapter II (paragraph II.2.2). Figure V.15 is a superposition of the mass gain obtained after 100h of oxidation at 700°C in air enriched with 12% vol. of water vapour for the 9%Cr steel used as reference for this work, Fe9Cr (reference sample for the new castings, no composition modification in comparison with the reference), Fe9Cr (0.01 wt % V), Fe9Cr (0.5wt % Si), and Fe9Cr (1.5wt % Si):

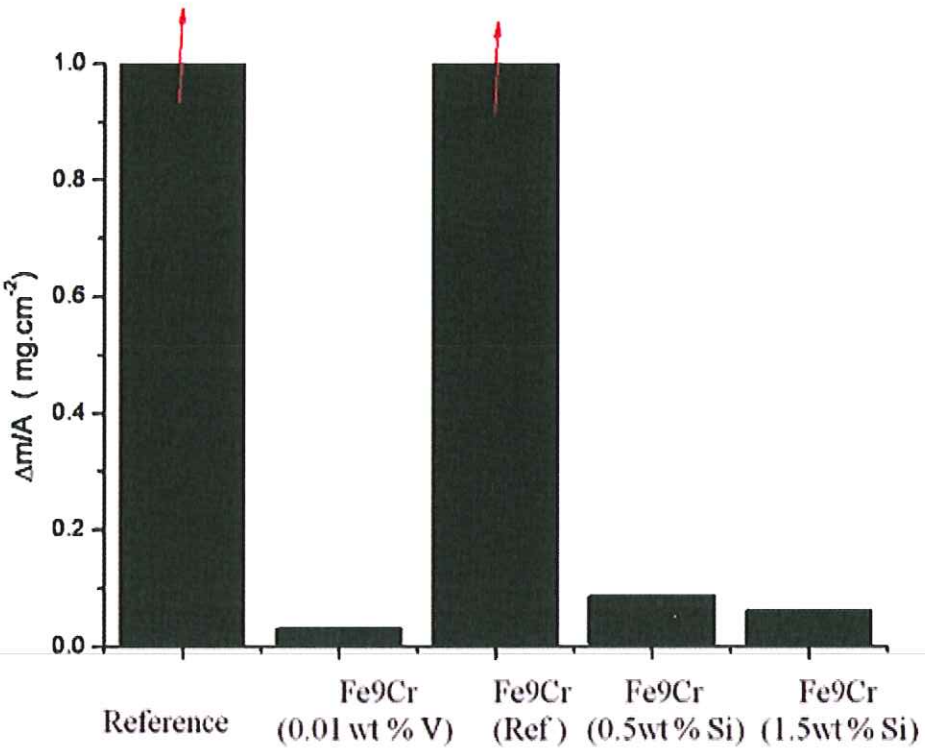

Figure V.15: Mass gain for Reference, Fe9Cr (reference sample for the new castings no composition modification in comparison with 9%Cr steel used as reference), Fe9Cr (0.01 wt % V), Fe9Cr (0.5 wt % Si), and Fe9Cr (1.5 wt % Si) after oxidation at 700°C for 100h in air + 12% vol. water vapour.

Figure V.15 displays important mass gain for the reference after oxidation at 700°C for 100 in air enriched with 12% vol. of water vapour. This is in agreement with what was observed in Figure IV.1. Similar conclusion could be drawn for Fe9Cr which has exactly the same bulk composition as the reference material. Indeed in this case really important mass changes are seen in Figure V.15. This important mass gain corresponds to the formation of iron oxide. Lower mass gain than for the references is clearly noticed for Fe9Cr (0.5wt % Si). This confirms the behavior highlighted in dry air at 750°C for 100 h. The effect of silicon addition is clearly evidenced. Moreover, when we focus on Fe9Cr (1.5 wt % Si) and Fe9Cr (0.01 wt % V) even lower mass gain is observed, with the lowest mass variation for the steel containing 1.5 wt % Si among the tested castings. Whereas in dry air, it was the steel containing 0.5 wt % Si which was the more impressive for high temperature resistance behavior, in wet atmosphere it is Fe9Cr (1.5 wt % Si) which has the better behavior.

Surface characterization of the oxide scale grown in such condition, was performed by SEM and XRD at low glancing angle.

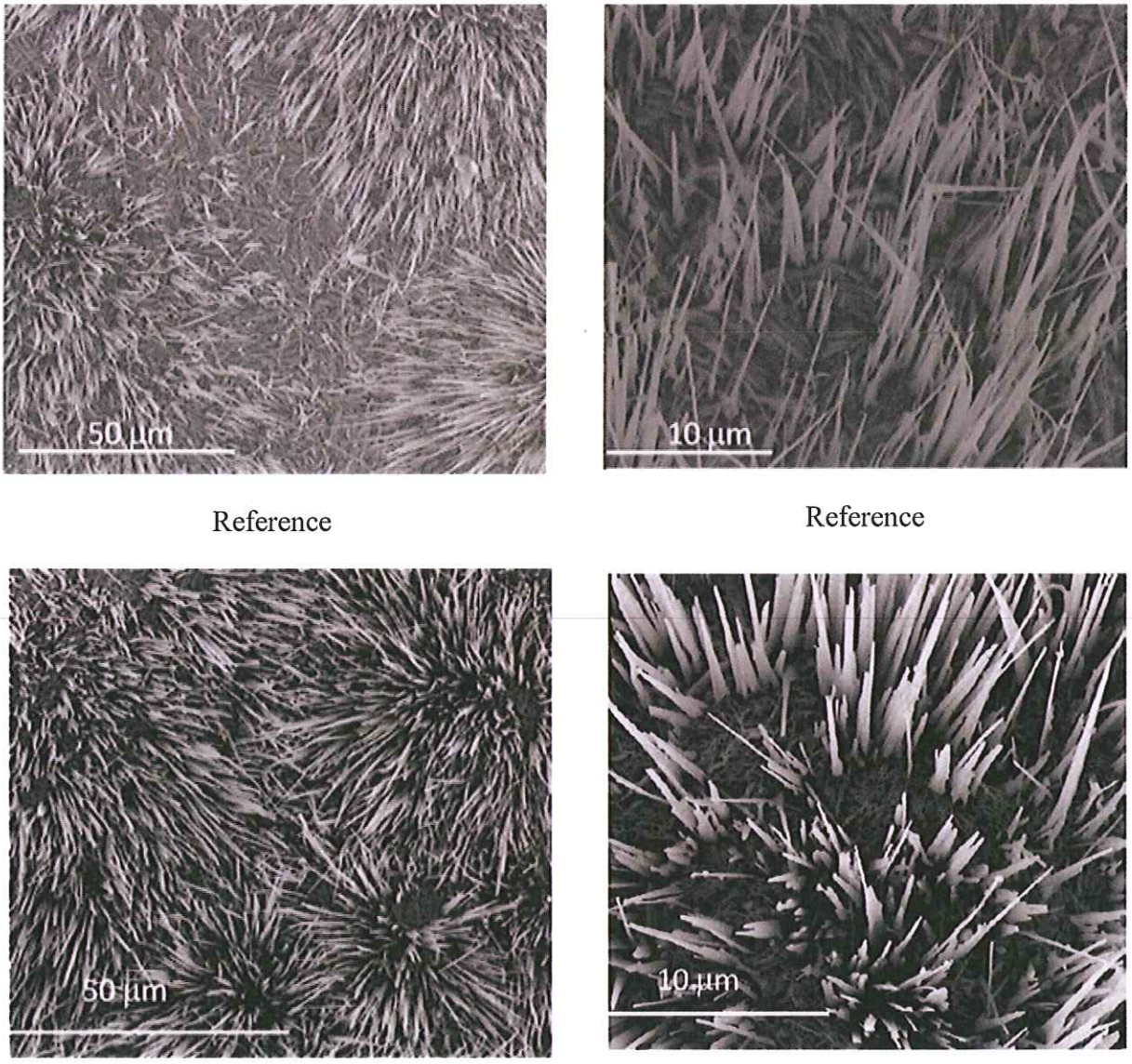

Figure V.16: SEM surface micrographs (top) Reference , (bottom) Fe9Cr (ref) after oxidation at 700°C for 100 h in air+12% vol. water vapour.

Not only displaying the same mass variation, the reference and Fe9Cr have also the similar oxide morphology. Indeed iron oxide needles or whiskers are seen on the surface of both steels samples after oxidation at 700°C for 100h in air +12% vol. water vapour (cf. Figure V.16). XRD surface analyses of those corroded samples allow identifying Fe_3O_4 (ICDD n°071-6336) and Fe_2O_3 (ICDD n°033-0664) as the main crystalline constituent, of the scale. Similar observation is found in the literature when low chromium steels are oxidized in water vapour containing environment [13-16]. The mechanism for whisker formation discussed by

Raynaud and Rapp [16] and first proposed by Tallman and Gulbransen [17] that is generally accepted involves surface diffusion inside a hollow structure that results from the presence of a dislocation in the oxide. The growth of the whiskers is more pronounced in water vapour containing atmospheres because of faster dissociation of water vapour compared with oxygen. Zeng and Young [15] suggest that an important aspect of whisker formation is that the tip of the whisker is catalytically active in promoting dissociation of the oxidant. It is evident that the growth of whiskers is controlled by a surface reaction and thus linear kinetics will be observed, but as the oxide thickens then the rate limiting process for scale growth is diffusion controlled.

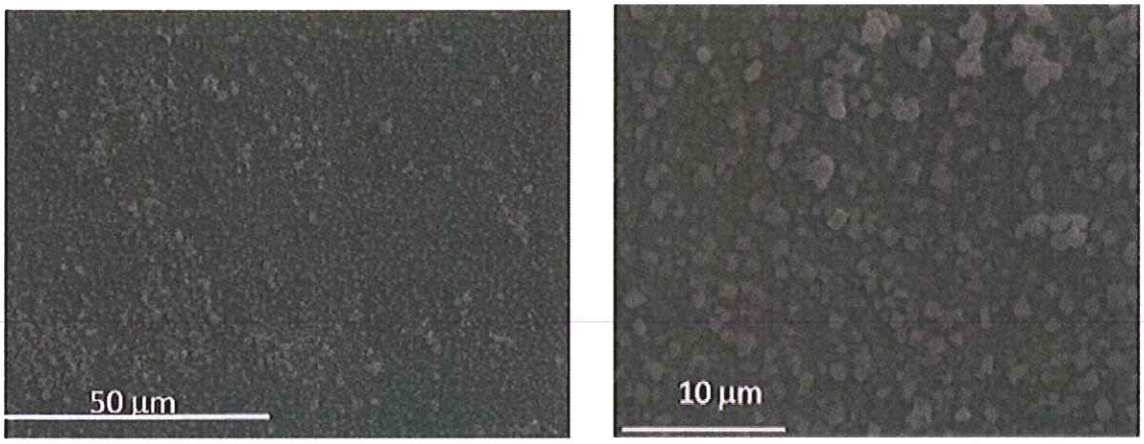

Figure V.17: SEM surface micrographs for Fe9Cr (0.5 wt %. Si) after oxidation at 700°C for 100 h in air+12% vol. water vapour.

Figure V.17 shows SEM surface micrographs corresponding to Fe9Cr (0.5 wt %. Si) after oxidation for 100h at 700°C in air enriched in water vapour. In opposition with what was observed previously in Figure V.16, no iron needles or whiskers were found. Small white submicronic crystallites are formed all over the surface of the samples. EDX analyses highlight the presence of iron, manganese and chromium in the oxide scale. EDX analysis was also performed on a spalled part of the sample. Silicon oxide was then identified in the inner part of the oxide scale. On the XRD pattern corresponding to the scale top surface show only peaks of mix oxide phase $(Cr,Fe)_2O_3$ (ICDD n°035-1112) were present.

Figure V.18 presents scale morphology of the Fe9Cr (1.5 wt % Si) sample. Platelets of oxide cover the sample surface. Their geometrical forms are typical of the spinel oxides. EDX analysis on this sample gives an idea of the composition of the oxide scale. Indeed, the platelets are mainly composed of chromium with enrichment in manganese and iron. Beneath the platelets the oxide is enriched in silicon and vanadium. Better behavior of Fe9Cr (1.5 wt %. Si) compared to Fe9Cr (0.5 wt % Si) in air enriched in water vapour could be due the

formation of these spinel like oxide enriched in chromium. The presence of such protective phase was confirmed by XRD pattern of the scale where $(Cr,Fe)_2O_3$ (ICDD n°035-1112) was detected.

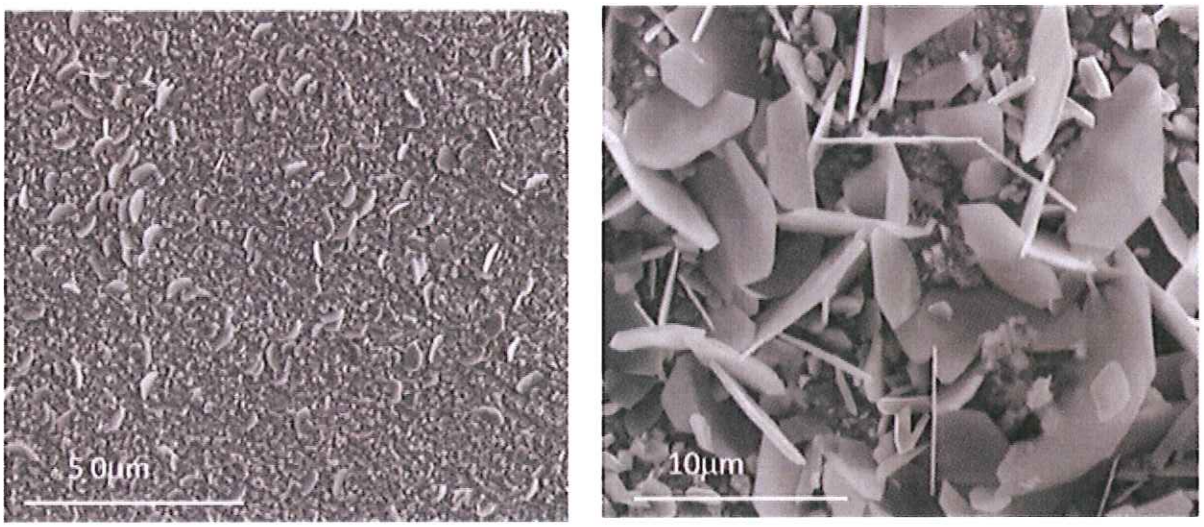

Figure V.18: SEM surface micrographs for Fe9Cr (1.5 wt % Si) after oxidation at 700°C for 100h in air+12% vol. water vapour.

In Figure V.19, a very thin oxide layer is observed. Scratches due to the polishing steps of the samples preparation are still visible. Oxide nodules have grown along those scratches. The low thickness of the oxide was expected according to the very low mass gain of Fe9Cr (0.01 wt % V) sample as seen on Figure V.15. EDX analysis shows that the oxide scale is composed of chromium manganese, iron and silicon oxides. This composition is not surprising; indeed due to the thin oxide layer we have information on the substrate composition. Nevertheless important efforts of comprehension of the vanadium effect on the oxide growth mechanism are still needed.

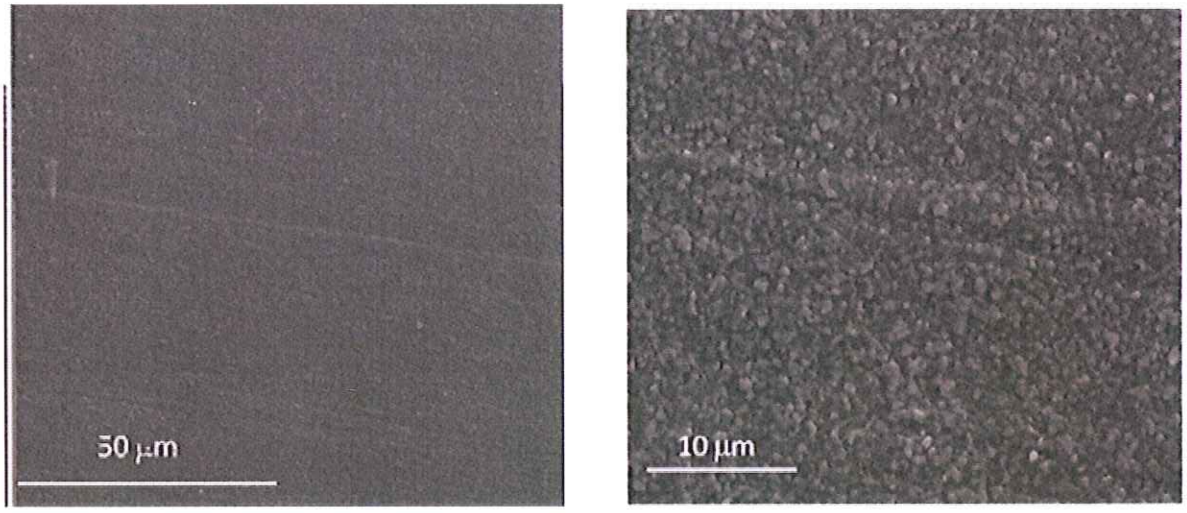

Figure V.19: SEM surface micrographs for Fe9Cr (0.01 wt %. V) after oxidation at 700°C for 100 h in air+12% vol. water vapour.

V.2.3 Steam effect on casting enriched in silicon, TEM results.

Oxidation experiment was performed on Fe9Cr (0.5 wt % Si) and Fe9Cr (1.5 wt % Si) steels at 650°C for 100h in steam with a pressure of 2.10^{-2} bar using the XPS oxidation chamber described previously. A thin film of a cross section of those corrosion products was prepared by FIB prior to observation in TEM. In steam, important oxidation rate was observed on Fe9Cr (0.5 wt % Si). The thickness of the formed oxide layer is significant; it was not possible to do a cross section by FIB on the entire scale.

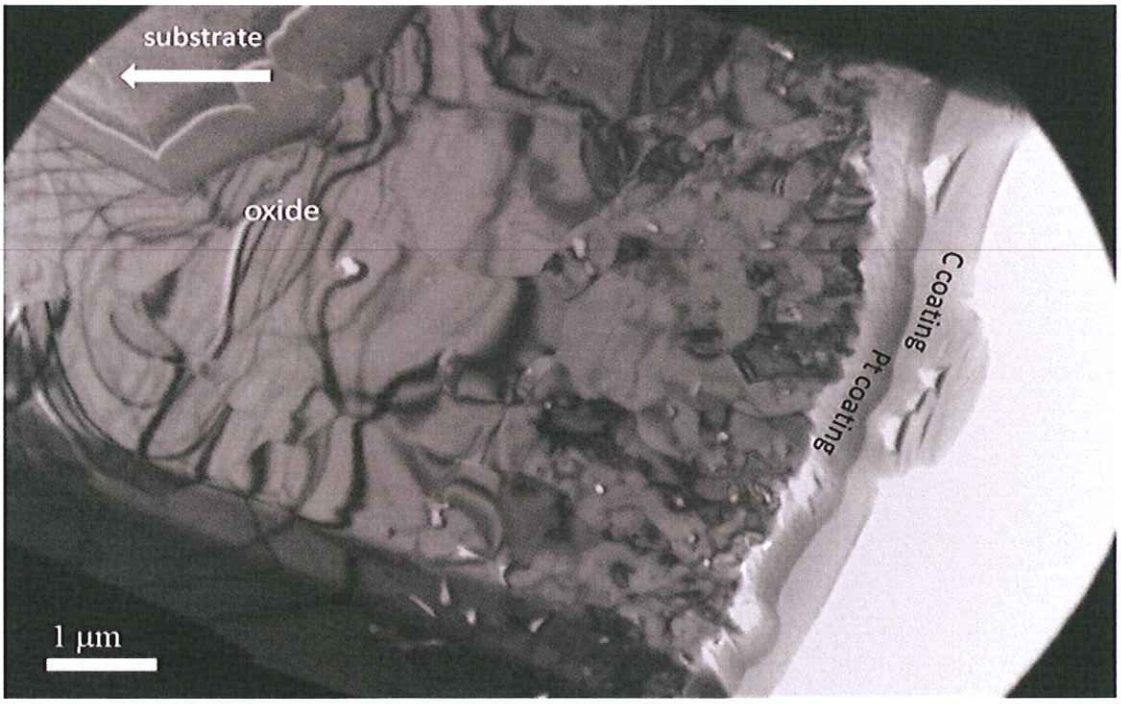

Figure V.20: FIB cross section of Fe9Cr (0.5wt %. Si) steel oxidized for 100 h in steam at 650°C.

Figure V.20 gives an idea of the oxide thickness, the several micrometers of oxide visible on the micrograph is far from being representative of the entire scale thickness. The scale is composed of big oxide grains in the inner part. Holes are present within the grains. The top part of the foil is composed of smaller oxide grains where it is also possible to distinguish some pores. The EDX semi quantitative analysis corresponding to the two parts of the scale previously described are similar. Table V.6 resumes the results obtained concerning iron, chromium and oxygen species. According to the EDX results, the Fe/O atomic ratio is close to the one corresponding to hematite.

Elements	% weight	% atomic
O	35.2	65.4
Fe	64	34.1
Cr	0.8	0.5

Table V.6 : EDX semi quantitative analysis on Fe9Cr (0.5wt %. Si) steel FIB cross section after oxidation for 100h at 650°C in steam.

In the case of Fe9Cr (1.5wt % Si) the oxide scale formed after oxidation in steam at 650°C is much thinner. Indeed, on Figure V.21, which is a FIB cross section of the corrosion products, the entire scale is visible and its thickness is around 150 nm.

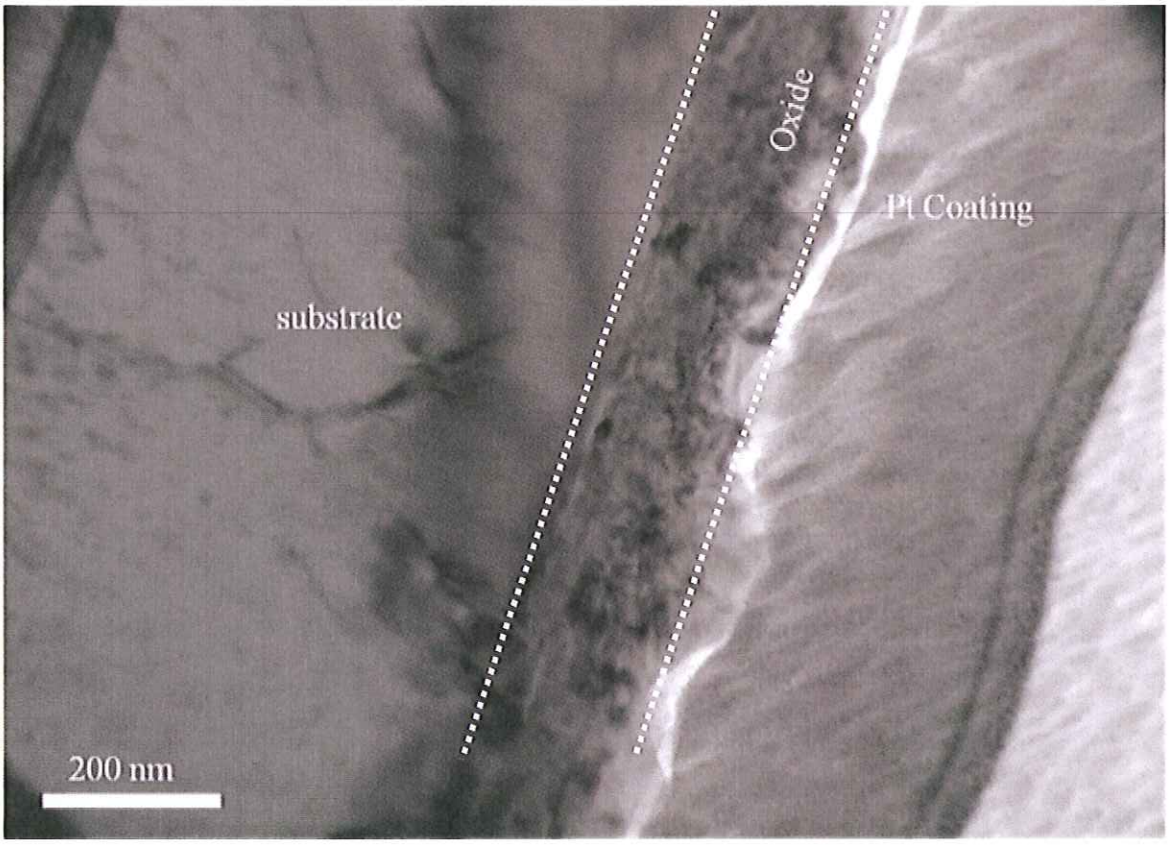

Figure V.21: FIB cross section of Fe9Cr (0.5wt %. Si) steel oxidized for 100 h in steam at 650°C.

Small grains form the thermally grown oxide layer. A complex scale composition is highlighted by EDX analysis. Indeed, iron oxide, vanadium oxide, silica, and manganese oxide are present in a layer mainly composed of chromium oxide. Table V.7 presents the semi quantitative analysis corresponding to oxide scale. Moreover high magnification TEM micrograph allows us to determine the presence of a thin (around 2 nm thick) continuous and amorphous silicon rich oxide at the interface metal/oxide (Cf. Figure V.22). The formation of

such an interface (white bubble) as mentioned previously could be responsible for the good results observed.

Elements	O	Fe	Cr	Si	V	Mn
% weight	29.2	17.1	42.2	0.6	0.4	10.5
% atomic	57.7	9.7	25.8	0.6	0.2	6

Table V.7: EDX semi quantitative analysis on Fe9Cr (1.5wt % Si) steel FIB cross section after oxidation for 100 h at 650°C in steam.

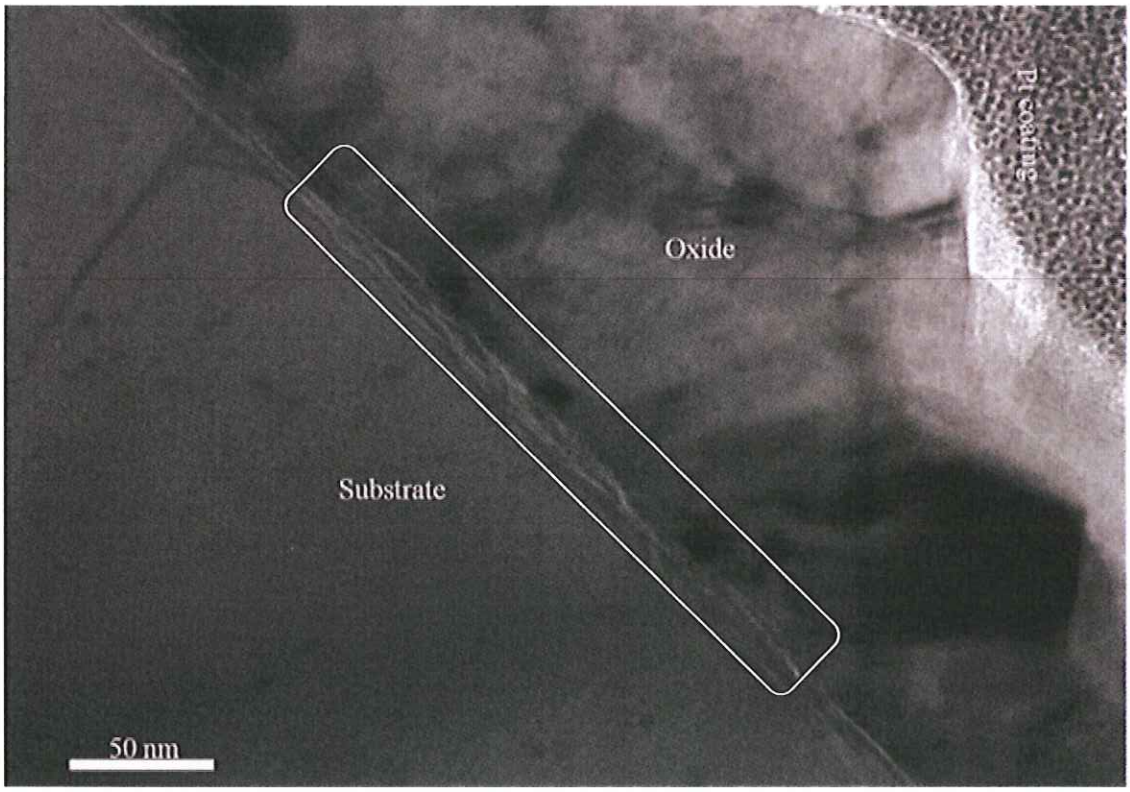

Figure V.22: High magnification TEM micrograph of Fe9Cr (0.5wt %. Si) steel oxidized for 100h in steam at 650°C. The red bubble underlines the metal/oxide interface.

V.3 General summary and discussion on ways to improve 9%Cr steel high temperature corrosion resistance.

9%Cr chromium steel is a grade intensively used for its mechanical properties and its low production cost. Nevertheless, it has shown its limits for application at 650°C in dry or wet environment due to catastrophic corrosion phenomena which can occur in those service conditions. In order to improve the high temperature corrosion resistance of this steel, several ways to increase its temperature performance were investigated.

Chemical vapour deposition processes, such as pack cementation coating and metal oxide chemical vapour deposition of reactive elements were studied. Improved behavior of 9%Cr steel grade was reported by Agüero et al. [1-3, 18] after coating with aluminide by slurry deposition. The intermetallic phase formed stable alumina phases which protect the substrate. In our case the deposition of aluminum was done by pack cementation according to the method developed by Houngninou et al. [7-8] but difficulties were faced to obtain homogeneous FeAl layer. Indeed, important coatings too rich in aluminum were formed or outside iron diffusion was also observed during the cementation. Those phenomena could definitely be detrimental to the substrate and the aluminum oxide integrity during long time exposure at high temperature. Therefore changes in the pack composition and dwelling temperature were realized. A decrease of the aluminum activity in the pack using a Cr15%Al metallic powder instead of pure aluminum gave satisfying results. Nevertheless this process should be optimized.

La_2O_3, Nd_2O_3, and Y_2O_3 coatings realized by MOCVD methods were investigated as a way to improve 9% Cr steel corrosion resistance in hot gases. Isothermal tests performed on La_2O_3 coated sample and Y_2O_3 coated were not really conclusive. As a fact, mass gains in both cases were higher than that measured with the same oxidizing condition for the uncoated steel used a reference and crack of the coating are even seen for investigation at 750°C. But, these conclusions should be analyzed cautiously. Chevalier et al [10-12] show that rare earth protective coatings effects are usually probed at higher temperatures than 700°C. Studies during cycling experiments at 700°C of those coatings and pack aluminide coated samples, give interesting outlooks about their utilization as a solution for the material. What is observed for the first 9 cycles where aluminide coated sample show higher mass gain than for uncoated sample, may be due to the density difference of the formed oxide in that particular

case, but after the 10th cycle it is clearly possible to state that those coatings have positive effect over 9%Cr steel resistance at high temperature corrosion in cyclic condition. Indeed, the uncoated material shows deterioration (cracks) after the 9th cycle, whereas the coated ones have still low mass evolution which could be considered as a better behavior in such drastic service conditions.

Nevertheless, the main obstacles to the development of such protection techniques for industrial steels are their costs and the difficulties to adapt them at important production scale.

Improving the behavior of low chromium containing steels by addition of alloying elements was also a solution investigated in this chapter. As a general trend, modification of the alloys composition shows good results in isothermal and cyclic condition in laboratory and in air enriched in water vapour.

The detrimental effect of vanadium in the corrosion behavior of the 9% Cr steel was also highlighted. Samples without vanadium display lower mass gain both during oxidation at 750°C in laboratory air and at 700°C in air enriched with water vapour. Thus if vanadium in the steel bulk is necessary for mechanical properties (strengthening by carbide formation), it definitely decreases its high temperature oxidation resistance.

The effect of Si content in the steel bulk is of the highest interest; because important decrease in the oxidation rates was observed when the silicon content of the material increased. Formation of a thin continuous and amorphous silica layer is supposed to be responsible for introducing change in Fe cations outward diffusion mechanisms, and thus is impeding the formation of porous iron oxide. Moreover beneficial effect on oxide scale adhesion is also supposed to be the corollary of silicon addition in the bulk material. But, in agreement with A.M. Huntz et al. [19], further investigation is necessary in order to determine the optimum quantity of this alloying element which should be added in the casting. Indeed, lower mass gain is observed in the case of 0.5wt %. Si content sample than in the case of 1.5wt % Si content sample after oxidation in laboratory air at 750°C for 100 hours; whereas in in air + 12% vol. water vapour at 700°C it is the opposite tendency.

REFERENCES

[1] A. Agüero, J. Garcia de Blas , R. Muelas, A. Sanchez, S. Tsipas, Materials Science Forum, 369 (2001) 939.
[2] A. Agüero, R. Muelas, B. Scarlin, Coatings for steam power plants under advanced conditions, Materials for Advanced Power Engineering edited by J. Lecomte-Beckers, M. Carton, F. Schubert, P.J. Ennis, Schriften des Forschungszentrum Jülich Reihe Energietechnik, 21 (2002) 1143.
[3] A. Agüero, R. Muelas , Materials Science Forum, 461 (2004) 957
[4] B.A Pint, Y.Zhang, P.F Tortorelli, J.A Haynes, I.G Wright, Materials at high temperatures 18 (2001) 185
[5] A.L Baldi, Modified diffusion coating of the interior of a steam boiler tube, US patent n° 4,208,453 (1980)
[6] C. Choux, Ph .D thesis, University of Bourgogne, Dijon, France (2008)
[7] C. Houngninou, Ph .D thesis, university of Bourgogne, Dijon , France (2004)
[8] C. Houngninou, S. Chevalier, J.P. Larpin, Applied Surface Science, 236 (2004) 256.
[9] Y. Q. Wang, Y. Zhang, and D. A. Wilson, Surface and Coating Technology, in press (2009).
[10] S. Chevalier, Ph .D thesis, University of Bourgogne, Dijon, France (1998).
[11] S. Chevalier, G. Bonnet, J. P. Larpin, Applied Surface Science, 167 (2000) 125.
[12] S. Chevalier, M. Kilo, G. Borchardt, J. P. Larpin, Applied Surface Science 205 (2003) 188
[13] B. Pieraggi, C. Rolland and P. Bruckel, Materials at High Temperatures, 22 (2005) 61
[14] Maurício de Jesus Monteiro, Stuart Saunders and Fernando Cosme Rizzo Assunção, "The Effect of Water Vapour on the High-Temperature Oxidation of a High Speed Steel", proc. ABM 2006, (2006) 128.
[15] X. G. Zeng and D. J. Young, Oxidation of Metals, 42 (1994) 163.
[16] G. M. Raynaud and R. A. Rapp, Oxidation of Metals, 21 (1984) 89.
[17] R. L. Tallman and E. A. Gulbransen, Journal of the Electrochemical Society, 114 (1967) 1227.
[18] A. Agüero, R. Muelas, M. Gutierrez, R. Van Vulpen, S. Osgerby, J.P. Banks, Surface and Coatings Technology, 201(2007) 6253.
[19] A. M. Huntz, V. Bague, G. Beauple, C. Haut, C. Severac, P. Lecour, X. Longaygue and F. Ropital, Applied Surface Science, 207 (2003) 255.

VI. Synthesis and outlooks

VI.1 Synthesis

Improving and finding solutions for our energy issues, to meet the ever increasing worldwide demand, is of utmost importance. [1-2]. Thermal power plants will therefore be used at higher temperature than nowadays. And their working conditions could be responsible for the degradation of engineering parts made of 9%Cr steel [3-6].

In this work, the behaviour at high temperatures ($T \geq 600°C°$) of a 9%Cr steel grade was studied in laboratory air under atmospheric pressure, but also in laboratory air enriched with 12% vol. of water vapour, and in pure steam (2.10^{-2} bar).

9%Cr chromium steel such T/P91 is not a chromia forming alloy, thus at 650°C or at higher temperature their utilization could be limited. In air under atmospheric pressure and at this temperature a temporary protective chromium iron oxide mixture is formed following a particular mechanism where both outward cations and inward anions diffusion are involved. During the first step of oxidation, the Cr supply is not sufficient and both in –situ high resolution diffraction using synchrotron facilities and in –situ XPS analysis underscored the fact that an iron chromium spinel with important Cr defects could be formed (Fe(II) Cr(IV))O_4. With time exposure and/or higher temperatures, a chromium iron oxide scale rich in chromium $(Cr,Fe)_2O_3$ grows on the steel and can decrease temporarily the oxidation rates. Nevertheless, the chromium quantity within the bulk being low, for long term exposure or for extremely high temperature ($T \geq 700°C$) porous iron oxide layers: Fe_3O_4, and Fe_2O_3 on top of it, are quickly formed corresponding to a critical oxidation states of the substrate. Indeed, in this case, thick oxide scale is formed which could spall leading to the destruction of the material [7-8]. Moreover, Vanadium used as a strengthening element in the steel composition could also be detrimental to its corrosion resistance properties at temperature higher than 650°C. This alloying element is well-known for forming a volatile oxide at this temperature which could be damageable to the integrity of the $(Cr,Fe)_2O_3$ layer .

Inward oxygen anions diffusion and outward metal cations diffusion have been underlined through isotopic labeling experiment. Reactions at both metal/oxide and oxide/gas interfaces should be considered during high temperature oxidation process in air for 9%Cr steel.

In humid atmosphere (steam or air enriched in water vapor) the kinetic of formation of iron oxide layers is increased and thicker oxide scales are formed in comparison to what observed in dry environment. Important pores were present within the oxide scale. The water decomposition at the surface of the samples and the diffusion of species such as OH^- within the scale instead of O^{2-} could be responsible for those phenomena. The presence of pores and gaps in the thermally grown layer can affect its mechanical integrity. Spallation can easily occur in this case and the life time of components used in such conditions can be severely diminished.

Thus, in both dry and humid atmospheres 9%Cr steels at 650°C have been proved improper for long time utilization as building material for technical and engineering parts.

Consequently, it is necessary to develop solutions for improving the high temperature oxidation resistance of low chromium steel grades. In this work several options were proposed, such a CVD coating methods (Pack cementation aluminide coating, metal organic chemical vapour deposition of reactive element oxide). The aims of those CVD techniques are to form protective scale which , by acting as a barrier, will slow down the inward and outward ion diffusion phenomena and although decrease oxidation rates of the 9% Cr steel substrates. However, these coating methods present a high cost and are difficult to transpose at an industrial scale. Furthermore, the tests for this work were carried out on plate , and the issues of the inner tube coating could also be discussed.

The effects of alloying elements addition on the high temperature resistance properties of the 9% Cr grade were also investigated. Particular attention was paid to the silicon content and its effects. The addition of silicon in the bulk of the low chromium containing steel seems to have beneficial effects on the oxidation rate in both dry and steam containing environments. The formation of a continuous and amorphous silica layer at the metal/oxide interface could explain the effect. Indeed, the obtained results show that the presence of iron in the oxide scale decreases when the amount of silicon in the bulk increases. Moreover the silicon oxide could help to enhance adhesion of the chromium rich oxide layer on the substrate.

This work has also highlighted the fact that the beneficial effect of silicon addition could be optimized for certain silicon contain and depends also of the atmosphere. When in dry environment 0.5 wt % Si in the bulk show good results, this amount is not enough to guarantee the utilization of the steel in steam at 650°C. For 1.5 wt % Si containing steel, better behaviour is observed in steam than for 0.5 wt % Si containing steel.

VI.2 Outlooks.

The 9% Cr steel has shown its limits of utilization at 650°C which is the new targeted service temperature for the thermal power plant. The addition of elements in the bulk was considered as a possible way to improve its resistance at high temperatures in dry and steam containing environments. Long term oxidation tests, should be nevertheless performed in order to confirm the better observed behaviour of the modified castings. Indeed data corresponding to long term oxidation should be obtained to simulate the behaviour for at least the life time of pipes made of 9% Cr steel. Moreover the grade is chosen for its mechanical properties, essentially its creep resistance and its thermal conductivity. It is necessary in order to validate one or the other solution to perform mechanical tests and to verify that neither the conductivity nor the creep strength is affected by the composition modification. As already mentioned, the geometry effect should be also considered and oxidation tests should also be done on pipe made of the modify steel.

As 650°C has been proved to be a temperature limit for the utilization of low chromium containing steel such as T/P91 in coal fire power plant, it is possible propose new fields of applications for this grade.

In the laboratory "Interdisciplaire Carnot de Bourgogne" important research on the development of metallic interconnectors for fuel cell is being done. It has been shown that T/P91 could be a good candidate for the new Solid Oxide Fuel Cells (SOFC) destined to work at 600°C. Within the IDEAL CELL European research project, several tests with T/P91 have already been performed and show promising results. This could be a way to ensure the utilization of 9%Cr steel in future power generating stations.

REFERENCES

1] http://www.iea.org
[2] J.D. Parker, Materials at high temperatures, 2 (2002) 47.
[3] Protocole de Kyoto à la convention-cadre des nations unies sur les changements climatiques, Nations Unies, 1998. FCCC/INFORMAL/83. GE.05-61647 *(F)* 070605 090605.
[4] http://en.wikipedia.org/wiki/File:PowerStation2.svg
[5] R. Viswanathan , W.T. Bakker, Proceedings of 2000 International Joint Power Generation Conference, Miami Beach, Florida, July 23-26 (2000).
[6] R. Viswanathan, Advanced Materials and Processes, August (2004) 73.
[7] R. Viswanathan, R. Purget, U. Rao, Proceedings of the 7th Liege Conference on Materials for Advanced Power Engineering, Energy Technology, 21, Part I-III (2002) 1109.
[8] A. Agüero, Garcia de Blas, R. Muelas, A.Sanchez, S. Tsipas, Materials Science Forum, 369 (2001) 939
[9] A. M. Huntz, V. Bague, G. Beauple, C. Haut, C. Severac, P. Lecour, X. Longaygue and F. Ropital, Applied Surface Science, 207 (2003) 255.

Résumé :

Les aciers ferritiques à faible teneur en chrome tel que le T/P91 sont largement utilisés dans les centrales de productions d'électricité pour leurs bonnes propriétés mécaniques et leur faible coefficient d'expansion thermique. Cependant, la demande croissante en énergie alliée à la nécessité de réduire les émissions de gaz à effet de serre, conduisent à envisager l'augmentation des conditions d'utilisation (température et pression) de ces matériaux. Des études ont montré qu'en modifiant la température de fonctionnement et la pression de vapeur d'eau de 538°C/18.5 MPa à 650°C/30 MPa, le rendement des centrales thermiques progressait d'environ 8%. Se pose alors la question de la tenue à la corrosion à haute température des aciers à 9% de chrome.
Au cours de ces travaux, le comportement d'un acier ferritique/ martensitique à 9% de chrome a été étudié à 650°C sous air sec et sous vapeur d'eau de matière isotherme et en conditions de cyclage thermique. La prise de masse des échantillons renseigne sur la cinétique de la réaction d'oxydation et l'adhérence des couches d'oxydes formées. Les produits de corrosion ont été caractérisés par plusieurs techniques d'analyses dans l'optique de clairement identifiés les oxydes en présences et leurs mécanismes de formation. Des oxydes mixtes de fer et de chrome $(Cr,Fe)_2O_3$ sont dans un premier temps formés et assurent s'avèrent être temporairement protecteur. Pour des longs temps d'oxydation ou des températures supérieures à 650°C, la magnétite Fe_3O_4 et l'hématite Fe_2O_3 sont les principaux oxydes formés, montrant ainsi l'inadéquation des nuances à faible teneur en chrome pour une utilisation dans des conditions aussi drastiques. Dans l'optique d'augmenter la résistance à la corrosion à haute température de cet alliage, diverses solutions ont été envisagées tel que l'aluminisation par cémentation en caisse, les revêtements d'oxydes de terre rare par MOCVD, ou encore l'ajout d'éléments d'addition. Ces solutions ont été également testées à 650°C sous air sec et sous vapeur d'eau.

Abstract:

The improvement of high temperature oxidation resistance of low chromium content steels, such as T/P91, is of great interest in regards with their application in thermal power generating plants. Indeed, they possess good creep properties, and low thermal expansion coefficient. Important needs in energy together with environmental issues place power generation plants under constraints which lead to develop high efficiency systems. A usual way to increase the efficiency consists in increasing temperature and pressure parameters of the power generating plant. Studies has shown that the total efficiency of a plant increases by nearly 8 % when changing the steam parameters from 538°C/18.5 MPa to 650°C/30 MPa. Then, the problem of corrosion resistance of 9% chromium steel in those conditions is asked.
In this work, the behavior of a ferritic / martensitic 9% chromium steel has been studied at 650°C in dry air and in water vapor containing environment in both isothermal and thermal cyclic conditions. The weight gain of samples provides information on the kinetics of the oxidation reaction and the adhesion of formed oxide scale. Corrosion products were characterized by several analytical techniques in order to identify oxides with accuracy and to understand their formation mechanisms. Mixed iron and chromium oxides $(Cr, Fe)_2O_3$ are initially formed and provide temporary protection to the substrate. For long time exposure or temperatures above 650°C, magnetite, Fe_3O_4 and hematite Fe_2O_3 are the main oxides formed, highlighting the fact that low chromium steel are inappropriate for applications in such drastic conditions. In order to increase the high temperature corrosion resistance of this alloy, various solutions have been proposed as aluminizing by pack cementation, reactive element oxides coatings of by MOCVD, or addition of alloying elements in the steel composition. These solutions were then tested at 650 ° C in dry air and in water vapor environments.

Key words : T/P91, low chromium steel, high temperature oxidation, cyclic oxidation tests, water vapour, MOCVD coatings, alloying elements, silicon, XPS in-situ analyses, ESRF Synchrotron and high resolution XRD.